Czech Technical University in Prague
Faculty of Nuclear Sciences
and Physical Engineering

DOCTORAL THESIS

A study of the $b\bar{b}$ production mechanisms with the ATLAS experiment

Prague 2016

Ing. Michal Marcisovsky

Bibliographic entry

Author:	Ing. Michal Marcisovsky, Czech Technical University in Prague, Faculty of Nuclear Sciences and Physical Engineering, Department of Physics
Title of Dissertation:	A study of the $b\bar{b}$ production mechanisms with the ATLAS experiment
Degree Programme:	Nuclear Engineering
Field of Study:	Experimental Nuclear Physics
Supervisor:	prom. fyz. Vaclav Vrba CSc., Institute of Physics of the Czech Academy of Sciences, Prague
Academic year:	2016
Number of Pages:	186
Keywords:	ATLAS, B-physics, QCD, azimuthal correlations

Bibliografický záznam

Autor:	Ing. Michal Marčišovský, České vysoké učení technické v Praze, Fakulta jaderná a fyzikálně inženýrská, Katedra fyziky
Název práce:	Studium produkčních mechanismů $b\bar{b}$ kvarků na experimentu ATLAS
Studijní program:	Jaderné inženýrství
Studijní obor:	Experimentální jaderná fyzika
Školitel:	prom. fyz. Vaclav Vrba CSc., Fyzikální ústav AVČR, v.v.i.
Akademický rok:	2016
Počet stran:	186
Klíčová slova:	ATLAS, B-fyzika, QCD, azimutální korelace

Abstract

The study of the production of $b\bar{b}$ quark pairs via measurement of the azimuthal angle correlations between them serves as an excellent tool for probing of QCD, particularly with consideration of contributions from higher order matrix elements. Measurement of $b\bar{b}$ pair azimuthal angle correlations at $\sqrt{s} = 8$ TeV using data recorded by the ATLAS detector in 2012 is presented in this thesis. The correlations were studied using J/ψ and μ proxies of the $B\bar{B}$ system. An increase of event yields at low $\Delta\phi$ was observed, which demonstrates important contributions from next-to-leading order processes to the $\Delta\phi$ distribution.

Abstrakt

Studium produkčních mechanismů párů $b\bar{b}$ kvarků prostřednictvím jejich úhlových korelací je účinný nástroj na testování QCD, hlavně příspěvků maticových elementů vyšších řádů. V této práci je prezentováno měření korelací azimutálního úhlu mezi $b\bar{b}$ páry při energii $\sqrt{s}$ =8 TeV za použití dat získaných experimentem ATLAS v roce 2012. Korelace byly studovány prostřednictvím rozpadového kanálu J/ψ a μ systému $B\bar{B}$. Byl pozorován nárůst v distribuci událostí v oblasti malých úhlů $\Delta\phi$, což demonstruje výrazný příspěvek procesů vyšších řádů.

Preface

The bottom quarks produced in high energy hadron collisions provide an essential test bench for the QCD. The b-quark is heavy enough ($m_b \gg \Lambda_{QCD}$) to justify the perturbative treatment. In the next-to-leading order (NLO) perturbative QCD, the bottom-antibottom ($b\bar{b}$) quark pair production is modeled by three distinct production mechanisms: flavor creation, flavor excitation and gluon splitting. The $b\bar{b}$ correlations are sensitive to the (N)NLO QCD processes.The fraction, in which each mechanism occurs is reflected in the production cross section, which can be estimated experimentally by measuring the correlations between the final states of particles arising from b and anti-b quarks. The topology of the produced $b\bar{b}$ allows discrimination between different QCD production mechanisms, and therefore predicted cross sections can be tested. One such variable viable for study of production mechanisms is the difference between azimuthal angles ($\Delta\phi$) between the final states. At the LHC nominal energy, most of the $b\bar{b}$ pairs are expected to be produced by the gluon splitting process, Born term (back-to-back $b\bar{b}$) contribution is expected to be smaller than at the Tevatron energy. The high rates of b production that are achieved at the LHC enable ATLAS to collect high statistics of B hadron decays, which allow measurements of $b\bar{b}$ correlations.

The thesis consists of eight chapters. The first chapter is devoted to the introduction to B-physics at ATLAS and production mechanisms of b quarks. The second chapter discusses the Pythia event generator and its emulation of higher-order QCD by parton showers. The third chapter is dedicated to ATLAS experiment, its subdetectors with emphasis given to the muon triggering and reconstruction. The fourth chapter gives an overview of the performed $b\bar{b}$ analysis, while the fifth chapter discusses dataset event selection. The sixth chapter discusses event modelling and unfolding of the detector effects, in the chapter number seven fit results are shown. The eighth chapter concludes the thesis.

Contents

“*He who makes a beast of himself gets rid of the pain of being a man.* ”

— Samuel Johnson

Chapter 1.

Introduction

In recent years, a significant progress has been made in understanding of bottom and charm quark production in both experimental and theoretical aspects. Traditionally, $b\bar{b}$ production has been studied using correlations of the azimuthal angle $\Delta\phi$ in di-muon events, where both muons are produced in semileptonic B hadron decays. The high luminosity and $\sqrt{s}$ of the Large Hadron Collider (LHC) allow studies in channels less burdened by backgrounds, such as $J/\psi + \mu$ or $J/\psi + J/\psi$. While many properties of the $b\bar{b}$ production are well described by the perturbative quantum chromodynamics (QCD), success in testing predictions by measurement is still limited.

1.1. Strong interaction

The Standard Model of elementary particles and interactions is an extremely successful quantum field theory describing behavior of elementary particles. Almost all experimental measurements are consistent with the model within measurement uncertainties, see figure 1.1. Within the Standard Model, matter consists of fermions with spin 1/2 and the strong, weak and electro-magnetic forces are mediated by spin-1 gauge bosons.

The QCD is believed to be a theory of strong interaction, and it is a part of the Standard Model (SM). It is constructed as a non-Abelian SU(3) gauge theory [2], following the path of quantum electrodynamics (QED) and Yang-Mills [3] theories. In QCD, each quark carries a quantum number called color, which is a conserved quantity. There are three colors $N_c = 3$, and therefore $(N_c)^2 - 1 = 8$ massless spin-1 gluons, which are gauge bosons of the theory. QCD does not distinguish between quark flavors, only the color charge of quarks matters. Since gluons carry color charge, they can couple to other

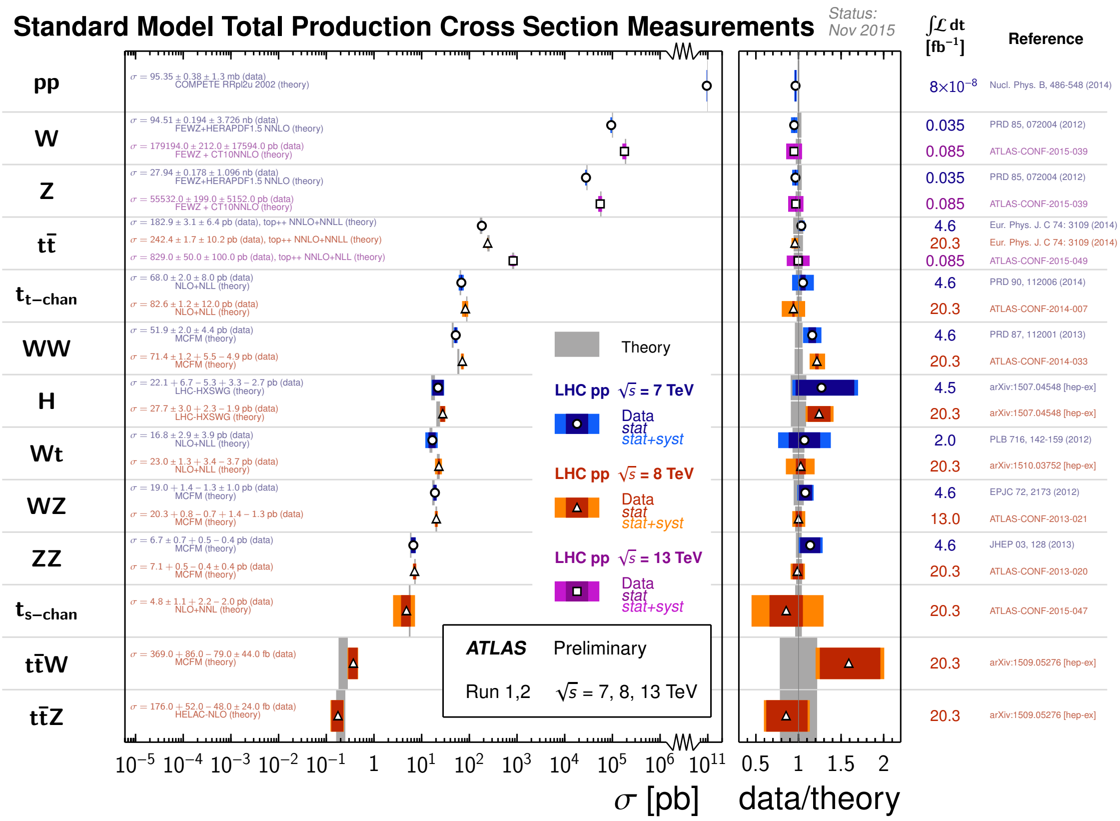

Figure 1.1.: Summary of several SM production cross section measurements, corrected for leptonic branching fractions, compared to the corresponding theoretical expectations. All theoretical expectations were calculated at next-to-leading order or higher. The W and Z vector-boson inclusive cross sections were measured with 35 pb^{-1} of integrated luminosity from the 2010 dataset. All other measurements were performed using the 2011 dataset, the 2012 dataset, or the 2015 dataset. The dark-color error bar represents the statistical uncertainly. The lighter-color error bar represents the full uncertainty, including systematic and luminosity uncertainties. The data/theory ratio, luminosity used and reference for each measurement are also shown. Image taken from [1].

gluons or even themselves, which is in strong contrast to gauge bosons of QED. The self-coupling of gluons causes several interesting properties of this theory, such as color confinement inside of hadrons with zero net outside color charge (color singlet state) and color antiscreening which leads to the asymptotic freedom of quarks within hadron [4] [5]. The result is running of the coupling constant of strong interaction, α_s, which is necessary in order to absorb infinities in the theory. At low energies (or corresponding large parton distances), the coupling constant becomes large and it is impossible to use standard QFT tools due to slow convergence or non-convergence of perturbation series. The coupling of the strong force becomes large at a scale $\Lambda_{QCD} \approx 250$ MeV [6]. It is approximately the scale where QCD becomes non-perturbative, because the strong coupling constant α_s approaches 1.

In QCD, quarks transform in a triplet transformation of color under the SU(3).

$$\psi = \begin{pmatrix} \psi_1 \\ \psi_2 \\ \psi_3 \end{pmatrix}$$

The quarks are transformed by eight unitary 3×3 matrices, eight generators, which are derived from the Gell-Mann matrices.

The Lagrangian can be written as:

$$\mathscr{L}_{QCD} = \sum_q \bar{\psi}_{q,a}(i\gamma^\mu \partial_\mu \delta_{ab} - g_s \gamma^\mu t^C_{ab} A^C_\mu - m_q \delta_{ab})\psi_{q,b} - \frac{1}{4} G^A_{\mu\nu} G^{\mu\nu}_A,$$

where γ^μ are the Dirac γ-matrices. The $\psi_{q,b}$ are quark-field spinors for a quark of flavor q with mass m_q and color index b which runs from $b = 1$ to $b = N_c = 3$. The A^C_μ represents the gluon field with C running from 1 to $(N_c)^2 - 1 = 8$. The t^C_{ab} corresponds to the eight matrices with dimensions 3×3, which are the generators of the SU(3) group. The α_s is connected to g_s via the relation $\alpha_s = \frac{g_s^2}{4\pi}$.

The field-strength tensor derived from A^C_μ has one crucial difference with respect to QED, that is the self-interaction of gluons:

$$G^a_{\mu\nu} = \partial_\mu A^a_\nu(x) - \partial_\nu A^a_\mu(x) + g f_{abc} A^b_\mu(x) A^c_\nu(x),$$

where f_{abc} are the structure constants of the SU(3) group. Alongside the masses of quarks, the strong coupling constant α_s is also a parameter of the QCD theory.

1.2. Beauty physics

The quarks come in three groups which are referred to as generations, there are also three corresponding generations of leptons. Each successive generation is heavier than the previous. Their properties are listed in table 1.1. Neither quarks nor gluons have ever been observed as free particles due to the QCD asymptotic freedom, with a notable exception of a top quark, which decays before it hadronizes.

Quark	Electric charge	Invariant mass
u	2/3	$2.3\ ^{+0.7}_{-0.5}$ MeV
d	-1/3	$4.8\ ^{+0.5}_{-0.3}$ MeV
c	2/3	1.275 ± 0.025 GeV
s	-1/3	95 ± 5 MeV
t	2/3	$173.21 \pm 0.51 \pm 0.71$ GeV
b	-1/3	4.66 ± 0.03 GeV

Table 1.1.: Invariant mass and electric charge of the Standard Model quarks [6].

The bottom (also called beauty) quark was discovered in E288 fixed-target experiment in Fermilab in the $p + Be \rightarrow \mu^+\mu^- + X$ [7] process. An excess of events was observed around invariant mass of 10 GeV as a series of resonances known as $\Upsilon(1\mathrm{S}, 2\mathrm{S}, 3\mathrm{S})$. These resonances are bound states of bottomonium, a meson consisting of a bottom and an anti-bottom quark. The bottomonia are also referred to as hidden beauty or covered bottom.

The bottom is the second heaviest quark in the SM. Due to its large mass, its coupling can be large to an assortment of new particles predicted by the beyond Standard Model (BSM) models. Due to its large mass and relatively long lifetime of B mesons, it is a useful tool in testing SM predictions at the LHC. In general, there are two strategies how to explore the TeV scale physics: direct production of new particles in hadron collisions and indirect through quantum interference effects from new particles in loop diagrams. Detailed studies of flavor physics, such as bottom physics, allow to study SM and potential BSM processes at energies beyond the direct production center-of-mass energy reach of the LHC. The precision flavor physics has tremendous potential to observe new physics phenomena which may shed light onto open questions in high energy physics and cosmology. The physics potential of B decays is discussed in [8] and [9].

Coincidentally, the bottom quark production in high energy collision allow a unique insight into the inner workings of the QCD. While the study of $b\bar{b}$ production mechanisms allows exploration of QCD properties at high energies, the study of bound states, open or closed beauty, lies at the edge of the QCD perturbativity. This dissertation thesis presents a measurement of $B\bar{B}$ correlations through $J/\psi + \mu$ proxies, where one B hadron decays into $J/\psi\ +\ X$ with subsequent J/ψ decay into a di-muon pair, while the other

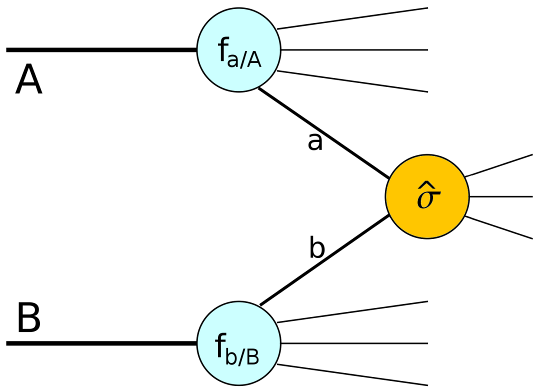

Figure 1.2.: The principle of computation of a generic hard process in a hadron collision.

B hadron decays semileptonically into $\mu + Y$ either directly or via an intermediate D meson.

1.3. *b* quark production mechanisms at the LHC

Bottom quark pair hadroproduction occurs primarily through the strong interaction at proton colliders. Within the QCD theory framework, the proton is understood a multi-body object with complex inner interactions. It consists of three valence quarks and a sea of virtual gluons and $q\bar{q}$ pairs. Thanks to the fact that the b quark is heavy, the cross section for the production of $b\bar{b}$ pairs from the proton-proton collision can be cast with the help of the factorization theorem [10]:

$$\sigma_{b\bar{b}} = \sum \int dx_a dx_b f_a^A(x_a, \mu_F^2) f_b^B(x_b, \mu_F^2) \hat{\sigma}_{ab}^{b\bar{b}}(p_a, p_b, \mu_F^2, \mu_R^2)$$

where $\hat{\sigma}_{ab}$ is perturbatively-calculated cross section for the interaction of two partons (a, b) resulting in the production of a $b\bar{b}$ pair. The μ_F and μ_R are the factorization and renormalization scales, respectively, and $f_i^X(x_i, \mu_F^2)$ are the parton distribution functions.

The graphical visualization of the factorization theorem is displayed in figure 1.2. Additionally, color confinement requires the produced bottom quarks be hadronized.

Parton distribution functions

The overview of the QCD physics at the LHC can be found in [11]. The properties of the naive static image of the proton are determined by its valence quarks, two u quarks and one d quark. The dynamic picture of the same proton is complex. The valence quarks interact between themselves via exchange of gluons, which can split into a virtual $q\bar{q}$ pairs which can in turn emit more gluons. Due to the exchange of soft gluons within the proton, a first principles calculation of the internal structure of the proton using tools of perturbative QCD is a desperate task. The partons involved in the hard process (high momentum exchange) are not well defined in pQCD. The statistical descriptions of parton momenta within proton were first attempted by the parton distribution functions (PDF). The PDF were introduced into the quark model by Feynman [12] to explain Bjorken scaling behavior in deep inelastic scattering experiments. From the collinear factorization point of view, their interpretation is probabilistic, i.e. finding a particle in a proton with a certain longitudinal momentum fraction x at a momentum transfer scale Q^2 is defined as $f_i(x, Q^2)$. Then, at the leading order, they can be interpreted as the probability to find a parton of type i inside the proton with a longitudinal momentum fraction in the interval from x to $x + \mathrm{d}x$ being $f_i(x, Q^2)\mathrm{d}x$. At higher order this interpretation breaks, because in some cases the next-to-leading order (NLO) PDFs can have negative value. In a proton collision, momenta of colliding partons are sampled from the proton PDFs at the energy scale of subprocess of interest. Usually, the PDFs are measured at lower momentum scales in an ep colliding experiments such as ZEUS or H1 at the late HERA collider, and are scaled up to the energy scale of interest by means of QCD evolution equations for parton densities. As the LHC is essentially a gluon-gluon collider and many hadron collider signatures of physics both within and beyond the SM involve gluons in the initial state, it is important to understand the gluon distribution.

The LO and NLO processes

Due to the behavior of the α_s at high energies, it is possible to apply perturbative approach in computation of observables. The cross section can be expressed as a series expanded in α_s. This approach is referred to as perturbative QCD (pQCD).

The cross section $\hat{\sigma}_{ij}^{b\bar{b}}$ can be written as a sum of processes of increasing order in α_s:

$$\hat{\sigma}_{ij}^{b\bar{b}} = \alpha_s^2(\mu_R^2)\hat{\sigma}_0(p_i, p_j, \mu_F^2, \mu_R^2) + \alpha_s^3(\mu_R^2)\hat{\sigma}_1(p_i, p_j, \mu_F^2, \mu_R^2) + ...$$

The leading-order (LO), or the first order results are given at $\mathcal{O}(\alpha_s^2)$. The second order, or NLO results are defined by the $\mathcal{O}(\alpha_s^3)$ term. Even higher orders, such as next-to NLO (NNLO) with $\mathcal{O}(\alpha_s^4)$, are following the same convention.

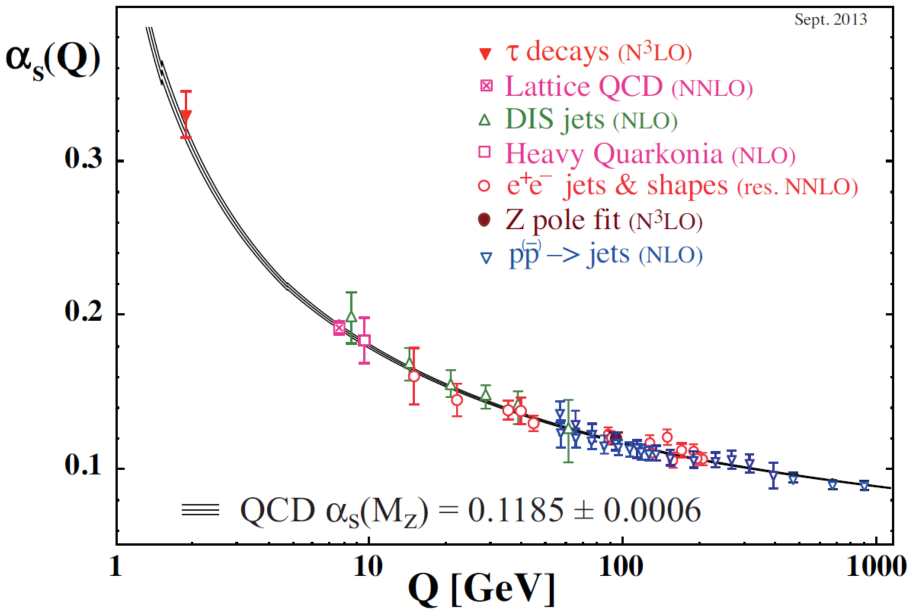

Figure 1.3.: The running coupling as a function of energy scale Q. [6]

In QCD, it may come as a surprise that the higher level terms in power series of α_s do not give progressively smaller corrections to the LO term. In fact, the NLO term is numerically comparable to the LO term, especially at high $\sqrt{s}$. This can be understood from the fact that the cross section for the LO process $gg \to gg$ is approximately 100 times larger than for the $gg \to b\bar{b}$ process. Any of the final-state gluons in the $gg \to gg$ scattering can split into a $b\bar{b}$ pair, giving a higher order $b\bar{b}$ pair production process which has a significant cross section. The suppression of this splitting by scattering kinematics and the additional factor α_s compensate the cross section enhancement of the NLO contribution to the level of the LO. Some of the Feynman diagrams contributing to the $b\bar{b}$ production are shown in figures 1.4 and 1.5.

The running coupling α_s as a function of energy scale is shown in figure 1.3. At the mass scale of a Z boson, $\alpha_s(M_Z^2) = 0.1185 \pm 0.0006$.

In LO $2 \to 2$ QCD processes, only $gg \to b\bar{b}$ and $q\bar{q} \to b\bar{b}$ processes are included in the computation of the $b\bar{b}$ cross section. Moreover, the bottom quarks are always produced back-to-back in the azimuthal angle $\Delta\phi(b, \bar{b}) \approx \pi$. Feynman diagrams contributing to the $b\bar{b}$ production at LO are shown in figure 1.4.

In the NLO process framework, the $b\bar{b}$ production processes have historically grouped into three categories:

- **Flavor creation** (FC) refers to the leading-order process which includes $2 \rightarrow 2$ processes of gluon fusion or $q\bar{q}$ annihilation diagrams plus higher order corrections to these processes. Because both b quarks emerge in the hard interaction, the states have $\Delta\phi \sim \pi$ and are balanced in transverse momentum (p_T).

- **Flavor excitation** (FEX) - Scattering of a b quark out of the initial state into the final state by a gluon or by light quark. One of the produced b quarks interacts and gets kicked away at significant angle. Because of this, b quarks tend to have asymmetric p_T.

- **Gluon splitting** (GS) is also referred to as parton showering, $b\bar{b}$ pair created within a parton shower process $g \rightarrow b\bar{b}$ in the initial or final state. Neither b nor $\bar{b}$ participate in the hard interaction, and therefore peak at small $\Delta\phi$.

At NLO, flavor creation consists of the $2 \rightarrow 2$ processes, in addition to diagrams where gluon initial-state radiation (ISR) or final-state radiation (FSR) is added to the $2 \rightarrow 2$ terms. Flavor excitation contains diagrams in which an initial state gluon splits into a $b\bar{b}$ pair before interaction with a parton coming from the other hadron, which effectively puts the b quarks on-shell. In gluon splitting diagrams, a gluon splits into a $b\bar{b}$ pair after interacting with the parton from the other hadron. Due to the additional parton in final states in NLO calculations, the resulting $\Delta\phi(b, \bar{b})$ distribution is non-zero over the whole range. The distribution still peaks in back-to-back region, but due to the GS component, it peaks also in the collinear regions of low $\Delta\phi$. Some of the Feynman diagrams contributing to the $b\bar{b}$ production at NLO are shown in figure 1.5.

The azimuthal angle refers to the $\Delta\phi = |\phi_Q - \phi_{\bar{Q}}|$, $\Delta\phi$ from the viewpoint of the above-mentioned processes is dependent on p_T and weakly on rapidity. Theoretical predictions and phenomenological discussions can be found in [13], [14] and [15]. The physics analysis and results presented in this thesis constitute the continuation of effort within the ATLAS collaboration to address the issues surrounding the measurement of $b\bar{b}$ angular correlations. Very early ATLAS predictions are shown in figure 1.6.

The produced $b\bar{b}$ pairs have distinct shapes in distributions of certain variables, the most notable are the azimuthal angle between them (angle in the plane perpendicular to the beam) and the polar angle. To visualize the azimuthal angle distributions for various processes, Pythia8 generator with PythiaB filter was used. The sample angular distributions as well as asymmetry parameter A are shown on the level of B hadrons in figure 1.7.

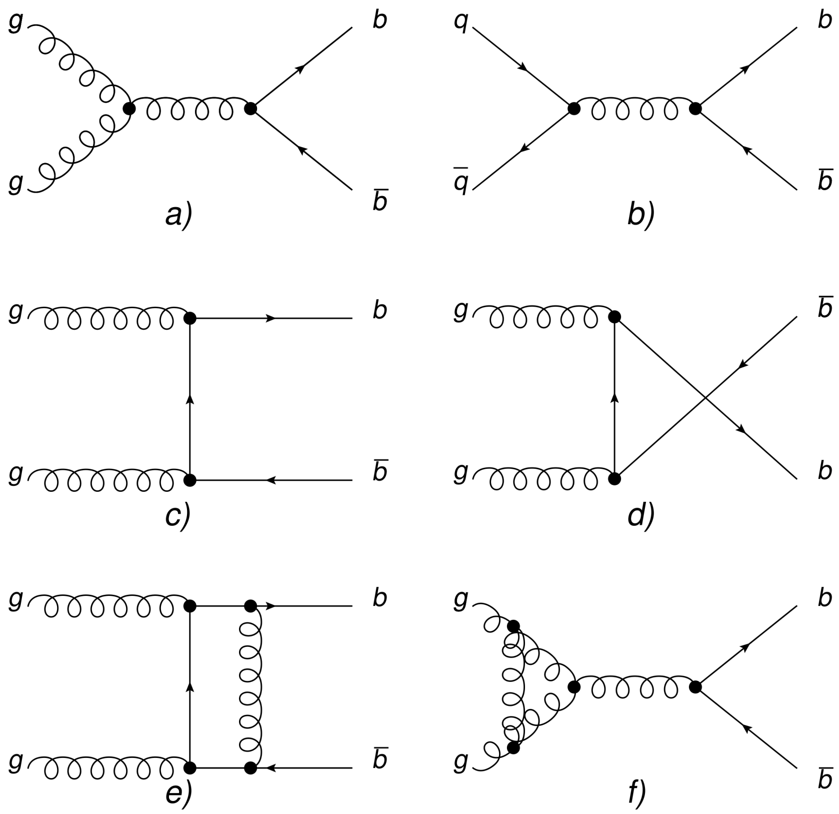

Figure 1.4.: The lowest order $2 \to 2$ Feynman diagrams that contribute to the bottom production. Figures (a) to (d) show the flavor creation diagrams, which have mostly two-body $b\bar{b}$ final states, usually produce back-to-back $b\bar{b}$ pairs balanced in transverse momentum. Taxonomy of $b\bar{b}$ diagrams in this fashion may become ambiguous at higher orders in perturbation theory. Two higher-order corrections with internal loop are shown in (e) and (f).

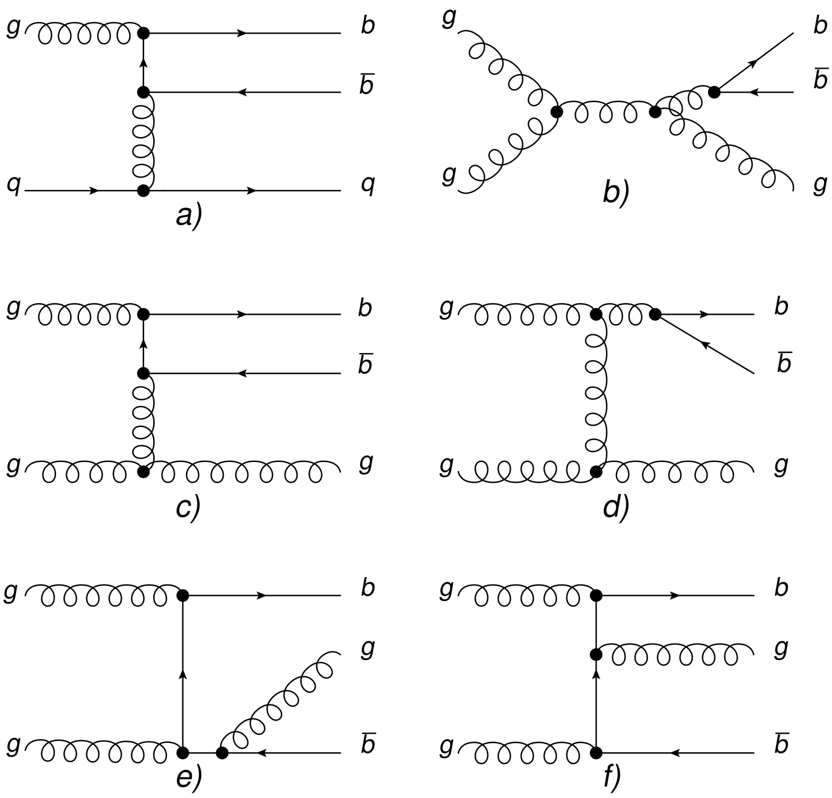

Figure 1.5.: The Born contribution NLO Feynman diagrams that contribute to the bottom production are shown for the flavor excitation class of processes in (a) and (c), while two examples of the gluon splitting are shown in (b) and (d). The two diagrams for the NLO corrections to the flavor creation are shown in (e) and (f), which interfere with GS and some FEX diagrams.

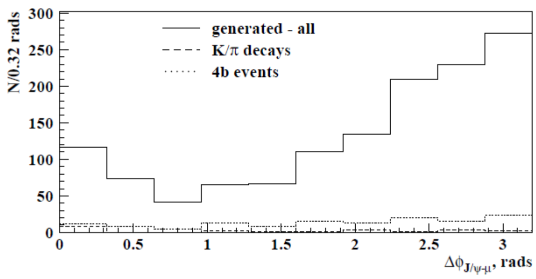

(a) The generator level distribution

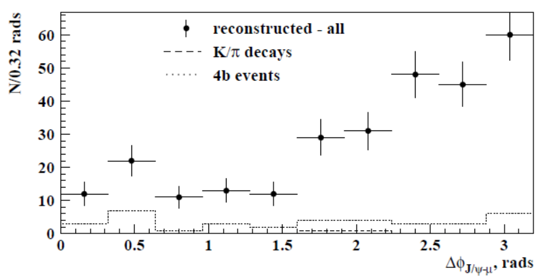

(b) Distribution after reconstruction

Figure 1.6.: The proxy $\Delta\phi(J/\psi, \mu)$ distribution to measure $b\bar{b}$ correlations at ATLAS. a) Truth-level muons are shown in simulated events containing a J/ψ and a third muon. The open histogram represents the generated distribution of such muons. The dashed histogram represents the fraction of these that are the products of K/π decays. The dotted histogram represents events containing four b quarks. b) Reconstructed muons. All events where a J/ψ and a third muon have been reconstructed are shown, with the 4 b quark background shown by the dotted histogram. No K/π decays are reconstructed as good muons [16].

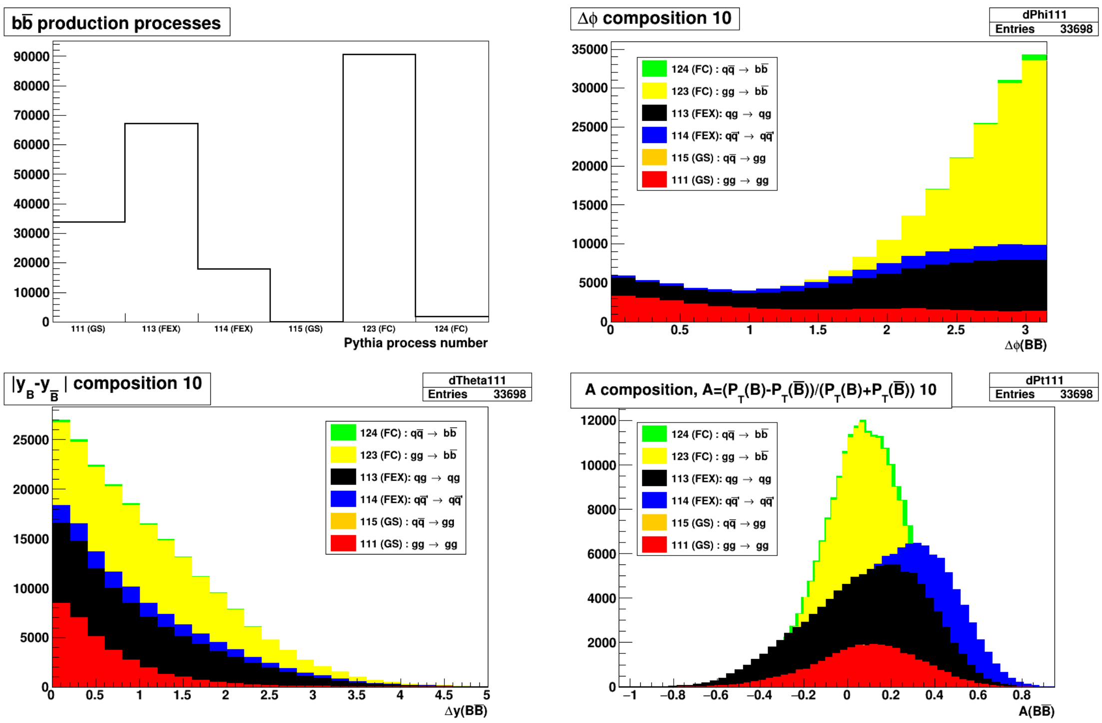

Figure 1.7.: The Pythia simulation showing the production mechanisms classes of the generated $B\bar{B}$ hadron pairs. The histogram on top left shows relative proportion of six Pythia QCD mechanisms generating bottom mesons. The figure on top right shows $\Delta\phi$ distribution, bottom left is difference in rapidities between the J/ψ and third muon and figure on the bottom right shows the distributions in p_T asymmetry parameter A. The processes are color coded. Red represents gluon splitting, yellow flavor creation and black and blue both represent flavor excitation class of processes. In making of these distributions it was required that both B hadrons have p_T greater than 10 GeV.

1.4. B hadron properties

Hadrons are color singlet combinations of quarks and can be considered to be bound states of their valence quarks and antiquarks. Because of the large b quark mass, B hadrons are considered to be heavy particles, with masses in the 5 to 10 GeV range. For a list of known B baryons and bottomonium states, see [6].

B meson is a particle containing c, s, u or d quarks besides a b quark. The relative production ratio at a hadron collider is approximately $B_d/B_u/B_s/B_c/b-$baryons $\approx 4:4:1:0.01:1$. B meson mass is in the range of 5.27-6.27 GeV and its typical lifetime is 1.5 ps, making its flight distance $c\tau \approx 0.5$mm. Properties of B mesons are listed in table 1.2. The b quarks decay in the lowest order via the radiation of a c quark and a virtual W^* boson. The decay process of a B hadron is similar, with the exception of one or more spectator quarks being involved. Higher order loop diagrams allow for special decay modes of B hadrons, such as $B_s \to \mu^+\mu^-$.

Table 1.2.: Valence quark composition, masses and lifetimes of unexcited states of B mesons [6].

Meson name	Composition	Mass [GeV]	Lifetime τ [ps]
B^0	$\mathrm{d\bar{b}}$	5.27958 ± 0.00017	1.519 ± 0.005
$\mathrm{B}^\pm$	$\mathrm{u\bar{b}}$	5.27926 ± 0.00017	1.638 ± 0.004
$\mathrm{B_s}$	$\mathrm{s\bar{b}}$	5.36677 ± 0.00024	1.512 ± 0.007
$\mathrm{B_c^\pm}$	$\mathrm{c\bar{b}}$	6.2756 ± 0.0011	0.452 ± 0.033

Experimentally, due to a long lifetime, the B hadron can be identified in a particle detector by searching for a secondary vertex, which is displaced from the beamline. The other favorable property of B hadrons is a large semileptonic branching fraction $\mathrm{Br}(B \to l + \nu + X) \approx 11\%$, where l denotes either $\mu^\pm$ or $e^\pm$.

1.5. B physics with the ATLAS detector

Even though ATLAS is designed as a general purpose detector for high-p_T physics, it is able to compete with dedicated B experiments such as LHCb.

The ATLAS B-physics programme covers two main aspects of the heavy flavor physics: measurements of production cross sections and production mechanisms of heavy flavor hadrons, either opened (B hadrons, charmed hadrons) or hidden (Onia). The important part of the early stages of the ATLAS B-physics programme is the measurement of production cross sections of beauty and charmed hadrons and of the heavy-flavor quarkonia, J/ψ and Υ, which provide sensitive tests of QCD predictions of production in proton-proton collisions at the LHC and validation of the MC tunes. Secondly, ATLAS is studying the properties of the entire family of B mesons (B^0 , $B^{\pm}$, B_s , B_c) and B baryons, thereby broadening the knowledge of both the spectroscopic and dynamical aspects of B-physics. Several studies have already been finalized and published:

- Measurement of J/ψ and Υ production cross sections
- Production cross sections and polarizations of B hadrons
- $B_s \to \mu^+\mu^-$ is a complementary measurement to the direct searches for physics beyond Standard Model using a di-muon trigger
- CP violation in $B_s \to J/\psi(\mu\mu) + \phi(K^+K^-)$ - according to the SM, only a small CP asymmetry is predicted. Deviations of weak mixing phase would be a clear signal for new physics. A very clean signature can be obtained by vertexing of J/ψ muons and ϕ kaons.
- Search for new states of quarkonia, where new triplet of χ_b states was found, see figure 1.8.
- Study of quarkonia with associated $W^{\pm}/Z^0$ production
- Study of open charm in D mesons

1.6. J/ψ properties

J/ψ is a bound state of a c quark and an antiquark. The J/ψ particle is a useful tool for reconstructing B hadron decays, since it is easily observable in the detector, as is shown in figure 1.12. The ATLAS B-physics triggers rely on this particle to identify B meson decays. The J/ψ lifetime is approximately $7.2 \cdot 10^{-21}$ s, and when it is produced in the decay of a B hadron it will decay in the same spot and thus mark the spot of B hadron decay. Its position can be precisely reconstructed from the di-muon vertex.

Prediction of a fourth quark, charm, was made by theoreticians in the GIM mechanism [18], which suppresses flavor-changing neutral current as well as $\Delta S = 2$ transitions in

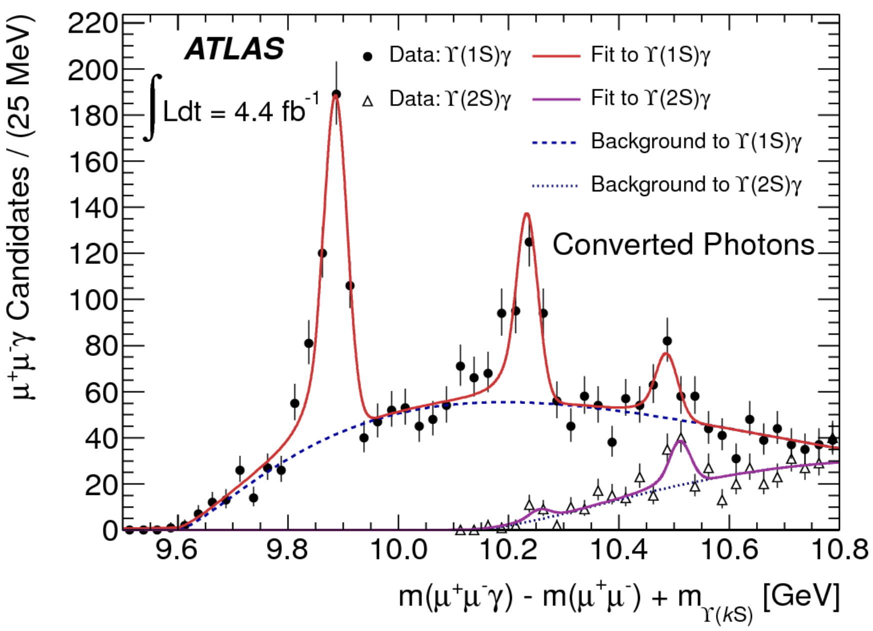

Figure 1.8.: The invariant mass distributions of $\chi_b \rightarrow \Upsilon(1, 2\mathrm{S})\gamma$ candidates using photons which converted into an e^+e^- pair in the inner detector (ID). The newly observed $\chi_b(3P)$ triplet is around invariant mass of 10.5 GeV. [17]

weak interaction. On November 10, 1974 two groups (one, a MIT group conducting an experiment on the east coast at Brookhaven National Laboratory, U.S.A. and the other a SLAC-Berkeley group doing experiment on the west coast at Stanford Linear Accelerator Center, U.S.A.) simultaneously announced the discovery of a new particle at invariant mass around 3095 MeV whose lifetime was about 1000 times longer than that of other particles of comparable mass. The BNL group studied di-electrons in the channel $p + \mathrm{Be} \rightarrow e^+e^- + X$ at beam energy of 28 GeV, the SLAC group employed channels $e^+e^- \rightarrow e^+e^-, \mu^+\mu^-$ and hadronic final states. In 1976, the two men who led those groups Samuel Ting and Burton Richter were awarded the Nobel prize in physics. The discovery plots are shown in figure 1.9.

In SLAC, other states were discovered at the SPEAR storage rings besides J/ψ. They were understood as the various excited states of the charmonium ($c\bar{c}$). Remarkably, it was shown later that the $c\bar{c}$ spectrum (shown in figure 1.10) can be well understood within the framework of non-relativistic quantum mechanics, with only a small spin-dependent corrections.

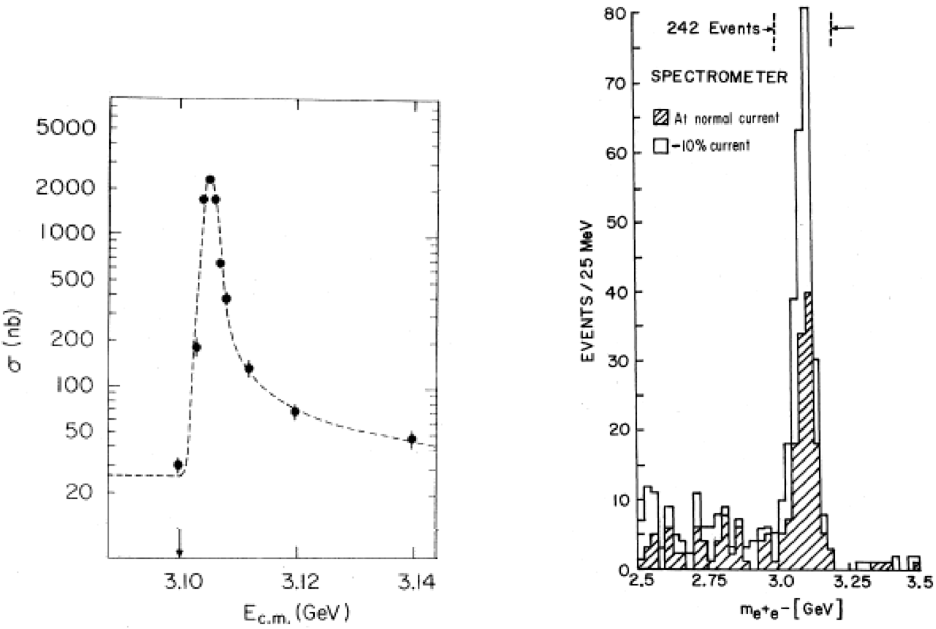

(a) SLAC **(b)** BNL

Figure 1.9.: The discovery plots of charmonium showing resonance in di-electron channels [19], [20].

Charmonium appears in various resonance states with different quantum numbers. The J/ψ and some of the other charmonium states are listed in table 1.3 together with the current knowledge of their mass and width.

State name	Spectroscopic notation [1]	mass [GeV]	Width [MeV]
η_c	1^1S_0	2.9836 $\pm$ 0.0007	32.2 $\pm$ 0.9
J/ψ	1^3S_1	3.096916 $\pm$ 0.000011	0.0929 $\pm$ 0.0028
ψ(2S)	2^3S_1	3.686109 $\pm$ 0.000014	0.299 $\pm$ 0.008
$\eta_c(2S)$	2^1S_0	3.6394 $\pm$0.0013	11.3 $\pm$ 3.2
h_c	1^1P_1	3.52538$\pm$ 0.00011	0.7 $\pm$ 0.4
χ_{c0}	1^3P_0	3.41475 $\pm$ 0.00031	10.5 $\pm$ 0.6
χ_{c1}	1^3P_1	3.51066 $\pm$ 0.00007	0.84 $\pm$0.04
χ_{c2}	1^3P_2	3.5562 $\pm$ 0.00009	1.93 $\pm$ 0.11

Table 1.3.: $c\bar{c}$ bound states under $D\bar{D}$ threshold listed by the Particle Data Group [6].

[1] $n^{2S+1}L_j$, where S=0,1 is the total spin of the quark and antiquark, L = 0,1,2 ... (or $L = S, P, D$,...) is the orbital angular momentum and j is the total angular momentum. The n is the radial excitation of the system.

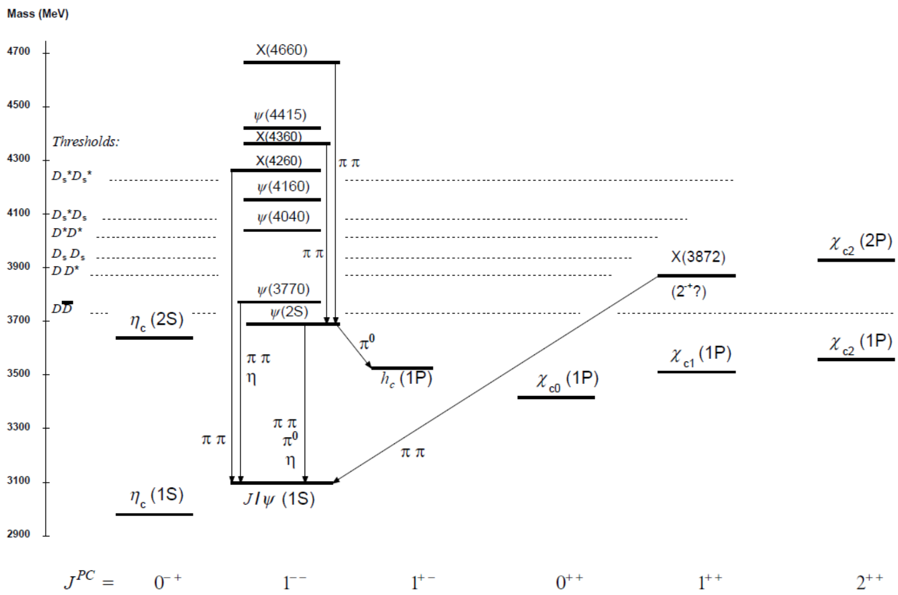

Figure 1.10.: The level scheme of the $c\bar{c}$ states showing experimentally established states with solid lines. Singlet states are called η_c and h_c, triplet states ψ and χ_{cJ}, and unassigned charmonium-like states X. Figure from [6].

The J/ψ resonance is very narrow because the J/ψ decays into an open charm is kinematically blocked ($\mathrm{m}(J/\psi) < \mathrm{m}(D\bar{D})$), and the decay of $J/\psi \to ggg \to$ hadrons is suppressed. The decays are illustrated in figure 1.11. Since the bottom and charm quarks are heavy, non-relativistic description of QCD (NRQCD) is possible. The NRQCD separates the perturbative and non-perturbative processes using the factorization theorem:

$$d\sigma_{pp\to J/\psi+X} = \sum_{i,j} \int dx_i dx_j f_i(x_i, \mu_F^2) f_j(x_j, \mu_F^2) \sum_n d\hat{\sigma}(i + j \to c\bar{c}[n] + X) \langle \mathcal{O}^{J/\psi}[n] \rangle,$$

where $d\hat{\sigma}(i + j \to c\bar{c}[n] + X)$ is the perturbative prediction of cross section for the production of $c\bar{c}$ in a state n and $\langle \mathcal{O}^{J/\psi}[n] \rangle$ are the corresponding non-perturbative elements describing that a state n will produce J/ψ. Gluon fusion processes give the highest contribution to the cross section due to the large gluon densities of the high-momentum protons.

In general, there are three sources of J/ψ production at a hadron collider:

1. Direct production in a pp collision, also called prompt production

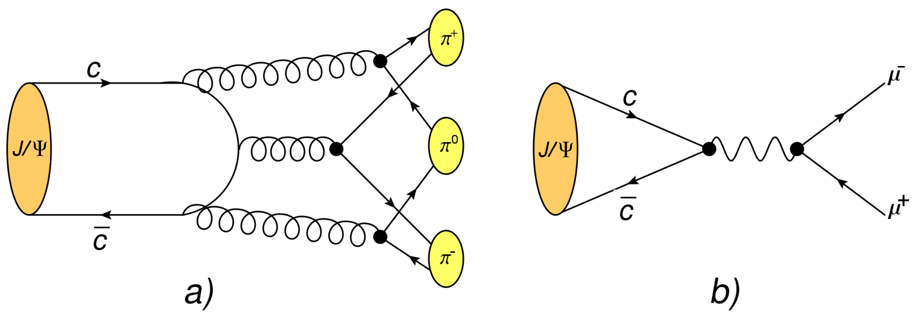

Figure 1.11.: Feynman diagrams for a) strong force decay $J/\psi \to \pi^+\pi^0\pi^-$ and b) $J/\psi \to \mu^+\mu^-$ electromagnetic decay.

2. Production in a decay of B hadron - characterized by a displaced J/ψ decay vertex, also referred to as non-prompt production

3. De-excitation of a higher charmonium state

1.6.1. Direct J/ψ production in pp collisions

The J/ψ particle at the LHC is produced by interactions between partons (quarks and gluons) inside the colliding protons. Quarks and gluons interact via the strong force as is described in the QCD theory. An extensive overview of quarkonia properties and production can be found in [21]. Several quarkonia production mechanisms have been devised to provide predictions:

- J/ψ production was originally described by the Color Singlet Model (CSM), which emerged shortly after the discovery of J/ψ. The $c\bar{c}$ pair is assumed to be produced with quantum numbers of the state it eventually evolves into, the leading order process of the CSM is $gg \to c\bar{c}[1^3S_1] + g$. An extensive overview can be found in [22]. The CSM was considered a good model until TeVatron experiments showed that it gravely underestimates the inclusive J/ψ cross section [23].

- The Color Octet Model (COM) assumes that a $c\bar{c}$ bound state is produced in a color octet state, then this state radiates a gluon and becomes colorless. One of the problems of this model is predictions for spin alignment of J/ψ which do not fit the data.

- In the Color Evaporation Model (CEM), $c\bar{c}$ bound state is produced in a color octet state, these quarks emit one or more gluons and form a colorless charmonium

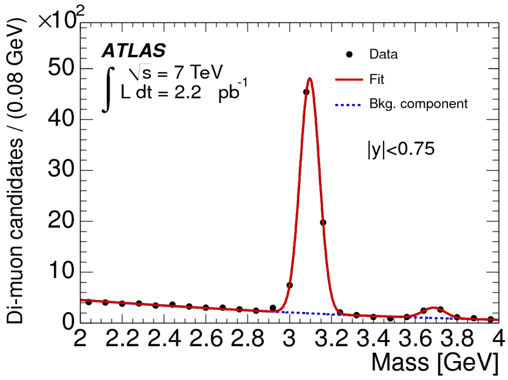

Figure 1.12.: Invariant mass distribution of reconstructed $J/\psi \rightarrow \mu\mu$ candidates used in the cross section analysis, corresponding to an integrated luminosity of 2.2 pb^{-1}. The points are data, and the uncertainties indicated are statistical only. The solid lines are the result of the fit. [24]

meson. The perturbative and non-perturbative parts of the production process are completely uncorrelated. It predicts that there is no color connection between the color and angular momentum quantum numbers with which the $c\bar{c}$ pair is produced and the quantum numbers of the formed quarkonium state. It has enjoyed a considerable phenomenological success, but in its original formulation it has fallen out of favor.

1.7. Previous studies of $b\bar{b}$ production

Several measurements of b quark pair azimuthal correlations have been performed, at the Sp$\bar{\text{p}}$S collider experiment UA1, at both TeVatron experiments, D0 and CDF and recently at the CMS experiment.

1.7.1. Sp$\bar{\text{p}}$S study at $\sqrt{s}$ = 630 GeV

The UA1 experiment at the Sp$\bar{\text{p}}$S has performed the measurement [25] of angular correlations in $p\bar{p}$ collisions at the center of mass energy $\sqrt{s}$ = 630 GeV. The study is based on the 10^8 $b\bar{b}$ events produced within the UA1 detector during the 1988-1989 run period with total integrated luminosity of 4.7 pb^{-1}. Both bottom hadrons are required to decay semileptonically into inclusive muons with transverse momentum $p_T > 3$ GeV. This yielded a total event sample of 3846 events.

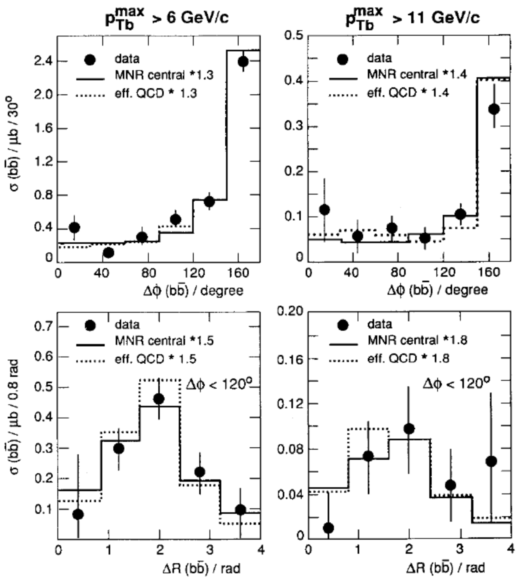

Figure 1.13.: The UA1 measured $b\bar{b}$ pair angular distributions $\Delta\phi$ and ΔR with a p_T of the higher p_T quark > 6 GeV (left) and > 11 GeV (right). Errors are statistical only. Shown are the distributions for $\Delta\phi$ (top) and ΔR (bottom). Also shown are the central pQCD predictions from the calculation of Mangano, Nason, and Ridolfi (MNR) and the prediction of the effective QCD Monte Carlo (ISAJET) used for the acceptance calculation. Figure from [25].

The di-muon data tag was used to select events with hadrons with produced b and $\bar{b}$ quarks, and using angular correlations method, the cross sections were derived and compared to the $\mathcal{O}(\alpha_s^3)$ theoretical predictions. There is a strong correlation between the properties of a parent b quark and the resulting semileptonic decay muon. In order to separate Drell-Yan and heavy flavour contributions, events were classified according to the muon charge and isolation, or the hadronic activity around the muon in the cone of $\Delta R = \sqrt{\Delta\phi^2 + \Delta\eta^2} < 0.7$. The isolation was defined as:

$$I = \sqrt{(\sum_i E_T/2)^2 + (\sum_i p_T)^2},$$

where E_T is sum of transverse energies of particles. The distributions were fitted simultaneously for the dimuon mass distribution in the range of $2\mathrm{m}_\mu < \mathrm{m}_{\mu\mu} < 35\,\mathrm{GeV}$, the $\Delta\phi(\mu\mu)$ for non-isolated events with $\mathrm{m}_{\mu\mu} > 4\,\mathrm{GeV}$ independent of the muon charge and $\Delta R(\mu\mu)$ distribution for the same events with requirement of $\Delta\phi(\mu\mu) < 120°$. For their ΔR and $\Delta\phi$ results see figure 1.13.

The measured total inclusive cross section was found to be $\sigma_{tot}(p\bar{p} \to b\bar{b} + X) = 19.7 \pm 4.3_{exp} \ {}^{+10.4}_{-6.5th} \ \mu b$. The measured $b\bar{b}$ angular distributions were found to be in a good

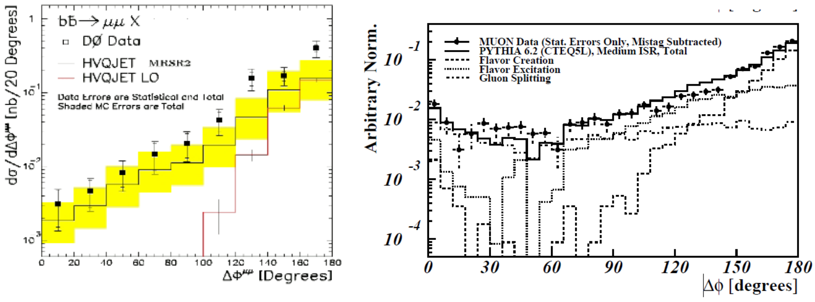

Figure 1.14.: Distributions of $b\bar{b}$ azimuthal angle distribution from the D0 and the CDF experiments at the Tevatron. Images are taken from [27] and [26].

agreement with the contemporary NLO QCD predictions and were phenomenologically reproduced by the ISAJET Monte Carlo. This measurement firmly established a sizable contribution from the higher-order QCD processes with a high significance.

1.7.2. TeVatron study at $\sqrt{s} = 1.8$ TeV

B-physics was amongst the areas of intense study for both TeVatron experiments, CDF [26] and D0 [27]. Similar measurements of angular correlations have been done at the TeVatron in the dimuon channel during RUN 1 $\sqrt{s} = 1.8$ TeV. The D0 experiment measured b quark production cross section for $|y^b| < 1.0$ and p_T^b greater than 6 GeV which was extracted from the single muon and dimuon data samples. The CDF used a different approach, it studies $b\bar{b} \to (J/\psi + X)(\ell + X')$ channel events, where the charged lepton (ℓ) is an electron $(e^{\pm})$ or a muon $(\mu^{\pm})$, to measure $\Delta\phi$ between bottom quarks.

The D0 results [28] agree in shape with the NLO QCD calculation of heavy flavor production, but are greater than the central values of these predictions. The angular correlations between b and $\bar{b}$ quarks, measured from the azimuthal opening angle between their decay muons, also agree in shape with the NLO QCD prediction. The CDF results [29] of measurements are consistent with the parton shower Monte Carlo (MC) models of Pythia and Herwig, and with the NLO QCD predictions. Neither non-perturbative nor supersymmetric production mechanisms are needed in order to describe the measured $\Delta\phi$ spectra. It is shown that the significant fraction of the $b\bar{b}$ pairs is produced with small $\Delta\phi$ and that flavor excitation and gluon splitting play a significant role in the $b\bar{b}$ production at the Tevatron. The observed distributions of $\Delta\phi$ are shown in figure 1.14. In conclusion, the NLO $b\bar{b}$ production has been observed at the TeVatron, where the shape of the $b\bar{b}$ azimuthal angular distribution was reproduced, but the normalization was underestimated by the theory.

1.7.3. CMS study at $\sqrt{s} = 7$ TeV

The measurements [30] are based on data corresponding to an integrated luminosity of 3.1 ± 0.3 pb $^{-1}$ recorded by the CMS experiment during the 2010 data taking period. The detection of the B hadrons is based on the reconstruction of the secondary vertices from their decays. The differential cross section of $B\bar{B}$ pair production is measured as a function of the angular separation variables ΔR and $\Delta\phi$ between the two reconstructed B hadrons for three different energy scales. Since this analysis relies on the reconstruction of two b-jets, at low angular separation these jets merge and it is difficult to reconstruct them. Therefore, gluon splitting processes are hard to observe.

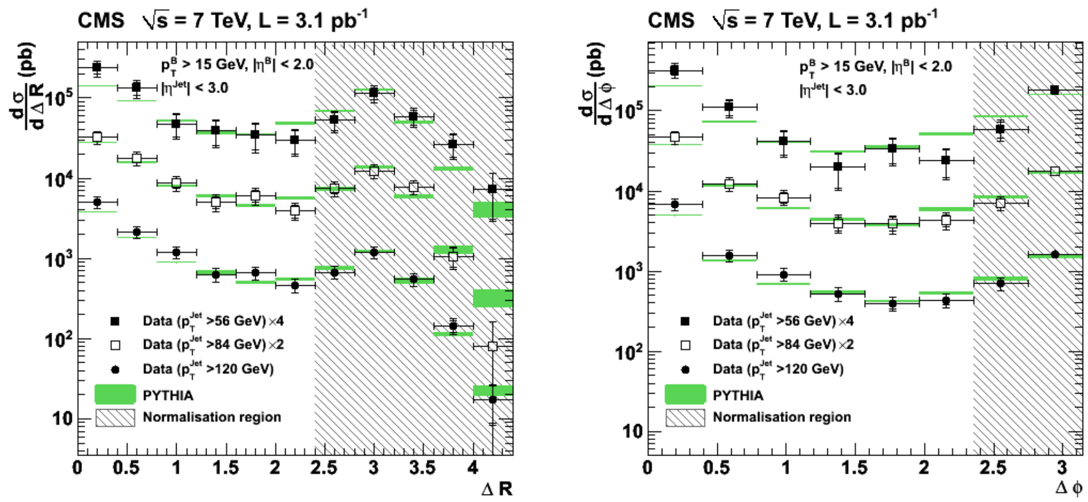

(a) Differential $B\bar{B}$ production cross section as function of ΔR

(b) Differential $B\bar{B}$ production cross section as function of $\Delta\phi$

Figure 1.15.: The differential BB production cross section as measured by the CMS detector. The MC is normalized to the shaded region of $\Delta R > 2.4$. Images are taken from [31].

The data exhibit a substantial enhancement of the cross section at small angular separation, exceeding the values measured at large ΔR and $\Delta\phi$, see figure 1.15. The fraction of cross section in this collinear region is found to increase with the leading jet p_T of the event.

Chapter 2.

Monte Carlo Generators

In general, for contemporary high energy experiments which collide hadrons at high energy, it is impossible (or too complicated to be practical) to make predictions based solely on analytical calculations based on the first principles of the SM field theory. Under the circumstances, one has to rely on predictions made by Monte Carlo event generators. Today, a wide variety of such event generators exist, some general-purpose and some specialized [32], [33].

The ATLAS software framework allows the use of numerous event generators, which communicate with ATLAS software packages via HepMC interface [34]. The multi-purpose generators available to the user are:

- Pythia 6.4 and 8
- Herwig++
- Sherpa

These generators are primarily leading-order generators, since NLO and NNLO predictions and matrix elements are available only for a handful of processes, because they are calculable only for low final state multiplicity. In the generator QCD simulation, the NLO effects are simulated using the parton shower (PS) approach. Higher order QCD corrections have significant impact on production cross sections, especially in the case of $b\bar{b}$ production mechanisms where NLO processes dominate. Usually MC generators such as Pythia only have predictions for LO matrix elements, which insufficiently cover the phase space. The parton showers and matrix elements are good approximations in two different phase space regions. Full matrix element calculations are appropriate for hard collisions, where a few states with large p_T are expected, such as jets, while parton shower approximations are suitable for studies of low p_T states and for emissions of collinear partons, such as in studies of jet structure. The parton shower mechanism in a MC generator serves two main purposes: to provide an estimate of higher-order corrections that are enhanced by large kinematic logarithms and at the same time to generate high-multiplicity parton states which can then be converted into the observable hadrons via hadronization. Therefore, in regions where higher order terms are required to give satisfactory approximation, the MC generators use the technique of parton showers, which to some extent approximates the higher order terms. At each step in the shower evolution, the emission probability is calculated for each parton and emissions are generated. The parton showers can be subdivided into two types with relation to the hard process, the ISR and FSR [35]. ISR describes how the incoming proton dissolves into partons before the collision, while FSR takes the products of the hard process and performs branchings into new particles. In general, the event generation starts with sampling of PDFs, a chosen hard collision process and then generator combines LO matrix elements with parton showers, multiple parton interactions and finally hadronization model to simulate the outcome of a collision. The example of a $b\bar{b}$ event is shown in figure 2.1.

2.1. Pythia8

Pythia is a high-energy physics event generator [36], [37]. It allows simulations of wide assortment of Standard Model and BSM processes. Historically it descends from JETSET package [38].

Previous versions od Pythia, such as Pythia 6, were written in Fortran 77 language. New requirements of the LHC experimental community presented an opportunity to rewrite it and clean it into a new C++ version. Pythia8 is currently able to simulate pp, $\bar{p}p$, e^+e^- and $\mu^+\mu^-$ collisions, ep, γp and $\gamma\gamma$ collisions are not yet supported.

Concerning PS, Pythia8 uses showers ordered in p_T, which has an advantage over mass ordered showers (used in the previous version Pythia6.4). In a pp collision, there can be more partons from each proton that interact, giving rise to the so-called multi-parton interaction (MPI). Pythia8 employs MPI framework which simulates the additional interactions besides the hard process. As the collision center-of-mass energy increases, more partons at smaller x interact and more particles can be produced in the ISR. Multiple interactions are therefore increasing with increasing collision energy and the models for multiparticle interactions are put to the test as the $\sqrt{s}$ at LHC increases.

Process	Matrix element ($\frac{\langle \lvert M \rvert^2 \rangle}{g^4}$)
$q_\alpha q_\beta \to q_\alpha q_\beta$	$\frac{2}{9}(\frac{2(s^2+u^2)}{t^2} + (\frac{2(t^2+s^2)}{u^2} - \frac{1}{3}\frac{4s^2}{ut})\delta_{ab})$
$q_\alpha \bar{q}_\beta \to q_\alpha \bar{q}_\beta$	$\frac{2}{9}(\frac{2(s^2+u^2)}{t^2} + (\frac{2(t^2+u^2)}{s^2} - \frac{1}{3}\frac{4u^2}{st})\delta_{ab})$
$qg \to qg$	$1 - \frac{us}{t^2} - \frac{4}{9}(\frac{s}{u} + \frac{u}{s}) - 1$
$gg \to q\bar{q}$	$\frac{1}{6}(\frac{u}{t} + \frac{t}{u}) - \frac{3}{4}(1 - \frac{ut}{s^2}) + \frac{3}{8}$
$q\bar{q} \to gg$	$\frac{8^2}{3^2} M(gg \to q\bar{q})$
$gg \to gg$	$\frac{8}{9}(-\frac{33}{4} - 4(\frac{us}{t^2} + \frac{ut}{s^2} + \frac{st}{u^2})) - \frac{9}{16}(45 - (\frac{s^2}{ut} + \frac{t^2}{us} + \frac{u^2}{ts}))$

Table 2.1.: The list of $2 \to 2$ processes with matrix elements currently supported by Pythia8. The normalization is such that $\frac{d\sigma}{dt} = \frac{1}{16\pi s^2}\langle \lvert M \rvert^2 \rangle$. Taken from [36].

Rescaled parton densities are defined after the first interaction, taking into account the nature of the previous partons which have already interacted [36]. Since the Pythia 6.4, the ISR, FSR and MPI were intertwined into one common decreasing p_T sequence.

2.1.1. PDFs anf MC tunes

Pythia framework allows for usage of many different libraries with parton density functions [39]. The Les Houches Accord for user processes (LHA) [40] is the standard way to input parton-level information from a matrix-elements-based generator into Pythia. Concerning the Monte Carlo studies presented in this thesis, CTEQ6L1 ATLAS tune was used [41]. More information about this tune and comparison with data can be found in [42].

2.1.2. Pythia8 QCD processes

There are six QCD processes modeled in Pythia8, all in a LO approximation. Comparison of those differerent QCD subprocesses and their matrix elements available in Pythia 8 is shown in table 2.1.

Pythia8 contains phenomenological models of hard processes that provide approximations to the flavor creation, flavor excitation and gluon splitting mechanisms [36]. They are made by combining hard process with parton shower.

Flavor creation processes (FC) ($gg \to b\bar{b}$, $qq \to b\bar{b}$), flavor excitation (FEX) ($gb \to gb$, $qb \to qb$) and gluon splitting (GS) ($g \to b\bar{b}$). These three QCD mechanisms are represented in the following processes, shown with Pythia8 process number:

- **isub 114**: $q + \bar{q} \to q + \bar{q}$: FEX, if ISR gluon splits into a $b\bar{b}$ pair, one of b-quarks is boosted
- **isub 124**: $q + \bar{q} \to b + \bar{b}$: LO FC process, direct production of $b\bar{b}$ pair. It produces events with back-to-back topology.
- **isub 115**: $q + \bar{q} \to g + g$: GS, when one of the two final state gluons splits into a $b\bar{b}$ pair
- **isub 113**: $q + g \to q + g$: FEX process, if ISR gluon splits into a $b\bar{b}$ pair, one of b-quarks is boosted via interaction with g
- **isub 123**: $g + g \to b + \bar{b}$: LO FC process, direct production of $b\bar{b}$ pair. It produces events with back-to-back topology.
- **isub 111**: $g + g \to g + g.$: GS, final state gluon splits into a $b\bar{b}$ pair

An event is considered to be FC when a $b\bar{b}$ quark pair is outgoing from the hard process. In principle, the FC is a leading-order process but it can become NLO when ISR and FSR are counted in. The GS production mechanism occurs when a $b\bar{b}$ pair originates from a single gluon. This gluon can be an outgoing hard scattering gluon or a shower gluon. It is possible that more than one $b\bar{b}$ pair is produced in the final state. However, this occurs in less than 5 percent of $b\bar{b}$ events generated by Pythia.

The produced b and $\bar{b}$ quarks (and subsequently B hadrons) have distinct shapes in distributions of certain characteristic variables for different production mechanisms. Furthermore, each $b\bar{b}$ production mechanism has a distinct shape in these variables as shown in Figure 1.7. The distinct characters of the distributions are exploited to extract the fractions for three $b\bar{b}$ production mechanism clases.

2.1.3. Pythia8 parton shower

When a higher order QCD event topologies are required to describe the experimental data, matrix element treatment is often impractical or even impossible due to the number of Feynman diagrams rising factorially. A parton shower approach can be used as an approximate pQCD treatment. Algorithmically, it can be implemented as an iterative code of applying branchings up to a certain cut off where partons stop showering. The parton shower is designed to simulate QCD radiation in the collinear limit and in the soft limit.

In the event generator picture, a QCD particle shower may be viewed as a sequence of $1 \to 2$ particle branchings. In the parton shower view, these branchings are given as a functions of momentum transfer scale Q^2 and momentum fraction z variables. In the case of QCD parton showers, the relevant branchings are:

- $g \to gg$
- $q \to qg$
- $g \to q\bar{q}$

These algorithms are referred to as leading-log showers and employ branching according to the DGLAP splitting kernels [36]:

$$P_{q\to qg}(z) = C_F \frac{1+z^2}{1-z}$$

$$P_{g\to gg}(z) = N_C \frac{(1-z(1-z))^2}{z(1-z)}$$

$$P_{g\to q\bar{q}}(z) = T_R(z^2 + (1-z)^2)$$

with C_F=4/3, N_C=3, $T_R = n_f/2$. The $P_{a\to bc}(z)$ is interpreted as the branching probability of the parton a. The variable z defines momentum sharing between partons b and c, where parton b is taking fraction z of the original parton a momentum and parton c is left with fraction of $1-z$ of the original a momentum.

The variable $t = \ln(\frac{Q^2}{\Lambda^2})$, where Λ is the QCD scale, is useful in understanding evolution of parton showers. In the context of parton shower evolution, it can be understood as a time coordinate. For a give value of t coordinate, the branching probability over all allowed z values can be expressed as: $I_{a\to bc}(t) = \int_{z_-(t)}^{z_+(t)} dz \frac{\alpha_s}{2\pi} P_{a\to bc}$ [36]. The probability of no branching in the time interval (t_0, t) is defined as

$$P_{NB}(t_0, t) = e^{-\int_{t0}^{t} dt' \sum_{b,c} I_{a\to bc}(t')}$$

The probability of not branching P_{NB} is referred to as Sudakov form factor.

It might appear that the parton shower approximation takes into account only the collinear-enhanced real parton emissions at each order in perturbation theory and neglects the virtual (loop) effects of the same order. However, this is not the case: such effects are included in the probability of not splitting during evolution from scale t_0 to t , which is given by the Sudakov form factor.

Since version 6.3, PYTHIA uses p_T ordered parton showers for the ISR and FSR. The parton shower approach is not a complete (N)NLO simulation of $b\bar{b}$ production based on full matrix elements up to and including the order of $\approx \alpha_s^3$ diagrams and their interference. It is a leading-log approximation to higher-order processes. However, it can be regarded as a useful QCD model of $b\bar{b}$ production to be confronted with LHC data.

2.1.4. Hadronization model in Pythia8

Hadronization is a mechanism for transforming colored partons into colorless hadrons. The hadronization model in Pythia8 is based exclusively on the Lund string fragmentation framework [43]. In QCD for large quark separation distances, color field lines are compressed to a tube-like regions due to the self-interaction among gluons.

Since the non-perturbative QCD is not analytically solvable, results from hadron spectroscopy (such as quarkonia spectra) and lattice QCD calculations [44] show that the color flux tube between $q\bar{q}$ pair can be well approximated by a inter-quark potential (so called Cornell potential)

$$V(r) = -k \cdot r + \frac{4}{3}\frac{\alpha_S}{r}$$

If the short-distance Coulomb term is neglected, the corresponding linear potential can be expressed as $V(r) = -k \cdot r$, where k is the string tension, is about 1 GeV/fm. When breaking the string, the $q\bar{q}$ pair is created on the spot, but it can QM tunnel to transverse momentum space. The flavour composition of the created $q\bar{q}$ pair is assumed to derive from a quantum mechanical tunneling process, which in turn implies a suppression of heavy quark production $u : d : s : c \approx 1 : 1 : 0.3 : 10^{-11}$ such that charm and bottom production can be neglected in the hadronization step [37]. This implies that production of D and B hadrons in hadronization is negligible.

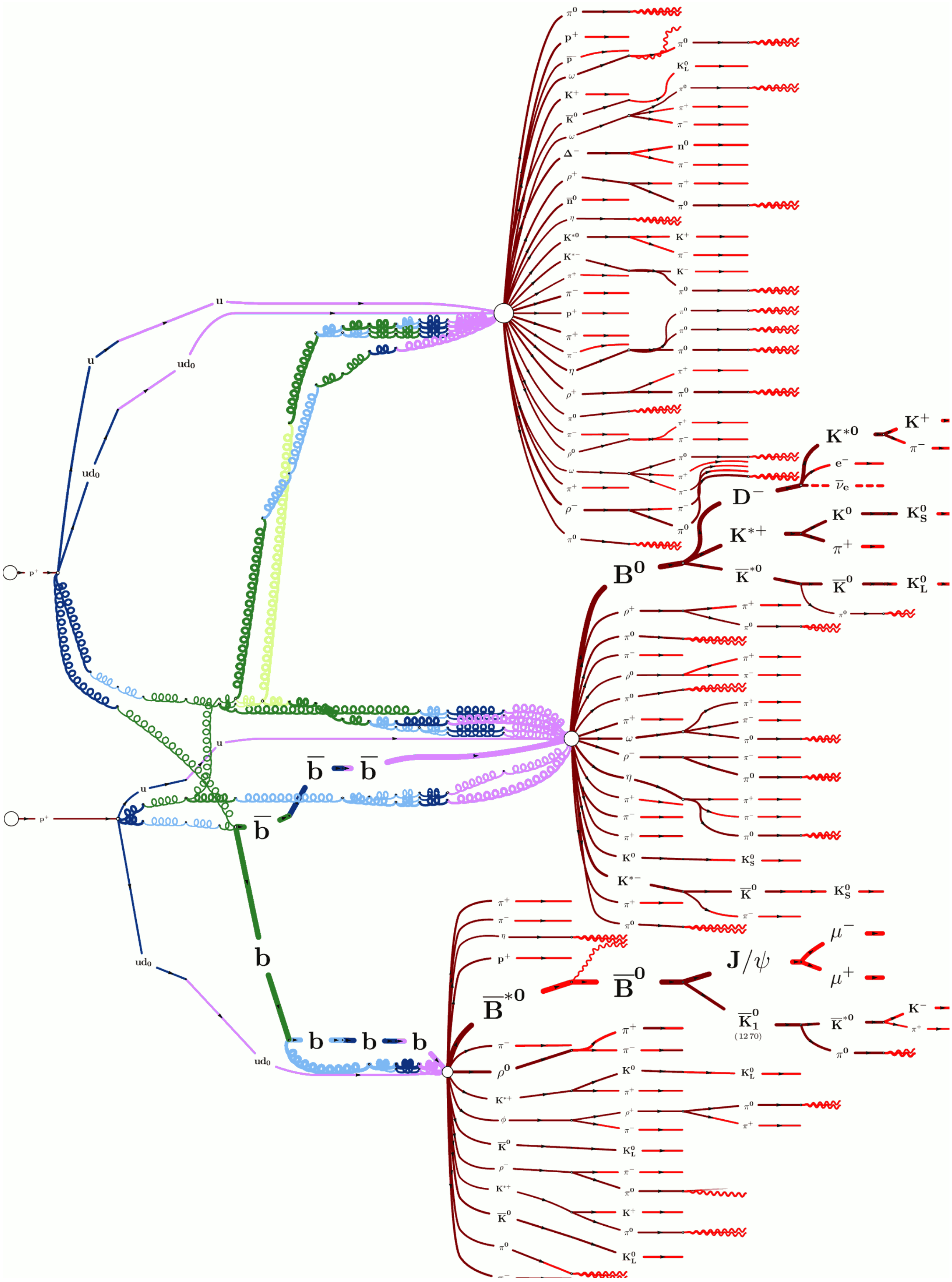

Figure 2.1.: A schematic picture showing a Pythia 8 $pp \to BB + X \to J/\psi + Y$ event. Red color denotes a "stable" particle which is simulated by Geant4. Other colors correspond to Pythia status codes, such as pink is partons just before hadronization, brown denotes stable hadrons emerged in hadronization, light blue marks the final state radiation while dark blue is the initial state radiation.

Chapter 3.

ATLAS experiment

3.1. The LHC

The Large Hadron Collider (LHC) at CERN is a synchrotron-type accelerator and a storage ring located near Geneva, Switzerland. It has circumference of 26.659 km and it occupies the same tunnel where the Large Electron-Positron collider (LEP) [45] resided until 2001.

3.1.1. The LHC

The LHC is divided into 8 octants. It collides particle beams in 4 interaction points, where four large experiments are located. The experimental programme of the LHC consist of proton-proton and lead ion collisions.

In the case of proton collisions at the LHC, the accelerator is designed to collide 7 TeV proton beams distributed in 2808 bunches, each containing about $1.15 \cdot 10^{11}$ protons. At nominal conditions, LHC can deliver instantaneous luminosity $\mathscr{L} = 10^{34}$ cm^{-2}s^{-1}. The source of protons is pure hydrogen gas. The duoplasmatron ionizes protium, separates protons from electrons and a continuous proton beam with energy of about 92 keV and current of about 300 mA is created. Continuous stream of protons is bunched and pre-accelerated in a 4-vane radiofrequency quadrupole (RFQ) with and an output energy of 750 keV. The bunched beam is then fed into Linac2, an Alvarez-type linac first run in 1978, which provides pulsed beams of up to 175 mA intensity at 50 MeV output energy. An 80 meter-long beam transport tube then carries the linac beam to proton synchrotron booster (PS) , which accumulates the beam, combines proton bunches and accelerates

Beam conditions	nominal	2010	2011	2012
E_B	7	3.5	3.5	4
Peak $\mathscr{L}$ [cm^{-2}s^{-1}]	10^{34}	2.1×10^{32}	3.7×10^{33}	7.7×10^{33}
$\int \mathscr{L}$ [fb^{-1}]	–	0.04	6.1	23.1
β^* [m]	0.55	3.5 / 2	1.5 / 1	0.6
N_{BP}	1.15×10^{11}	1.2×10^{11}	1.45×10^{11}	1.7×10^{11}
N_B	2808	368	1380	1380
Spacing [ns]	25	150	50	50
E_{BS}	362	28	110	140
$\langle\mu\rangle$	19	4	17	37

Table 3.1.: The evolution of LHC proton beam parameters during the LHC Run 1. The E_B denotes beam energy, N_{BP} number of protons per bunch, N_B number of bunches, β^* denotes the optical β function, μ is mean number of multiple proton interactions per bunch crossing. [46]

them to 1.4 GeV. It is expected that Linac2 will be superseded by Linac4, which is now in the commissioning phase as of 2015. It should provide a 160 MeV high-intensity beam for superluminosity LHC (SLHC) running. The whole LHC accelerator chain is shown in figure 3.1.

In addition to protons, the LHC is also designed to accelerate and collide the ^{208}Pb nuclei. Concerning the ion collisions, the high-energy accelerating chain is able to accommodate a beam of ^{208}Pb^{54+} highly-ionized lead atoms. The beam begins its path in an 18 GHz electron cyclotron resonance (ECR) ion source which produces ^{208}Pb^{27+} ions at about 2.5 keV/u. This beam is accelerated in a similar RFQ and Linac3 to 4.2 MeV/u, after which a 1 μm thick carbon foil strips lead ions of additional electrons to a charge state distribution centered around ^{208}Pb^{54+}. These ions are then selected from an ion mixture in a magnetic spectrometer before being transported to the accumulator Low Energy Ion Ring (LEIR), where the ions are accelerated up to 72 MeV/u and directed towards the PSB, and then follow a similar accelerating path as protons.

The evolution of the LHC parameters during the Run 1 period compared to design values is shown in table 3.1.

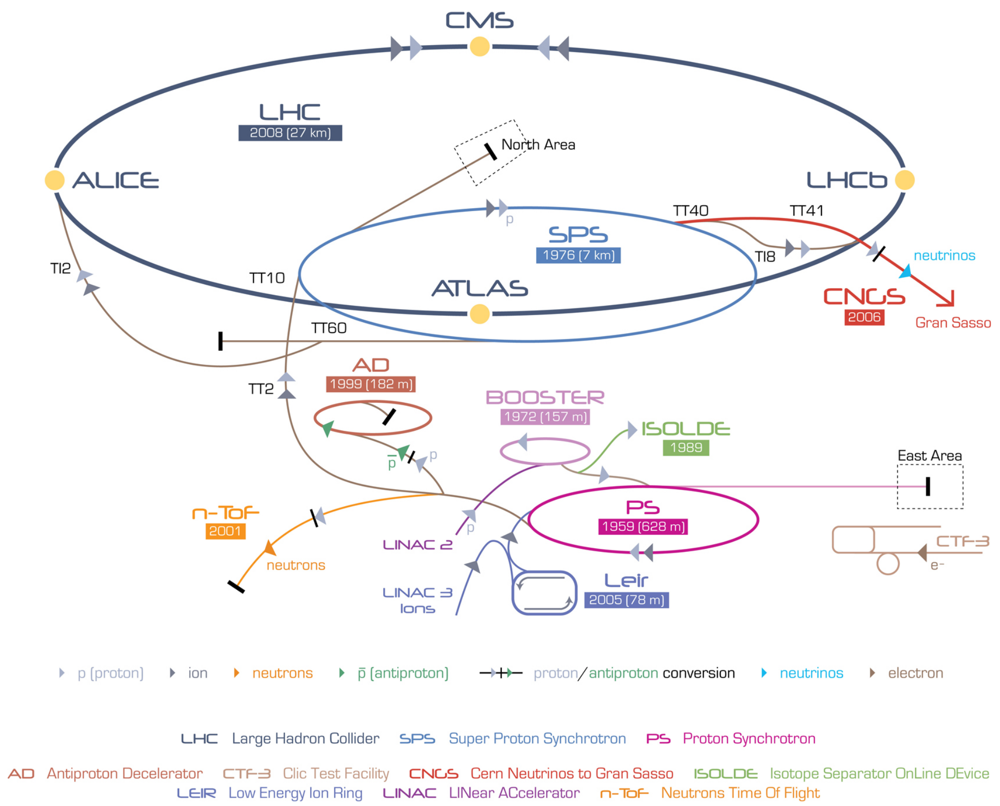

Figure 3.1.: The CERN accelerating chain is a succession of machines which accelerates particles to an increasingly higher energy. In the case of protons, the first regular acceleration stage is the Linac2, which accelerates them to 50 MeV. The beam is then injected into the PSB, which accelerates particles to 1.4 GeV, followed by a proton synchrotron (PS), which energizes them to 25 GeV. Protons are then sent to the SPS, where they are accelerated to 450 GeV and injected into beamlines of the LHC machine. Besides the LHC, CERN complex also hosts Antiproton decelerator, ISOLDE facility, fixed-target experimental halls, CNGS beam apparatus, nTOF and the Clic test facility (CTF).

3.1.2. Experiments

There are four large and two smaller experiments located on the LHC ring:

- ATLAS (**A** **T**oroidal **L**HC **A**pparatu**S**) is a general-purpose detector designed to cover the widest possible range of physics at the LHC. ATLAS is the largest collider detector ever constructed. Its components will be described in more detail in the following sections.
- CMS (**C**ompact **M**uon **S**olenoid) is another general-purpose detector on the LHC. The design of its magnetic system is simpler than in the case of ATLAS, but its solenoid is capable of generating a homogeneous 3.8 T magnetic field allowing precise

measurement of particle momenta. As the name suggests, it was designed with precision muon tracking in mind. Even though the CMS and ATLAS detectors have very similar physics programmes, their layout design and choices of subdetector technologies are diverse. The CMS and ATLAS detectors were designed to complement each other in order to extend their physics reach and to provide cross-check of results.

- LHCb (**L**arge **H**adron **C**ollider **b**eauty) is an asymmetric detector which utilizes the LHC as a B hadron factory. It has a set of subdetectors optimized for precise reconstruction of B hadron candidates and low-p_T particle identification. It's rapidity coverage matches the area of maximum b-production at LHC energies. It's physics programme comprises study of exotic quark bound states, study of the CP-violation in B hadron decays, neutral B and D meson oscillations and search for BSM physics in rare decay channels such as $B_s \to \mu\mu$.

- ALICE (**A** **L**arge **I**on **C**ollider **E**xperiment) is a detector optimized for study of ion-ion collisions with high track multiplicity and low-p_T final states. Its physics programme focuses decidedly on lead ion collisions studies and it is trying to observe matter in the quark-gluon plasma state.

- TOTEM (**TOT**al **E**lastic and diffractive cross section **M**easurement) is one of smaller experiments at the LHC ring distributed around the CMS detector. As the name suggests, it aims to measure the effective cross sections of the elastic, diffractive and total proton-proton interactions at the LHC.

- LHCf (**L**arge **H**adron **C**ollider **f**orward) is the smallest experiment at the LHC. It uses the LHC protons to simulate atmospheric interactions of very high-energy particles occuring in aerial astroparticle physics.

The following section is dedicated to the inner working of the ATLAS experiment.

3.2. ATLAS apparatus

Historically, the concept of ATLAS detector descends from two experiments proposed in the early 1990's, the ASCOT (**A**pparatus with **S**uper **CO**nducting **T**oroids) and the EAGLE (**E**xperiment for **A**ccurate **G**amma, **L**epton and **E**nergy measurements). In 1992, the collaborations merged and produced a letter of intent [47], which served as a basis for the future ATLAS design proposal. The construction of the detector was completed in 2008.

The high energy and large luminosity provided by the LHC machine allow the ATLAS detector to investigate a wide range of physics phenomena. The need to cover a wide range of assorted physics signatures of final states has governed the design of the detector. In general, the ATLAS physics programme can be divided into two parts: study and precise measurements of properties of particles and interactions of the SM, and search for new phenomena of BSM physics. At the focal point of the physics programme was the search for the Higgs boson. Since its discovery in 2012, the task has moved onto understanding the properties such as mass, parity and couplings of the new-found particle [48], [49]. It represents only a small part of the performed complex of studies related to the phenomena of the electroweak symmetry breaking, which includes precise measurements of $W^\pm$ and top-quark masses and measurements of triple gauge couplings. Other SM studies include measurements and testing of QCD processes, which make up most of the background at the LHC, top quark properties and CP violation in B decays. Concerning the BSM physics, direct and indirect searches for particles predicted by various supersymmetric models are being conducted. Theoretical predictions are being compared to the measurements, and limits are set. Other BSM topics include search for new gauge bosons, search for quark substructure, dijet resonances and extra dimensions.

3.2.1. ATLAS detector system

ATLAS is a general-purpose detector with almost 4π solid angle coverage [50]. It is optimized for high p_T physics[1]. It consists of four main subdetector components shown in figure 3.2. The closest to the beam pipe is the Inner Detector (ID) which provides spacepoint measurements of passing charged particles which are later reconstructed into tracks and vertices. The ID is surrounded by an electromagnetic calorimeter (ECAL), which measures the ionization energy liberated by the passage of traversing particles or deposited by electromagnetic showers of photons and electrons. The hadronic calorimeter encircles the ECAL and provides measurements of energy deposits by long-living hadron showers and muons. The largest part of ATLAS by volume is the Muon Spectrometer (MS), which contributes to the event reconstruction information about muons escaping the dense calorimetric system. The ATLAS detector has a complex magnetic field geometry, which comprises four magnet systems: a central solenoid in which the ID resides, an

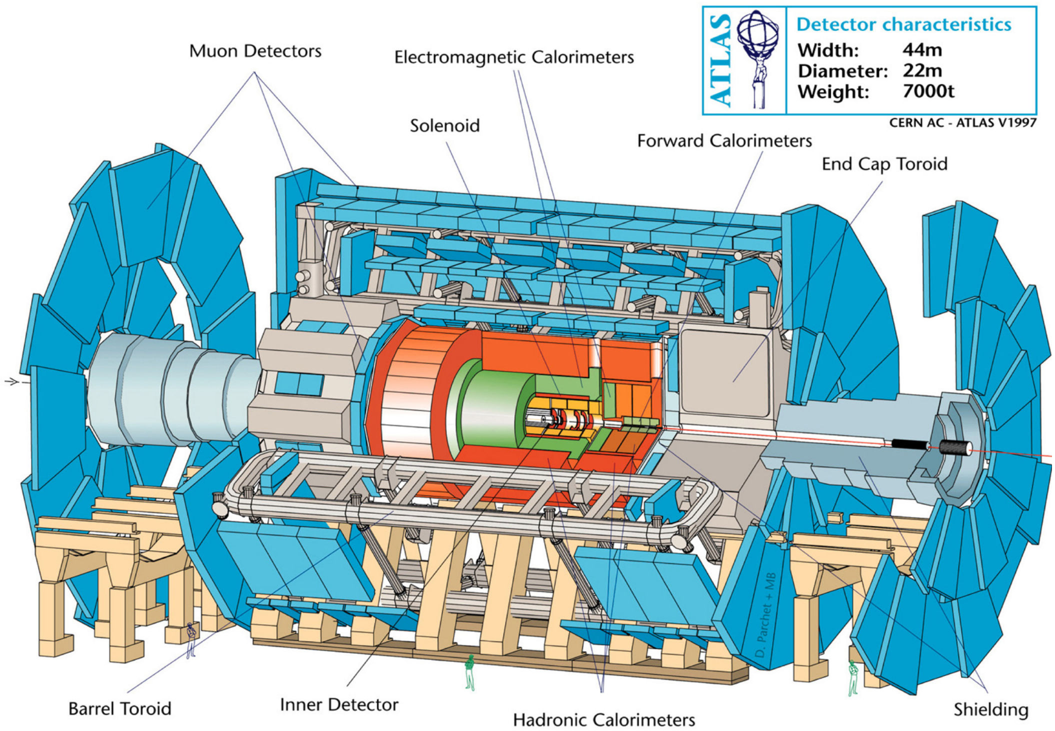

Figure 3.2.: The ATLAS apparatus view with its subdetectors highlighted.

Subdetector	Resolution	η Coverage
Inner Detector	$\sigma_{p_T}/p_T = 0.05\% p_T \oplus 1\%$	$\|\eta\| < 2.5$
LAr calorimeter	$\sigma_E/E = 20\%/\sqrt{(E)} \oplus 10.7\%$	$\|\eta\| < 3.2$
Hadronic barrel and end-cap	$\sigma_E/E = 50\%/\sqrt{(E)} \oplus 13\%$	$\|\eta\| < 3.3$
Hadronic forward	$\sigma_E/E = 100\%/\sqrt{(E)} \oplus 110\%$	$3.1 < \|\eta\| < 4.9$
Muon spectrometer	$\sigma_{p_T}/p_T = 10\%$ at p_T =1 TeV	$\|\eta\| < 2.7$

Table 3.2.: The pseudorapidity coverage and intrinsic resolutions of the ATLAS detector systems [51].

air-core barrel toroid and two end-cap air-core toroids which bend muon trajectories in the MS. The summary of properties of individual detectors can be found in table 3.2.

[1]ATLAS uses a right-handed coordinate system with the beam direction defining the z-axis, the positive x-axis points from the interaction point to the center of the LHC ring and the positive y-axis points upwards. The particle pseudorapidity is defined as $\eta = -\ln(\tan(0.5 \cdot \theta))$ and the transverse momentum $p_T = p \cdot \sin(\theta)$.

3.2.2. Inner Detector

The Inner Detector is a central part of the ATLAS detector and provides measurements of charged particle tracks close to the interaction point. The environment of ID is demanding due to the high particle fluxes which inflict intense radiation damage degradation to its components. At the same time, a very sensitive detector with high granularity and integrated electronics is required to record the same particle flux. It consists of a high-granularity Pixel Detector, the **S**emi**C**onductor strip **T**racker (SCT) and the **T**ransition **R**adiation **T**racker (TRT).

The pseudorapidity coverage of the ID is $|\eta| < 2.5$ for the Pixel detector and the SCT, while the TRT covers the area of $|\eta| < 2$. Charged particle tracks are bent by a 2 T solenoidal field generated by the superconducting central solenoid. In a typical ID track reconstruction, a track has 3 pixel hits, 8 SCT hits and approximately 30 TRT hits. The ID layout is shown in figures 3.3.

ATLAS Pixel Detector

The innermost part of the ID is the Pixel Detector. It consists of a barrel part with 3 cylindrical layers and three endcaps on each side [52]. The innermost layer of the barrel section is located at a radius of 50.5 mm from the beam, the middle layer at a radius of 88.5 mm and the outermost layer is at a radius of 122.5 mm. The total number of detection channels (pixels) is approximately 80 million, covering a total sensitive area of about 1.7 m^2.

The basic functional building unit of the pixel system is a pixel module. There are 1744 such modules in the whole Pixel Detector. Each pixel module consists of a silicon sensor, electronic readout chips and a module controller chip. Each sensor module contains 46080 pixels with dimensions 50 μm $\times$ 400 μm. The sensitive silicon sensor is connected to the readout chip via bump-bonds. On each module, there are 16 readout chips, each servicing an array of 18×160 pixels. In the barrel section, modules are arranged in staves and in sectors in the end-cap disks. All staves and sectors are identical in the mechanical construction. The stave length is 801 mm and the end-cap sections are at the distance of 495 mm, 580 mm and 650 mm, respectively, from the interaction point. The exploded view of a pixel module is shown in figure 3.4.

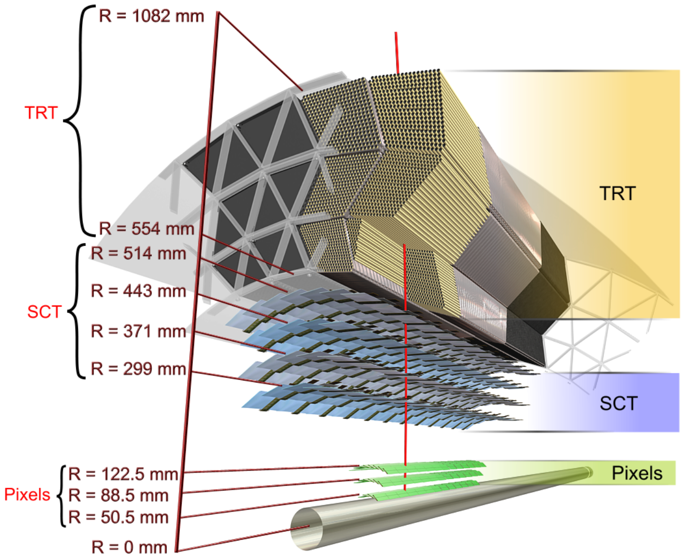

(a) transverse view of the ID barrel section

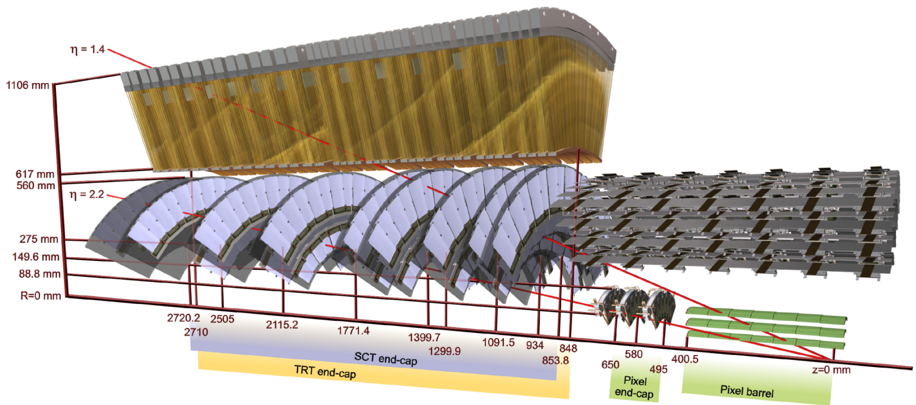

(b) longitudinal view of the ID end-cap section

Figure 3.3.: A diagram illustrating the sensors and structural elements in the Inner Detector. (a) shows the barrel of the ID: the beryllium beam-pipe, three cylindrical silicon pixel layers, four cylindrical layers of barrel silicon micro-strip modules (SCT) and 72 straw layers in the barrel transition radiation tracker (TRT) modules within their support structure. (b) shows the end-cap elements: three silicon-pixel disks, nine disks of the end-cap SCT and forty planes of TRT wheels. The Pixel and SCT barrel layers are also displayed [51].

The detector typically provides three space points per track with resolution of about 10 μm in the $r-\phi$ direction and about 115 μm in the beam axis.

During the LHC LS1 period, a new fourth layer of the Pixel Detector was installed. This Insertable B-Layer will further improve tracking and vertexing performance for the LHC run 2 [53], [54].

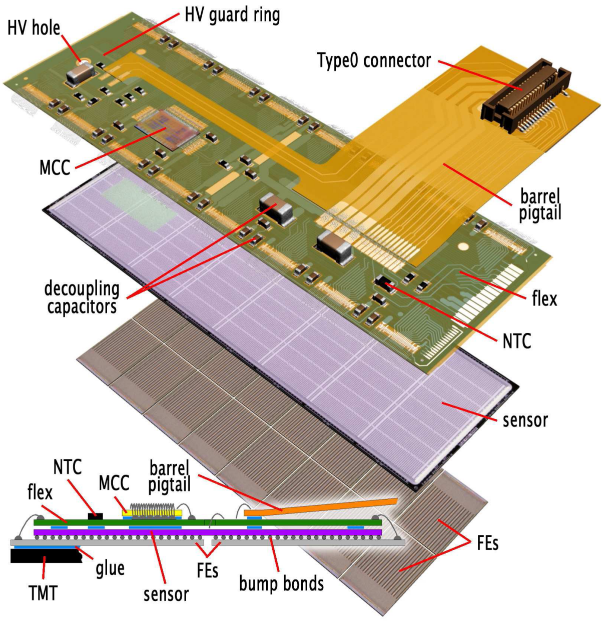

Figure 3.4.: The components of a pixel module. The front-end chips (FEs) are connected via bump-bonds onto a silicon sensor wafer. The supporting flex printed circuit boards also contain a module control chip (MCC), which receives and transmits data from the FE chips. [52]

SCT - SemiConductor Tracker

The Pixel Detector is surrounded by the SCT, which is made of four concentric barrel layers and nine end-caps on each side of the barrel. The total sensitive silicon area of the detector is 61.1 m^2 and it has 6.3 million channels distributed in 4088 modules. The individual barrel layers are at a radial distance of approximately 300, 371, 443 and 514 mm from the beam. The barrel section is approximately 1.6 m long. Each barrel module consists of two silicon strip sensors, skewed with respect to each other by a small angle of 40 mrad between them. Typically, SCT provides 8 hits in sensors and four space points per track. SCT generally provides a space point resolution of about 16 μm in the $r - \phi$ and about 580 μm in the z direction.

TRT - Transition Radiation Tracker

The TRT is the outermost layer of the ID, it extends to a radius of 1082 mm from the interaction region. Its design was driven by the requirement for additional spacepoints for tracking in the pseudorapidity range $|\eta| < 2$ and more importantly the ability of electron and pion separation. TRT is a gaseous detector, it combines the concept of a straw tracker with charged particle transition radiation. It consists of a barrel section and two end-caps. The barrel section has 52 544 detection straws approximately 150 cm long oriented axially (parallel to the beam), providing spacepoint information in the ϕ direction. The straws are split electrically into two. The angular coverage corresponds to the $|\eta| < 0.7$. The end-cap section is made of 319 488 detection straws arranged in wheels radially. It provides resolution of about 130 μm.

3.2.3. Calorimetry system

Calorimeters are widely used in high-energy physics experiments. The basic function of calorimeters is the measurement of the energy and position of incoming particles and particle jets. Calorimetry systems play an important role in the ATLAS physics programme, their main tasks are the measurement of electron and photon energy, identification and measurement of jet energy and direction, and also identification of missing transverse energy.

The ATLAS calorimeter system consists of an electromagnetic calorimeter and a hadronic calorimeter, the schematic view is shown in figure 3.5. While a homogeneous calorimeter usually has better energy resolution as the bulk of the deposited energy can be measured, both calorimeters of the ATLAS are of a sampling design, which can provide more important information about the longitudinal development of the shower.

Liquid argon ECAL

The EM calorimeter is divided into a barrel part $|\eta| < 1.475$ and two end-cap sections $1.375 < |\eta| < 3.2$. It is a lead/liquid-argon (LAr) design with accordion-shaped kapton electrodes and lead radiator plates. The accordion geometry provides complete symmetry in ϕ coordinate and allows avoiding azimuthal cracks. The liquid argon (LAr) was chosen as an active medium because of its radiation hardness and medium speed. Electrons originating from ionization of passing charged particles drift to collecting electrodes and produce electrical signal proportional to the deposited energy. The total thickness of the LAr ECAL is 24 radiation lengths (X_0)[2] in the barrel and more than 26 X_0 in end-caps.

[2] Radiation length is a characteristic amount of matter traversed by particle parameterized by the mean distance over which a high-energy electron loses all but 1/e of its energy by bremsstrahlung.

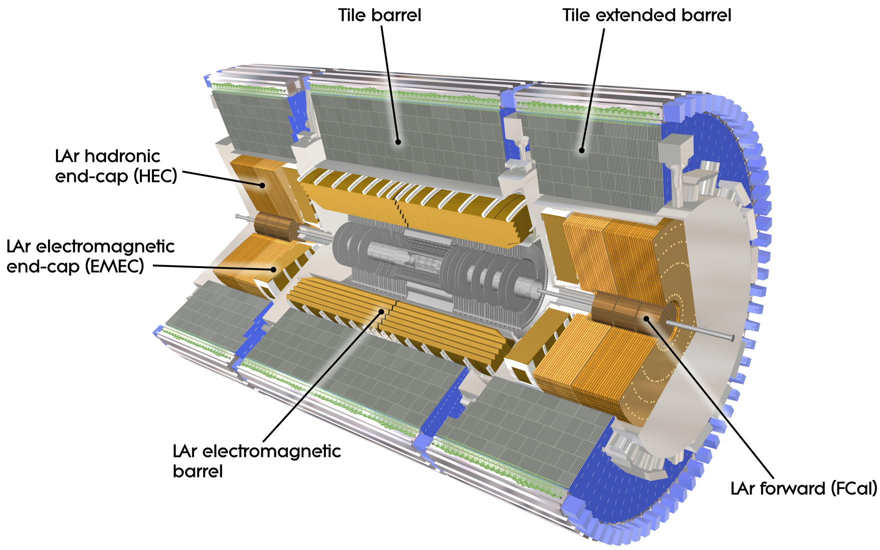

Figure 3.5.: A cut-away view of the ATLAS calorimetry systems. In the barrel section, the inner part is liquid argon electromagnetic sampling calorimeter, the outer part is hadronic scintillating tile calorimeter. The calorimeter endcaps comprise electromagnetic (EMEC) and hadronic (HEC) portions built on a LAr technology sharing a common cryostat. In the forward region around the beam pipe, there is LAr forward calorimeter integrated into the end-cap cryostats. [51]

Hadron calorimetry

The hadronic calorimeter covers the pseudorapidity range of $|\eta| < 4.9$. Two technologies were used in the construction of the calorimeter: The Tile Calorimeter (TileCal) using plastic scintillator as active medium and steel plates as radiator in the $|\eta| < 1.8$ range, and LAr technology similar to the LAr ECAL in the hadronic end-caps which cover the range of $1.7 < |\eta| < 3.1$ and in the forward calorimeter in the range of $3.1 < |\eta| < 4.9$. The calorimeter is divided into a central barrel with 5.8 m length, and two extended barrels. The total thickness is at least 11 hadronic interaction lengths, and it is built to contain a hadronic jet of about 1 TeV.

3.2.4. Muon Spectrometer

The Muon spectrometer (MS) forms the outer layer of the detector and it is designed to detect and reconstruct trajectories of charged particles exiting the barrel and end-cap calorimetry sections. It has sensitive coverage up to $|\eta| < 2.7$ and it provides momentum measurement for particles in a wide range of momenta, ranging from about a few GeV (due to MIP ionization losses in the calorimeter) up to approximately 1 TeV.

While for the low p_T muons, the momentum resolution is dominated by effects such as multiple scattering and fluctuations of the energy loss in the calorimeters, for the large p_T muons the momentum resolution errors are dominated by alignment and spatial resolution of muon chambers due to small sagitta of the muon track. The nominal momentum measurement precision is better than 4 % for 10-200 GeV muons, and about 10% for 1 TeV muons.

The MS consists of a barrel part $|\eta| < 1.05$ and end-cap sections at $1.05 < |\eta| < 2.7$. A system of three air-core superconducting toroids, a barrel toroid and two end-cap toroids provide magnetic field for muon deflection. The barrel toroid is formed by eight coils, the field integral seen across the toroid by muons is ranges from 2 to 4 $\mathrm{T} \cdot \mathrm{m}$. In each end-cap, the magnetic field is generated by eight superconducting coils generating a magnetic field with field integral between 2 and 8 Tm.

The MS is equipped with four types of gaseous detectors, which can be divided into two groups: precision measurement and fast trigger chambers. The actual layout of the MS is shown in figure 3.6.

The MS is equipped with four types of muon chambers [55]:

- RPC - **R**esistive **P**late **C**hambers are gaseous detectors providing a typical space–time resolution of 1 cm $\times$ 1 ns. The basic RPC unit is a narrow gas gap formed by two parallel resistive Bakelite plates, separated by insulating spacers. They collect data for triggering in the barrel section with $|\eta| < 1.05$.
- TGC - **T**hin **G**ap **C**hambers are similar to multi-wire proportional chambers, but with an anode wire pitch greater than the anode–cathode distance. They act as triggering chambers in the endcaps with $1.05 < |\eta| < 2.4$.
- MDT - **M**onitored **D**rift **T**ubes perform the precision coordinate measurement in the bending direction of the air-core toroidal magnet in the $|\eta| < 2$ region.
- CSC - **C**athode **S**trip **C**hambers are basically multiwire proportional chambers with a symmetric cell, in which the spacing between the anode and the cathode is equal to the anode wire pitch. They provide muon spacepoints for the pseudorapidity range $2 < |\eta| < 2.7$.

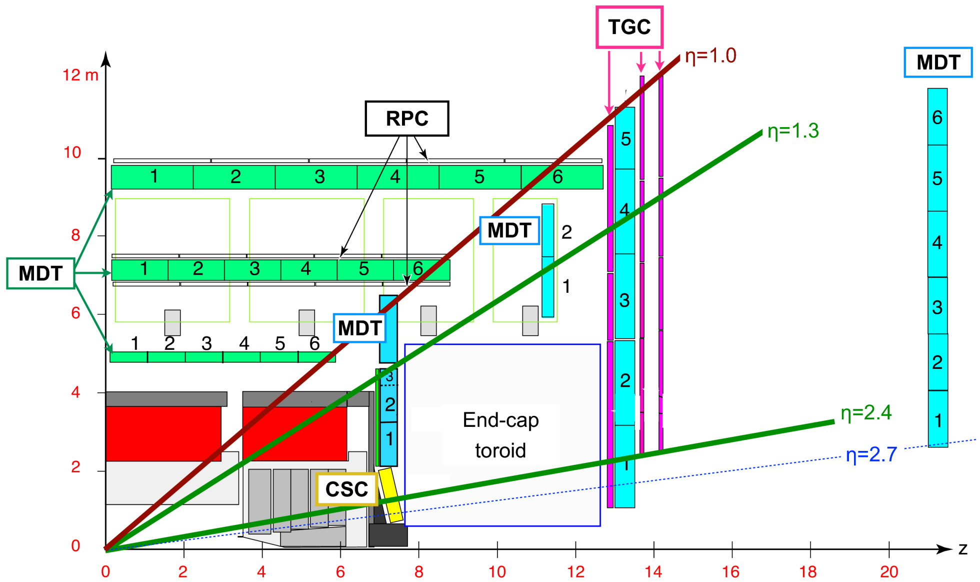

Figure 3.6.: A schematic showing a quarter-section of the muon system in a plane containing the beam axis. The MDT chambers in the barrel are arranged in three concentric cylindrical shells around the beam axis. In the end-cap region, muon chambers form large wheels, perpendicular to the z-axis. In the forward region, CSC is used in the innermost tracking layer. The RPC and TGC chambers are arranged in three layers (called stations) as indicated in the figure. [56]

In the barrel region, the RPCs provide the time and space resolution necessary for triggering. RPCs do not have electrodes made of wires and are therefore easy to construct. This allows an inexpensive coverage of large detector areas. Another advantage of RPCs is short dead time resulting in adequate rate capability and a very good timing resolution of approximately 1.5 ns, which allows muon assignment to individual bunch-crossings. In the end-cap region, the TGC trigger chambers are used for triggering. The high granularity and required hit position resolution is easily achieved by the use of wire electrodes for read-out.

There is about 100 to 190 radiation lengths of material between the interaction point and the MS, its distribution depends on η and consists mostly of calorimeter material.

The muon reconstruction efficiency is affected in two regions of the ATLAS detector, at $\eta \approx 0$, where the MS is only partially equipped with muon chambers due to cabelage and at $1.1 < |\eta| < 1.3$ between the barrel section and the endcaps.

3.2.5. The ATLAS TDAQ system

At the LHC, the bunch crossings occur approximately every 25 ns. It is impossible or extremely costly to record and reconstruct every collision event. Therefore, a trigger mechanism, which selects events interesting from the physics point of view, is implemented. The trigger is a set of hardware and algorithms which selects a particular bunch crossing of interest among others within the trigger budget, i.e. the allowed trigger bandwidth, which is recorded onto storage media. Robustness of the event selection is a necessity, since events that are discarded are lost forever. The ATLAS trigger is implemented as a three-level selection process with the goal of reducing the event rate from the design bunch-crossing rate of 40 MHz to a final average rate of about 400 Hz. The trigger is entwined with the data acquisition system and in common terminology it is called ATLAS TDAQ - trigger and data acquisition system.

For each bunch crossing, the trigger system checks if at least one of hundreds of triggering conditions is satisfied. Triggers are based on identifying combinations of candidate physics objects (signatures) such as leptons ($e^{\pm}$, $\mu^{\pm}$, $\tau^{\pm}$), γ, hadronic objects such as jets (including special triggers for b-quark jets) or the triggers important for analysis presented in this thesis, triggers for special B-physics decay modes. In addition, there are also event-based kinematic trigger signatures for inelastic pp collisions (i.e. minimum bias triggers) and triggers based on global event properties such as missing transverse energy (E^{T}_{miss}) and sum of scalar transverse energy ($\sum E_{\mathrm{T}}$). Trigger signature can be a combination of physics objects and kinematic thresholds. The schematic of the ATLAS TDAQ is shown in figure 3.7.

In ATLAS, the trigger algorithms are organized into so called trigger chains. Each chain is built up from intermediate steps in each trigger level, every step contains algorithms characterized by a physics signature. A trigger chain is often referred to simply as a trigger. The TDAQ trigger system is configured via a trigger menu, which defines complete trigger chains which are running during the data taking. Each chain starts from a level-1 (L1) trigger and specifies a sequence of reconstruction and selection steps for the specific trigger signatures required in the trigger chain. L2 and EF sections in a chain are composed of Feature Extraction (FEX) and Hypothesis (HYPO) algorithms. While the former algorithms create the physics objects (like calorimeter clusters or muon tracks), the latter apply selection criteria to the reconstructed objects (e.g. transverse momentum greater than 6 GeV) and perform trigger decisions.

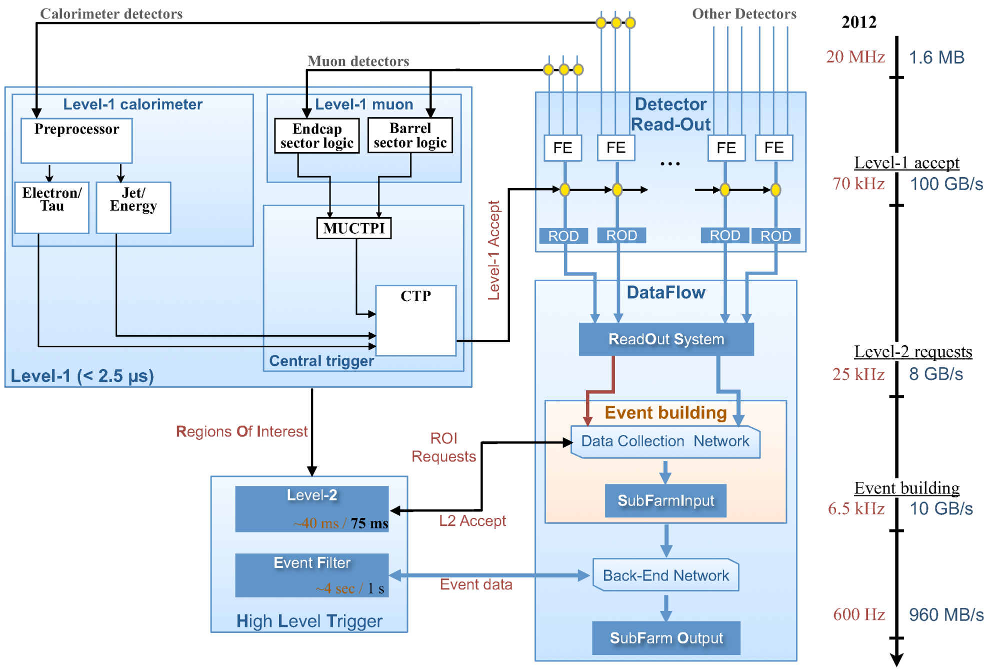

Figure 3.7.: The schematic overview of the Trigger and DAQ system in 2012 (Run 1). The first level uses information from the MS and calorimetry systems to make a decision within 2.5 μs. While the decision is made, data bubble through the pipeline. If the L1 trigger accepts the event, detector data are read-out and continue further to the data acquisition system where an event is built. The L1 trigger produces RoIs, according to which the L2 trigger requests a subset of data from the whole detector. Fast online reconstruction algorithms are run and the L2 trigger decision is made. Events accepted by the L2 have their full data requested by the Event Building (EB), where all fragments are put together and the final decision is made [57].

The first level of the trigger, designated as LVL1, is a hardware based trigger. It utilizes custom electronics with FPGAs and ASICs. The trigger decision is done by a central trigger processor (CTP), which is fed by signals coming from the dedicated hardware in triggering muon chambers (RPCs and TGCs) and calorimeters (LAr ECAL and TileCal). The LVL1 trigger identifies event features such as candidate electrons, photons, jets, muons and missing transverse energy. It must reach a decision within a time window of less than 2.5 μs. The LVL1 trigger decision is based on combinations of objects required in coincidence or veto. For every selected event, the LVL1 trigger also provides the region of interest (RoI) information, an area in η and ϕ section of the detector where the object that fired the LVL1 trigger occurred.

The second and third level triggers are referred to commonly as high level trigger (HLT). They are based on PC farms running Linux operating system and a dedicated triggering software. The second level trigger, L2, receives data at full granularity within the RoI provided by the LVL1 and combines information from all detectors. The reconstruction is performed only within RoI to minimize the computing load. Using RoIs from LVL1 reduces the volume of data requested to a few percent of a full event. When an event passes L2 trigger, it is forwarded to a third trigger level, the event filter (EF). The EF refines selection of the L2 classification, performing full online event reconstruction. At this level, more detailed alignment and calibration data are available. The trigger system makes extensive use of caching of reconstructed objects, it allows features extracted in one chain to be reused in another similar chain, thus minimizing both the data access and processing time of the trigger system. The description and design of the ATLAS HLT trigger can be found in [58].

Reconstructed data for physics analyses are delivered in so-called streams. A trigger stream consists of events that were triggered by related signatures recorded to the same data-set. Streams are designed in a way that the overlap between them is minimal. The EF stream recording rates per month in 2012 are shown in figure 3.8.

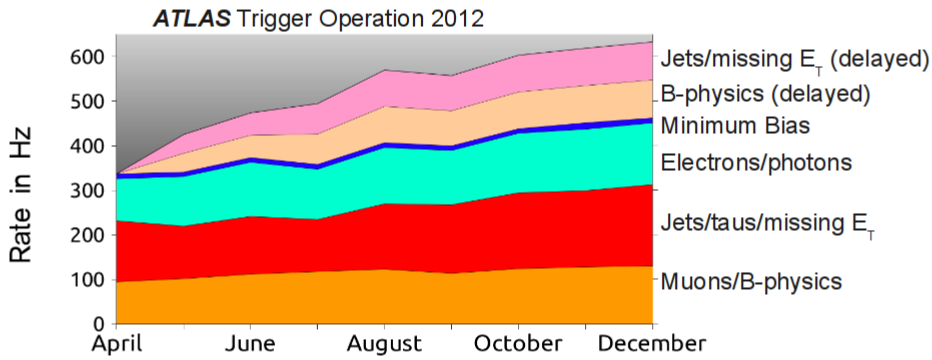

Figure 3.8.: Event Filter stream recording rates per month, averaged over the periods for which the LHC declared stable beams. Special run periods such as Van der Meer (VdM) scans or ALFA runs have been left out. Optimization of DAQ streams allowed for the increase of the total trigger rate recorded onto a disk. [59]

In order to keep the recording bandwidth below resource limits, trigger rates must be controlled. That can be achieved by several different techniques: changing physics objects thresholds, applying different sets of selection cuts or most commonly by prescaling. Triggers, especially for low p_T objects, can be prescaled by a factor of N to reduce the trigger rate to an acceptable level, which effectively translates to recording one random event of N triggered events. During a data-taking run, the trigger rate falls with a decreasing beam instantaneous luminosity; therefore, dynamic prescales are applied to reduce the trigger rate to a similar level as luminosity falls. The trigger settings, including prescales, are kept constant during a lumiblock (short for luminosity block), a time period about 1 minute long where the TDAQ settings do not change and luminosity is considered constant.

Triggers can also be divided according to prescales into three groups:

- Unprescaled triggers, which usually have large thresholds so their final trigger rate is small. They are kept constant over a long data-taking period. These triggers are highly desirable for analysis.
- Prescaled triggers are commonly used in physics analysis, but they are prescaled down at high luminosity to keep recording level below resource limits.
- Supporting triggers, used mainly for detector monitoring and calibration, validation of other triggers and to collect unbiased background samples. They are highly prescaled and are allowed a small fixed output rate.

3.2.6. The ATLAS muon trigger

The muon trigger is a subset of TDAQ which identifies muons in collision. Its task is to select interesting events with good efficiency and minimum bias. Each level of muon trigger refines the decision made by the previous one and, where required, applies additional selection criteria. The time window for decision-making process increases for each trigger level, which allows the use of an increasing amount of information and algorithmic complexity.

ATLAS Level-1 trigger

The Level-1 (LVL1) muon trigger system is a hardware-based system which processes input data from fast muon trigger detectors [60]. Its main objective is to select muon candidates and identify the bunch crossing in which they were produced. The RPC and TGC systems provide a very rough measurements of muon candidate p_T, η, and ϕ coordinates. In order to form coincidences, hits are required to be located within the so-called parameterized geometrical muon roads. A road represents an envelope of all muon trajectories originating in the beam interaction point with a p_T above a defined threshold.

The LVL1 muon trigger selects active RoIs in the event using RPCs in the barrel and TGCs in the endcaps. As input, the muon trigger receives the pattern of hit strips or wire groups in the muon Trigger chambers. The elementary working principle of the LVL1 muon trigger algorithm is to require a spatial and temporal coincidence of hits in the different trigger stations inside the muon roads [60].

There is a total of more than $8 \cdot 10^5$ input signals to the muon trigger system alone. The LVL1 triggers generated by hits in the RPCs or TGCs require a coincidence of hits in the three stations for the $p_T > 10$ GeV thresholds, and a coincidence of hits at least in two of the three stations for the lower p_T thresholds [56]. The illustration of trigger stations coincidences is shown in figure 3.9.

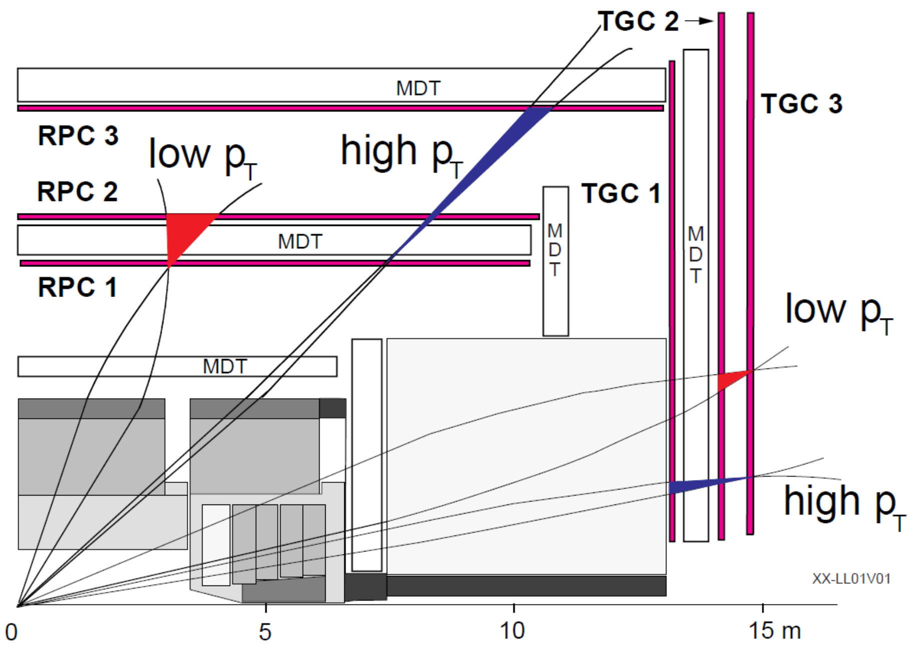

Figure 3.9.: Longitudinal view of the barrel and end-cap triggering systems. Muons are identified at LVL1 by spatial and temporal coincidence of hits in the RPCs or TGCs pointing to the beam interaction region. The chambers marked as RPC2 and TGC3 are the reference pivot planes for barrel and end-cap sections [60].

The RoI has typical size of $\Delta\phi \times \Delta\eta \approx 0.1 \times 0.1$ in the RPCs and $\Delta\phi \times \Delta\eta \approx 0.03 \times 0.03$ in TGCs, giving a total of approximately 7200 trigger cells. Higher trigger levels then provide verification and more precise reconstruction [61].

ATLAS Level-2 trigger

The Level-2 (L2) trigger operates only in the detector region immediately around the RoI. It loads full granularity data from the Read-Out Buffers related to the RoI, prepares them for processing and distinct fast algorithms are engaged. The RoI provided by the LVL1 enables Level-2 trigger to select the region of the muon detector in which the interesting features reside, thus reducing the amount of data to be transferred and processed.

The L2 trigger performs event reconstruction within the muon RoI and validates the LVL1 decision. The L2 trigger has at its disposal the complete information from the MS including MDT and CSC chambers. It must decide within 40 ms whether to keep or discard an event. The L2 reconstruction algorithms are designed to meet the stringent timing requirements for event processing. Muon FEX algorithms usually reconstruct muon trajectory using the combined information from the ID and MS; therefore, corresponding ID and MS track reconstruction algorithms are employed.

There are several strategies and corresponding pattern recognition algorithms which reconstruct ID tracks at the L2 trigger [62]. First, the clusters are formed from adjoining hits in the Pixel detector and SCT. Pixel and SCT clusters are combined with geometrical information from ATLAS geometry database to provide three dimensional hit information, called space-points. Clusters and space-points provide input to the HLT pattern recognition algorithms. The three most important algorithms are:

- *IDScan* algorithm is based on the space point histogramming, it determines the z position of the interaction point and groups space points in the RoI into (η, ϕ) bins. Then it performs a combinatorial tracking only inside of spacepoint groups that point to the determined primary vertex position.

- *SiTrack* algorithm is based on a combinatorial approach. Tracks are formed from spacepoints within a set of roads that correspond to the inside-out combination of spacepoints in the ID. Knowledge of the z position of interaction vertex is not needed.

- *L2Star* (**L2** **S**ilicon Tr**A**ck **R**econstruction) is a new framework for trigger tracking at L2. This framework was designed to simplify software maintenance and facilitates an environment for the development of new tracking strategies while at the same time avoiding duplication of code. It consists of a module which can be configured to apply different tracking strategies. Strategy A is projection based, similar to the *IDScan*, Strategy B is combinatorial, similar to the *SiTrack*. *L2Star* allows combination of strategies. It was deployed during the 2012 data taking.

The *L2Star* framework represents an effort to combine both the *IDScan* and *SiTrack* algorithms in a common coding structure, allowing their respective track pattern recognition techniques to be used in a modular format [62]. This enables easy optimization of the algorithms to specific physics signatures. In 2012 data taking, the separate implementations of *IDScan* and *SiTrack* were replaced with their *L2Star* equivalents, labeled Strategy A and Strategy B, respectively. These algorithms employ the same code structure, but with some optimization of the ingredient parameters. These were adjusted to improve the pattern recognition performance in the high pileup environment created by the LHC running.

Concerning the muon reconstruction at L2, a MS track is constructed by adding the data from the MDT and CSC chambers to get a more precise estimate of the track parameters, leading to the L2 stand-alone-muon [63]. There are four approaches of muon reconstruction in L2:

- $\mu Fast$ aims at confirming or discarding muon candidates provided by Level-1. It selects hits from MDT stations within a road where the Level-1 muon trigger detectors were fired. In each station, a local linear fit is performed to obtain the intersection of the muon trajectory with the station itself.

- $\mu Comb$ combines the $\mu Fast$ stand-alone MS tracks with information coming from other detectors, such as the Inner Detector (ID). It matches MS and ID trajectories by means of spatial windows determined analytically with a very fast procedure based on optimized LUTs.

- $\mu Tile$ is designed for gaining efficiency on very low-p_T muons. This is useful for triggering of low-p_T B-physics events, where muons are triggered by RPCs or TGCs with relatively low probability, since their p_T is so low that track segments are produced only in the innermost layer of the MS.

- μIso selects high momentum isolated muons, it also uses information from the LAr and Tile calorimeter systems to compute the isolation.

ATLAS EF trigger

The task of the EF trigger is to perform a detailed muon reconstruction and confirm or discard muon candidates found at Level-2. The EF computing farm runs much more sophisticated algorithms which have access to the complete event information. The reconstruction at the EF is less time constrained ($\approx$ 4 seconds per event) and uses software components from the offline reconstruction which enjoy the modularity and flexibility of the offline tracking framework. It shares the tools and services provided by the offline software and provides access to most of the offline tracking strategies and algorithms.

Muons in the event-filter are found by two different procedures. The first focuses on RoIs defined by the Level-1 and Level-2 steps described above and is referred to as the RoI-based method. The second procedure searches the full detector without using the information from the previous levels and is referred to as the full-scan method. There are several online muon reconstruction algorithms available [58]:

- *TrigMuEF* starts from the MS and extrapolates track back to the IP. It consists of a chain of four sequential FEX algorithms and the corresponding HYPO algorithms to produce the final trigger decision: *SegmentFinder*, *TrackBuilder*, *Extrapolator* and *Combiner*. Muon track segments are made first, starting from MDT precision hits, then tracks are built from segments inside the MS, adding information from the other muon detectors taking into account the complexity of the magnetic field, the energy loss in the calorimeters and the effect of the multiple scattering through all crossed materials. In the last step, extrapolated MS tracks are combined with matching ID tracks by the means of a global track refit of all the spacepoints found in both MS and ID systems.

- *TrigMuGirl* employs a different strategy. It starts from the ID tracks and performs muon identification outwards starting from candidates provided by EF Inner Detector algorithms, inside the muon Level-2 RoI. Tracks are subsequently extrapolated towards MS chambers, looking for hits around the ID track direction, making segments from hits and improving extrapolation using segments.

The whole muon chain demonstrates excellent performance, as is shown in figure 3.10.

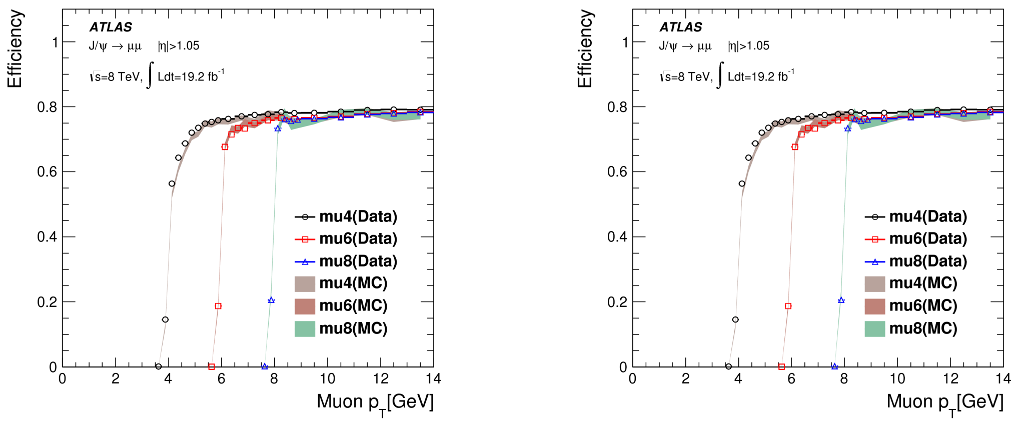

(a) MS barrel region **(b)** MS end-cap region

Figure 3.10.: Efficiency of low p_T single muon triggers, mu4, mu6, mu8, measured as a function of the probe muon p_T, separately shown for the barrel region and the end-cap region. For a better view, the error bars for MC indicate the statistical uncertainties only, while those for data indicate both the statistical and systematic uncertainties. Image taken from [56].

The B-physics triggers

B-physics triggers are low-p_T dimuon triggers with imposed additional mass cuts to select specific final state signatures ($J/\psi \rightarrow \mu\mu$, $\Upsilon \rightarrow \mu\mu$ and $B \rightarrow \mu\mu X$). The advantage of triggering on di-muons is a clean physical signature, while the drawback is a relatively low branching ratio (≈ 0.0066) of a B hadron decaying to J/ψ, which is required to decay into a pair of muons.

For the triggering of di-muon channels, three approaches have been devised, each finding its area of usefulness at a different instantaneous luminosity levels:

- Topological triggers, which require two L1 muon RoIs. At Level-2, $\mu Fast$ algorithm reconstructs a muon in the MS and $L2StarB$ algorithm reconstructs ID tracks. From these collections, $\mu Comb$ algorithm creates global muon tracks. If there are more than two muons, di-muon combinations are formed and they are passed onto the fast vertex fitter which performs a fit of muon tracks and returns a vertex. The vertex parameters are subject to scrutiny, and if the vertex quality is good enough and the di-muon invariant mass is in the allowed range, event is passed to EF. The EF then repeats the L2 procedures with tools and algorithms developed for offline analysis. An example of such trigger is EF_2mu4T_Jpsimumu_L2StarB, used in the analysis presented in following chapter.

- *TrigDiMuon* triggers are seeded by a single L1 muon RoI. Search is performed at higher trigger levels for a second muon starting from ID tracks. Invariant mass calculation of a triggered muon and oppositely-charged track pair is performed. If this mass is within a certain mass window, the ID track is extrapolated to the MS and the algorithm searches for any hits in the MS in the vicinity of extrapolated track. If hit criteria are satisfied and the second track is a muon candidate, vertex fit of two muons is performed in a similar fashion as the topological trigger case. They were developed primarily for the LHC low-luminosity running for the 2010 detector commissioning period.
- Muon + track trigger signature was developed primarily for selection of events for triggering and reconstruction efficiency studies. It is similar to the *TrigDiMuon* signature, but it does not search for any hits in the MS. It features a tight invariant mass cut to limit trigger rate. This trigger was used as a primary trigger for J/ψ and Υ events in the early data-taking periods of 2010.

The *TrigDiMuon* and muon + track triggers can be operated in a so-called FullScan (FS) mode, where the triggers are using tracking within the entire Inner Detector rather than just in the region of interest.

In the data recorded in the 2011 and 2012 data taking periods, topological B-physics triggers were employed by most analyses. For di-muon signature, there is a set of invariant mass cuts for each reconstructed di-muon vertex:

- 2.5 - 4.3 GeV designated for J/ψ triggering
- 4.0 - 8.5 GeV devoted to B decays such as $B_s \to \mu\mu$
- 8 - 12 GeV trigger for $\Upsilon(1S, 2S, 3S)$ events
- 1.5 to 14 MeV DiMu triggers which covers the whole B-physics region.

The trigger di-muon invariant mass windows are shown in figure 3.11. In the trigger chain EF_2mu4T_Jpsimumu_L2StarB utilized in this work, the triggering chain functions as follows: At LVL1, two muon RoIs above 4 GeV transverse momentum threshold are required. At L2, the muons are confirmed by the $\mu Fast$ algorithm and then by $\mu Comb$ in combination with the ID track reconstructed by the B variant of the $L2Star$ algorithm.

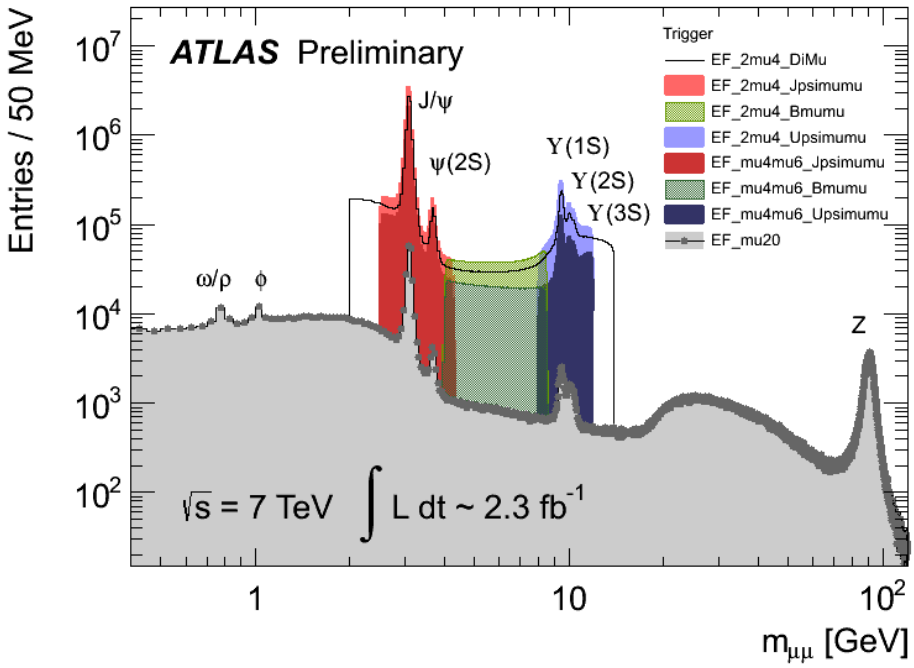

Figure 3.11.: The invariant mass of di-muons in the recorded data. Different colors denote different mass cuts on di-muon trigger. Grey represents prescaled EF_mu20 trigger, where a single muon is required at Level 1, confirmed at the HLT, passing a threshold of 20 GeV. EF_2mu4 denotes two muon triggers at Level 1, confirmed at the HLT, with both objects passing a threshold of 4 GeV. EF_mu4mu6 denotes two muon triggers at Level 1, confirmed at the high level trigger, with one object passing a threshold of 4 and the other 6 GeV. Jpsimumu, Bmumu, Upsimumu and DiMu denote coarse invariant mass windows in the regions of the J/ψ (2.5-4.3 GeV), B (4-8.5 GeV) and Υ (8-12 GeV) and the combined range of all three (1.5-14GeV) respectively, as calculated using the trigger objects [64].

The 2 muons are then used as an input by $BMuMuFex$, where a vertex fit is performed for opposite sign muons and a J/ψ mass cut and a cut on vertex χ^2 is made.

3.2.7. The physics analysis software

The ATLAS offline software is a part of the Athena package. The Athena software framework is based on Gaudi [65], a project originally developed by LHCb.

3.2.8. Analysis data flow overview

Collison data are collected in runs (usually the entire LHC fill) and they are subdivided into lumiblocks approximately 1 minute long. In 2012, the average trigger rate during *pp* collisions in stable beam conditions was approximately 550 Hz. This includes all physics streams which, with an average compressed RAW event size of 0.8 MB/event, gave an average 440 MB/s streaming rate of RAW events. [66]

After recording, the ATLAS offline data reconstruction is performed at Tier-0 center located at CERN [67]. The RAW data are processed in two steps within one job, producing first the ESDs and then the derived AODs and DESDs in the second step. The ESD is a transient format, it is implemented in a circular buffer. The RAW data and output from reconstruction are exported to the ATLAS Grid storage Tier-1 centers. Data events are reconstructed with the Athena framework and then they are stored in the AOD format. The AOD does not contain low-level information about hits and spacepoints, but it has a variety of high-level physics objects such as the trigger information, reconstructed tracks, photons, electrons, muons and jets. The produced AODs are then skimmed, slimmed and/or thinned into the Derived Physics Data format used in the physics analyses. The flow is visualized in figure 3.12.

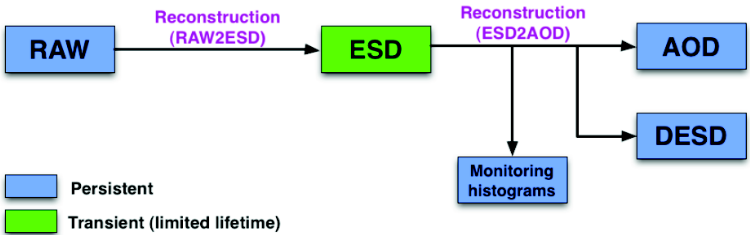

Figure 3.12.: The objects reconstructed from the RAW data are temporarily stored in the ESD format. The physics information for user analysis is stored in the AOD file format. The DESDs are designated for detector performance studies. Figure from [66].

The ATLAS production of the Monte Carlo samples starts with the generation of hard-process collisions using the Monte Carlo generator programs producing EVNT files. In some cases, pre-generated inputs for the processes are produced off-Grid and registered on a Grid storage for MC event generation and EVNT production. The EVNT files are then processed in the detector simulation step, producing HITS files. The modeling of pile-up is added in the next processing stage and the detector response (digitization) is simulated at the same time, producing RDO files. As a separate step, the trigger response simulation is performed again producing RDO files with the simulated trigger

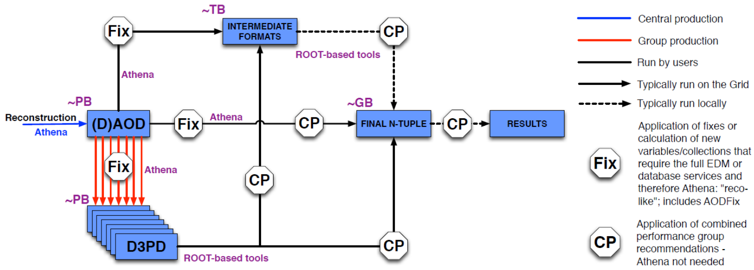

Figure 3.13.: The ATLAS Run 1 Analysis Model from the AOD onwards. Users either analysed the (D)AOD directly in Athena or converted the (D)AOD into a ROOT NTUP format or D3PD. Very often these PB size formats were reduced to intermediate formats of an order of TB in size by applying simple selection criteria and/or removing per-event information. Figure from [68].

information added. The rest of the reconstruction chain is the same as the prompt data reconstruction.

The data flow of a typical user analysis is shown in figure 3.13.

Event data structure records

Each run and each stream produce one dataset (logically connected files). The most important dataset categories are presented in table 3.3.

3.2.9. Athena - analysis and simulation software package

Athena is a common framework for detector performance and physics studies. It is based on C++ and Python and it is a concrete realization of a component-based architecture descended from Gaudi, which is designed for a wide range of physics data-processing applications. Apart from specialized data types, procedures and functions, Athena is a central software repository for all physics algorithms. The Athena framework is managed by using the Configuration Management Tool (CMT) [69].

The Athena framework ensures that the algorithms are run in the correct order, and it offers common services such as message logging, access to data types stored on memory media, and filling of histograms and production of ntuples in cooperation with ROOT [70]. The algorithm output collections are written to a common place in memory,

Name	Description	Typical event size
RAW	Raw data contain all information from the detector in a compressed byte-stream format. It is a persistent representation of the complete event data produced by the ATLAS online detector machinery.	1 MB
ESD	Event Summary Data are an object oriented representation. Besides hits, this dataset contains also the detailed output of the detector physics object reconstruction. It is produced from the RAW data. It is a transient storage for data, which are produced in a circular buffer-like fashion.	2 MB
AOD	Analysis Object Data: C++ object representation, contains physics objects but no detector hits. In principle, it contains sufficient information for common physics analyses. Separate dedicated streams of AODs are made to suit different needs of the physics community.	200
DAOD	Further derived formats: C++ object representation of data, where reduction is used to select targeted events and store only the necessary information.	100 kB
DPD	Derived Physics Data, usually Skims, Slims and Thins of AOD. They are made in physics groups for user analysis. They are written in ROOT N-tuple format.	10 kB
EVNT	Event Data: C++ object representation (HepMC), contains the truth event information as produced by Monte Carlo generators such as Pythia, Herwig++, MC@NLO.	40 kb
HITS	Hits data from full or fast detector simulation: C++ object representation contains simulated energy deposits in active detector volumes and related particle information.	1.1 MB
RDO	Raw Data Object: a C++ object representation of the byte-stream information (i.e. RAW data format), used predominantly in simulation.	2.2 MB

Table 3.3.: Different file formats produced during event reconstruction.

called the 'transient event store', from where they can be retrieved and processed further or they can be written to a disk, using the POOL persistency scheme.

The complexity of the physics that is taking place at the LHC collisions and the diversity of the ATLAS subdetectors require a detailed description of the Monte Carlo event generation and of the detector response simulation.

In general, the production of simulated events comprises several steps:

- Event generation is modeling of complex physics processes that occur at the LHC proton collisions. Event simulation produces hundreds of particles per event at LHC energies. A more detailed discussion about event generators takes place in section 2.1.

- Detector simulation is a process, which models the physical interaction of particles, which were generated in the previous step, with the detector subsystems. In ATLAS, this is performed by the Geant4 toolkit [71], which is steered by the G4ATLAS application [72]. GEANT4 performs particle transport through the magnetic field and simulates the interactions with the detector material. It allows detailed simulation of multiple scattering, ionization energy loss, and photon conversions. It also simulates the decay of unstable particles such as $K^{\pm}$ and $\pi^{\pm}$ which make up the bulk of the decays-in-flight background in the analysis presented in this thesis.

- Digitization is modeling of response of detector electronics. It includes simulating the response of the detector to the energy deposits simulated in the previous step.

- Event reconstruction is the last step of processing. Starting from the hits produced in the detector, specialized algorithms are run to reconstruct the event. Besides other physics objects, they include algorithms for hit spacepoint formation, pattern recognition, track fitting, vertex finding, energy measurement and muon reconstruction.

3.2.10. Offline muon reconstruction

The analysis presented in this thesis concerns muonic final states; therefore, this chapter will concentrate on muon reconstruction. For the detailed description of the tracking event data model in the ATLAS detector, see [73]. The ATLAS detector reconstructs muons with information collected by the ID, MS and to a lower extent calorimetry system.

The muon reconstruction in the ATLAS detector represents a challenge because of reasons of high background level present in the ATLAS experimental cavern, which yields high single MS tube occupancy which can create fake tracks from combinatorial hit associations. Moreover, the MS magnetic system provides inhomogeneous magnetic field which forbids any simple analytical muon trajectory description. There are also four different types of muon chambers with their specifics arranged in a non-trivial geometry. There are large distances between muon measuring stations which cause substantial extrapolation uncertainties. Furthermore, the physical separation between precision chambers and trigger chambers supplying the second coordinate prevents the use of a full, three-dimensional information.

The offline track reconstruction is described in full in [74]. The helical trajectories of tracks are parameterized uniquely by Billoir track parameters in a vector $A = (d_0, z_0, \phi, \theta, q/p)$, where d_0 (z_0) is defined as a transverse (longitudinal) distance of track perigee to the primary vertex. A perigee is the distance of the closest approach of track to the primary vertex. The ϕ_0 is the azimuthal angle of the track at perigee, and θ is its polar angle. The ratio of q/p is the particle charge multiplied by the inverse of its momentum. The track parameters are graphically illustrated in figure 3.14.

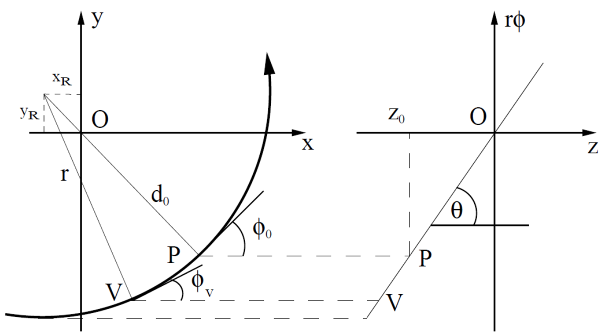

Figure 3.14.: Schematic view of the ATLAS track Perigee Parameters [74].

In ATLAS, there are four strategies for offline muon reconstruction and corresponding muon categories:

- Combined muons, where the track reconstruction is performed independently in the ID and the MS. Final track is formed by combination of those two tracks. This is the most important category of muons and it is utilized solely in this analysis since the muons are measured with the highest precision and are the purest with respect to other categories.

- Standalone muons are muons that are reconstructed solely in the MS. In other analyses, they are mainly used to extend the range of measurements beyond the ID $|\eta| < 2.5$ limit. The standalone muon track is extrapolated back to the interaction point, while taking into account the ionization energy losses in the calorimetry systems. The muon track parameters are then calculated at the muon closest point of approach to the beam.

- Segment-tagged muons are muons, where the ID track is extrapolated to the MS and it is associated to at least one local track segment in the precision MDT or CSC chambers.

- Calorimeter-tagged muons are muons with an identified ID track that is associated to the cluster of deposited energy in the calorimeter, that is compatible with MIP energy loss hypothesis. This category has the lowest purity of muons, but its advantage is that it recovers muon acceptance in the uninstrumented regions of the MS around $|\eta| < 0.1$.

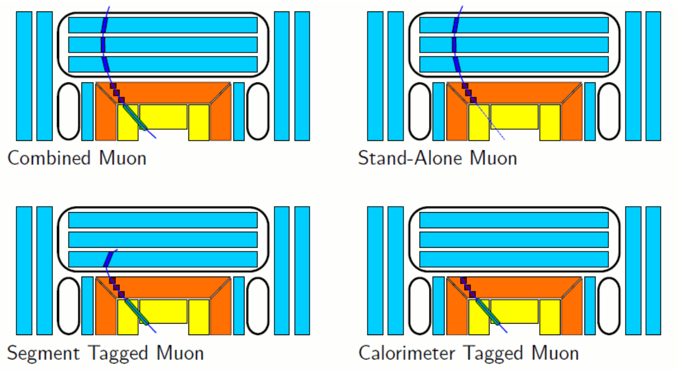

Figure 3.15.: Reconstructed muon categories. Combined muons are completely reconstructed in the MS and in the ID, while stand-alone muons are reconstructed only in the MS and no match for the ID track is found. Both segment and calo-tagged muons are utilized to increase the acceptance in detector areas with limited muon chamber coverage. While the former matches the ID track to an incomplete track segment in the MS, the latter matches the ID track to a localized energy deposit in the calorimeter. [75]

The muon categories are shown in figure 3.15. and are reconstructed by three muon reconstruction chains.

In the 2012 data taking period, the muon reconstruction algorithms are divided in three chains STACO, MUID and MUONS (also termed Chain 3). The algorithms in these chains are applied seperately to reconstruct muon candidates in collision events and produce separate muon candidate collections. Since the same muons are reconstructed by these chains, essential overlap in muon candidates within the chains must be taken care of during the user data analysis. This is usually done by selecting one of these chains as a sole source for reconstructed muons.

Besides philosophical and technical differences, the major difference between the STACO and MUID lies in the process of combining measurements from the MS and the ID. The STACO attempts to statistically combine the two independent measurements from the ID track and the MS track, while the MUID performs a global fit of all the hits associated with the tracks in both detectors, taking into account muon ionization losses in the calorimeter.

STACO stands for **STA**tistical **CO**mbination of MS and ID tracks [76]. It performs a calculation of χ^2 for all combinations of tracks. It accepts only the combined tracks if χ^2 is below the preset threshold value. The offline MS track is reconstructed using the $MuonBoy$ algorithm. It processes the MS hit information in the regions of activity, in areas indicated by the trigger chambers. It searches for hits and produces track segments and tracks, which are then extrapolated to the beam interaction point. During this phase, muon ionization momentum losses are corrected for using an energy loss parameterization. In order to combine the ID and MS tracks, the STACO suite performs a statistical combination of these two independent track measurements using the parameters of the reconstructed tracks and their covariance matrices. For the purpose of improving low-p_T muon reconstruction efficiency, the STACO suite features the $MuTag$ algorithm, which associates the ID track to the $MuonBoy$ track segments not yet associated with a combined track. If no matching ID track is found, the $MuonBoy$ muon is considered to be standalone.

The MUID chain [77] consists of the MOORE and $MuID$ and $MuGirl$ algorithms. MOORE (**M**uon **O**bject **O**riented **RE**construction) performs offline track reconstruction in the MS. It uses hit information in the MS to produce standalone segments and tracks. The track fit procedure is based on the track fitting package, developed for the ID. The package MuID can extrapolate the MOORE tracks back to the interaction point and determines the muon track parameters at the perigee. This package also allows reconstruction of combined muons by performing a global fit of a MS track combined with an ID track. It does a global fit by first calculating a χ^2 fit of the MS and compatible ID track parameter differences and their covariances. Then, a combined fit is performed for all MS-ID track matches below set χ^2 threshold. In case of a successful combined fit, these refitted tracks are kept as combined muons. The MUID chain also contains its tagged-muon algorithm, $MuGirl$. Similarly as $MuTag$ in the STACO chain, it starts searching for muon track segments and tracks in the MS at the coordinates defined by the ID track. If a full track refit is possible, a combined muon is made. If this is not the case, a tagged muon is made.

The use of two independent offline muon reconstruction algorithms STACO and MUID brought robustness and redundancy in the ATLAS commissioning phase during Run 1. Both chains have demonstrated their excellent capabilities in physics analyses with muons. While the STACO and MUID algorithms can be considered mature and validated, their maintenance and presence of both muon collections in data has been causing redundancy of effort and confusion within the physics analysis communities who had been forced to decide which of the two reconstruction chains is to be utilized. Therefore, a new unified muon reconstruction algorithm Chain 3 has been developed [78] to incorporate the best features of the two. It has been used first in the reconstruction of 2012 data, and it is anticipated that only this third muon chain will be employed for future data taking in 2015 and beyond. It is in fact this third chain which was used as a source of reconstructed muons in the analysis presented here.

The comparison of reconstruction efficiencies of the muon chains is shown in figure 3.16 as a function of muon transverse momentum, and in figure 3.17 as a function of muon pseudorapidity. The performance of the muon reconstruction chains in 2011 and 2012 data taking periods is presented in full in [75].

J/ψ reconstruction

In Athena package, a specialized B-physics software package has been developed, covering all the aspects of various decay topologies and constraints of B-physics. The package has a modular structure, which contains a set of core algorithms for specialized studies and a common tools for building the decay chain. These tools are implemented in separate classes - for vertexing interfaces, flavor tagging, Monte Carlo truth handling [79]. Within this framework, the J/ψ reconstruction is performed using $JPsiFinder$ algorithm. It was developed specifically to suit the needs of ATLAS B-physics community for reconstruction of di-muon vertices. From all the muon combinations in an event, it performs a vertex fit on a pair of muons and if the di-muon pair satisfies the pre-set criteria, it is stored as a di-muon candidate. The selection criteria include cut on a common vertex χ^2, invariant mass, input muon track quality or the combination of input muon charges. Overall, the ATLAS capability and precision of reconstruction of di-muon pairs is demonstrated in figure 3.18.

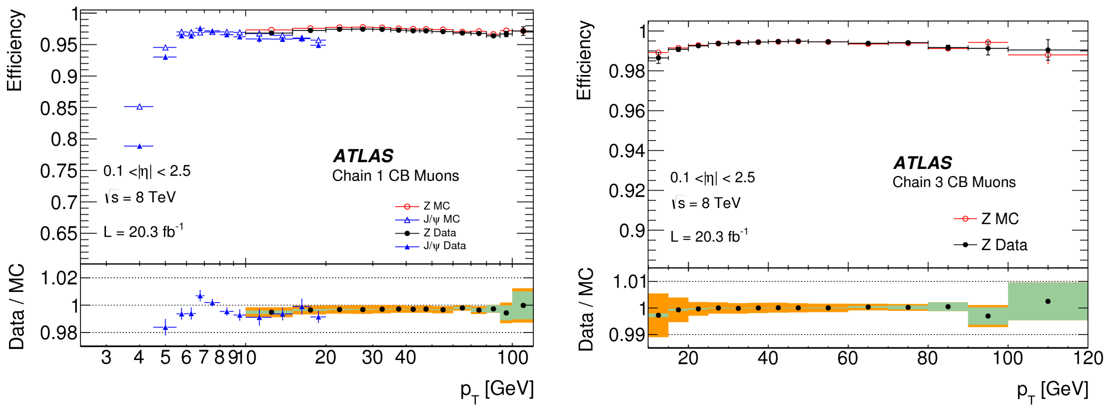

(a) barrel region **(b)** endcap region

Figure 3.16.: Left: Reconstruction efficiency for muons reconstructed in Chain 1 (STACO) as a function of the p_T of the muon within the range of $0.1 < |\eta| < 2.5$. It shows the results obtained with $Z \to \mu\mu$ and $J/\psi \to \mu\mu$ events. The error bars on the efficiencies indicate the statistical uncertainty for $Z \to \mu\mu$ and include also the fit model uncertainty for $J/\psi \to \mu\mu$. The panel at the bottom shows the ratio between the measured and MC predicted efficiencies. The green areas show the pure statistical uncertainty, while the orange areas also include systematic uncertainties. Right: Analogous plot for Chain 3 (MUONS) derived from $Z \to \mu\mu$ events. [75]

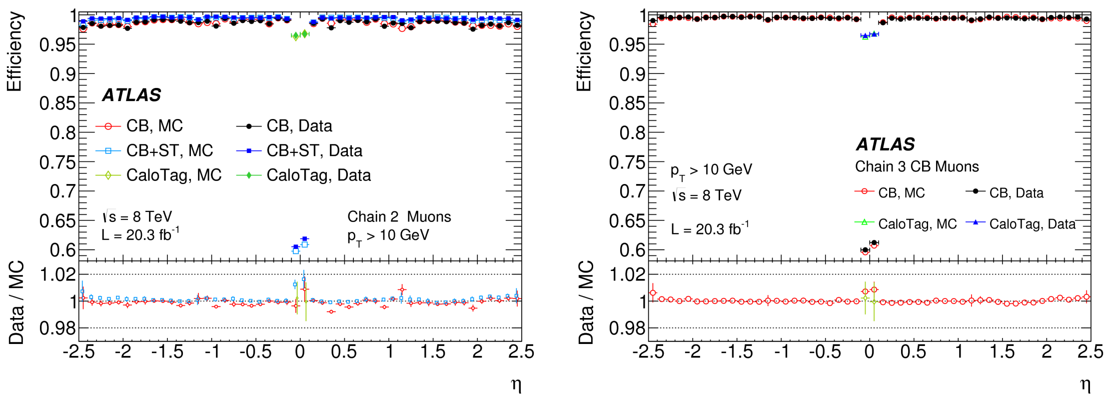

(a) barrel region **(b)** endcap region

Figure 3.17.: Left: Reconstruction efficiency for muons reconstructed in Chain 2 (MUID) as a function of the η for different muon reconstruction types. CaloTag muons are shown in the region $|\eta| < 0.1$, where they are used in physics analyses. It shows the results obtained with $Z \to \mu\mu$ and $J/\psi \to \mu\mu$ events. The error bars shown for the efficiencies represent the statistical uncertainty. The panel at the bottom shows the ratio between the measured and predicted efficiencies. The error bars show statistical and systematic uncertainties added in quadrature. Right: Analogous plot for Chain 3 (MUONS). [75]

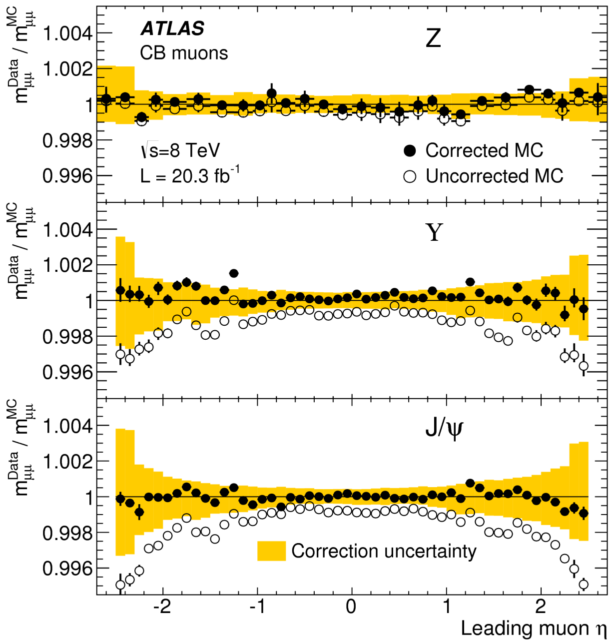

Figure 3.18.: Ratio of the fitted mean di-muon mass, for data and corrected MC from Z (top), Υ (middle), and J/ψ (bottom) events as a function of the pseudorapidity of the highest-p_T muon. The ratio is shown for corrected MC (filled symbols) and uncorrected MC (empty symbols). The error bars represent the statistical and the systematic uncertainty on the mass fits added in quadrature. The bands show the uncertainty on the MC corrections calculated separately for the three samples [75].

Chapter 4.

Experimental study of $b\bar{b}$ production using ATLAS 2012 8 TeV data

4.1. Analysis overview

The analysis note [80] has been submitted for review by ATLAS collaboration, and the following text is based mostly upon this note. The note contains original work by the author of this thesis.

The analysis studies b-quark production mechanisms via several kinematic distributions of B-hadrons produced in an event. B hadrons are unstable and cannot be measured directly, most of them decay after traveling fraction of a mm from the primary vertex where they were produced.

Therefore, the kinematic distributions of a $B\bar{B}$ system are studied through a proxy $J/\psi + \mu$ system, where one B hadron decays into a $J/\psi(\mu\mu) + X$, the second B hadron decays semileptonically into a final state containing muon. The latter muon is referred to as third muon in the following text.

The most sensitive parameters to the $b\bar{b}$ production mechanisms are the azimuthal angle difference $\Delta\phi$, angular separation ΔR and the asymmetry parameter A. Unfortunately, the strong signal found in asymmetry between transverse momenta of B hadrons $A = \frac{p_T(B_1) - p_T(B_2)}{p_T(B_1) + p_T(B_2)}$ is washed away when using $J/\psi + \mu$ proxies, see figure A.18 in the appendix.

The fits of $J/\psi + \mu$ were used to extract event yields. The signal is defined as non-prompt J/ψ and non-prompt muon.

The goal of this analysis is to obtain the differential cross sections for the proxy system binned in bins of:

- $\Delta\phi$, azimuthal angle difference between the J/ψ and $3^{rd}\mu$
- ΔR, defined as $\sqrt{(\Delta\phi)^2 + (\Delta\eta)^2}$ between the J/ψ and $3^{rd}\mu$
- Δy, difference in rapidities between the J/ψ and μ
- invariant mass m of the three muon system
- p_T of the $J/\psi + \mu$ system
- boost (y), defined as the magnitude of the average rapidity of the $J/\psi + \mu$ system
- $\frac{p_T}{m}$, the ratio of the transverse momentum of the three muon system to the invariant mass of the three muon system
- $\frac{m}{p_T}$, the ratio of the invariant mass of the three muon system to the transverse momentum of the three muon system

Even though these output cross sections are calculated for the $J/\psi + \mu$ system, it is possible to reconstruct the original BB distributions via deconvolution using $BB \rightarrow J/\psi + \mu$ proxy transfer matrix, for an example of such matrix see section 6.3.1. The number of the bins as well as the bin dimensions for each differential observable are listed in table 4.1.

Bin	$\Delta\phi$	ΔR	Δy	$p_T[GeV]$	$m[GeV]$	y_{boost}	$\frac{p_T}{m}$	$\frac{m}{p_T}$
1	0-0.1	0-0.2	0-0.1	0-10	3-8	0-0.1	0-0.25	0-0.5
2	0.1-0.25	0.2-0.4	0.1-0.2	10-15	8-15	0.1-0.2	0.25-0.5	0.5-1.0
3	0.25-0.5	0.4-0.8	0.2-0.4	15-20	15-22	0.2-0.4	0.5-1.5	1.0-2.0
4	0.5-1.0	0.8-1.3	0.4-0.7	20-25	22-25	0.4-0.7	1.5-3.5	2.0-4.0
5	1.0-2.0	1.3-2.2	0.7-1.2	25-40	25-35	0.7-1.2	3.5-5.5	4.0-15.0
6	2.0-2.3	2.2-2.7	1.2-1.9	40-60	35-50	1.2-1.7	5.5-30.	15.0-150.0
7	2.3-2.6	2.7-3.1	1.9-2.7	60-150	50-75	1.7-2.5		
8	2.6-2.9	3.1-3.8	2.7-4.8		75-200			
9	2.9-π	3.8-7.0						

Table 4.1.: List of chosen observables for the $J/\psi + \mu$ system and their binning.

In order to limit decays-in-flight background and increase triggering and reconstruction efficiency, all muons in an event are required to have transverse momentum larger than 6 GeV. The complete list of applied cuts is discussed in section 5.1. The signal yield and corresponding cross section measurements are extracted from the four-dimensional maximum likelihood fit. It consists of two two-dimensional fits, one for the J/ψ component, the other for the 3^{rd} muon component.

The list of observables, on which the fit is performed, consists of the following variables:

- J/ψ candidate invariant mass to separate J/ψ di-muons from background
- J/ψ candidate pseudo-proper lifetime to select non-prompt J/ψ candidates coming from B hadrons
- 3^{rd} muon transverse impact parameter d_0 to select muons coming from non-prompt sources
- output of a boosted decision tree (BDT) for 3^{rd} muon, which assesses the likeness of a muon candidate being a true muon. The BDT returns a number between -1 (high probability of a fake muon) to 1 (high probability of a true muon).

The J/ψ part of the model consists of 5 components, while the 3^{rd} muon model consists of another 5 components. They are fully described in section 6.1.1 and 6.1.2. In the 3^{rd} muon case, several templates are extracted from the MC, while as many as possible are extracted from the data. From the $pp \to J/\psi(\mu\mu) + X$ simulated events, the d_0 template for prompt muons was extracted. From the $pp \to BB \to J/\psi(\mu\mu) + X$ non-prompt MC, the extracted templates are:

- d_0 template for non-prompt 3^{rd} muons
- True muons and fake muons for the boosted decision tree training

The rest of 3^{rd} muon model templates such as pile-up background and fake J/ψ are extracted from the 2012 data.

4.2. Background analysis of the $J/\psi + \mu$ channel

The backgrounds affecting the analysis can be categorized into two categories, one related to the J/ψ and the other to the third muon.

- Fake J/ψ, that is $\mu^+\mu^-$ from the non-$c\bar{c}$ states such as multiple interactions, independent decay trees, B cascade decays ($b \to c + \mu + X \to s + \mu + X'$), muons coming from the decays of $K^\pm\pi^\pm/D$ mesons or combination of any aforementioned sources. All these can create a di-muon candidate in the J/ψ invariant mass range. This background is discussed in section 6.1.3.

- Prompt J/ψ that comes directly from the pp collision. They have pseudo-proper lifetime consistent with zero and are discussed in section 6.1.1.

- Fake third muon - the muon coming from the decay tree which contains a light meson, such as $K^\pm/\pi^\pm$ originating in the B meson decay or emerging in the primary or pile-up vertex alongside the primary B mesons. A boosted decision tree is trained to identify such event, see section 4.3.

- Pile-up muon, originating in multiple interactions during bunch crossing. This background is not correlated, and it should have a flat distribution in $\Delta\phi$. It is dealt with using a cut on difference of track z_0 coordinates between the 3^rd muon and the closest J/ψ muon. For details, see section 6.1.5.

- Muon that has originated in a D meson in the underlying event. Such events are discussed in section 6.1.7 and models are subtracted on the bin-by-bin basis from the fit.

- Decay of the B_c, such as $B_c \to J/\psi + \mu + X$. Similarly to prompt D meson background, such events are subtracted from the fit and it is discussed in section 6.1.6.

- Di-muon production via the Drell-Yan process [81]. This background is expected to be very small.

All the signal and background components are combined together and fit on the data is performed. The signal is extracted from the fit by requiring a non-prompt J/ψ and non-prompt muon which does not come from the decays-in-flight of a $K^\pm$ or $\pi^\pm$. In parallel to the recorded data, the Monte Carlo simulation samples have been processed through the full detector simulation and reconstruction, in order to compare MC predictions for distribution of observables with data.

4.3. Boosted decision trees

This analysis uses BDT, a method originating in multivariate analyses, to extract a number of fake muons in the data. Multivariate methods are often used in data analysis to extract correlations hidden from the usual rectangular cuts. For this purpose, artificial neural networks and boosted decision trees give satisfactory results. Given a muon candidate, BDT assigns to each muon candidate a weight, ranging from -1 to 1 based on the muon properties.

In BDTs, the selection is done on a majority vote on the result of a large number of individual decision trees, which are all derived from the same training sample by supplying different event weights during the training. Successive decision nodes are used to categorize the events out of the sample as either signal or background. Each node uses only a single discriminating variable to decide if the event is signal-like or background-like. Signal objects, in this case real muons, have BDT output weights close to +1. Using a set of variables associated with the muon candidate, a BDT is trained to create a set of binary splits of the data based on the input variables. Each variable is considered one at a time with a yes/no (signal/background) decision taken for each until a stop criterion based on signal purity is satisfied. In order to stabilize the BDT, a process termed boosting is applied where a set of multiple trees is used with the classification based on the majority decision of the set of trees.

The BDT analysis framework used is included in the TMVA toolkit (**T**he **M**ulti**V**ariate **A**nalysis) version 4 was used [82], which is fully integrated into the ROOT framework.

4.3.1. BDT input variables

The BDT is trained on two disjunct sets of real and fake muons, representing signal and background. Both sets are taken from Pythia8 BB MC datasets, see section 5.2.2. This simulation has been specially produced with full detector simulation of particle propagation to ensure proper modeling of hadrons decaying outside the ID. Signal muons are defined as reconstructed muons matched to a truth muon inside the truth muon collection matching to within $\Delta R < 0.02$. The signal muon must come from a semileptonic decay of a B-hadron. Background muons are defined as reconstructed muons matched to a truth muon that has a $K^{\pm}$ or $\pi^{\pm}$ parent. In this case, the reconstructed muon must match the DIF truth muon to within $\Delta R < 0.15$, or it must be matched to a charged $K^{\pm}$ or $\pi^{\pm}$ if there is no matching truth muon. All reconstructed muons are required to pass the standard muon quality cuts used in this analysis.

The variables with the most significant sensitivity to DIFs are:

- Momentum balance significance of a muon candidate calculated from ID and MS tracks
- Scattering significance in the ID
- Scattering neighboring significance in the ID
- η of the muon candidate

The BDT, which incorporates each of these variables, has potentially a much larger discriminating power than any of the individual discriminants alone. The number of BDT input variables is kept small to minimize any potential mis-modeling of the BDT performance between simulations and data. Usage of only four input variables does not negatively affect the BDT performance, since the goal is not to maximize the separation between fake and real muons, but to have sufficient separation to use the BDT output distributions as fit templates that accurately describe the data.

Momentum balance significance

If the $K^{\pm}$ or $\pi^{\pm}$ decays in flight into a muon and neutrino, this muon candidate should have larger difference between the measured ID and MS track momenta than real muon, since part of the momentum is carried away by a neutrino. One of the discriminants which is used to clean the muon candidate sample is the momentum balance, defined as:

$$\frac{\Delta p}{p} = \frac{p_{ID} - p_{MS} - \Delta p_{CALO}(p_T, \eta, \phi)}{p_{ID}},$$

where p_{ID} is the muon momentum measured in the ID, p_{MS} is the momentum measured in the MS and the p_{CALO} is the expected muon ionization loss in the calorimetric system. p_{CALO} can be measured in calorimeters or it can be a parameterized estimate of the ionization energy loss. A large significance of this variable should signal the case when a fake muon candidate decays outside of the ID and inside the calorimeter.

Scattering significance

The scattering significance S is a variable that characterizes deflections in the muon candidate trajectory resulting from decays in flight. For each measurement along the muon trajectory, the deviation in azimuthal angle of the measured hit position from the fitted trajectory, $\Delta\phi_i$, is calculated and compared to the expected deviation from multiple scattering, ϕ^{msc}. A signed variable $s_i = q\Delta\phi_i/\phi^{msc}$ is devised, which represents deviation from the expected value for hit position measurement i. The q in the expression represents the track charge. The scattering significance at the k-th detector layer $S(k)$ is defined as

$$S(k) = \frac{1}{\sqrt{n}}\left(\sum_{i=1}^{k} s_i - \sum_{j=k+1}^{n} s_j\right),$$

where n represents the total number of measurements of the muon candidate trajectory. The $S(k)$ yields a statistically significant value when the muon candidate has deviated between measurements k and $k+1$. An overall scattering significance is obtained from the maximum value of $S(k)$.

The scattering neighboring significance works in a similar manner. Track segment angles $(\delta\phi, \delta\theta)$ on either side of an ID scatterer are compared to search for track kinks.

The role of η variable is in helping to distinguish DIF muons, since a $K^\pm/\pi^\pm$ is more likely to decay to a muon at central rapidities where the meson traverses less detector material and is therefore less likely to interact hadronically. Since the fake muon BDT response is trained on the Pythia sample used throughout this analysis, it is important to estimate the model dependence of the $|\eta|$ distribution of $K^\pm/\pi^\pm$'s in the simulation. The model dependence arising from the use of $|\eta|$ in the BDT was found to be small.

The plots of selected variables for signal muons and decay-in-flight muons are shown in figure 4.1. The variables are chosen so that a potential discrimination of fake muons in both the ID and calorimeter systems is possible.

The BDT output for real and fake muons is shown in figure 4.2.

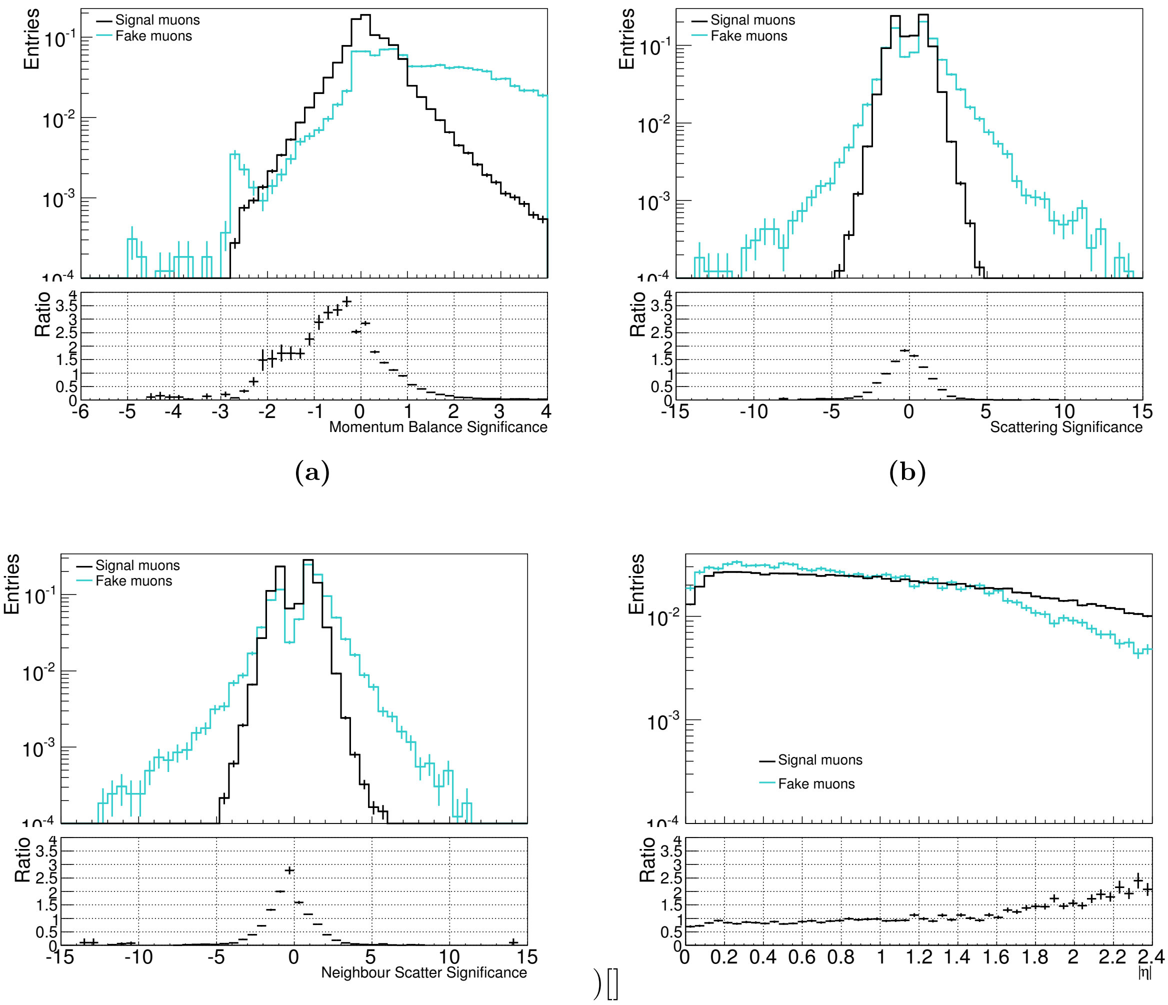

Figure 4.1.: The BDT training input distributions normalized to unity for signal muons (black) and fake muons (cyan). The momentum balance significance is shown in subfigure a) The closer the value is to 0, the higher the probability that a muon candidate is a true muon indeed. The cyan curve deviates significantly in the area of the positive energy loss, which is in fact due to the momentum carried away by the neutrino. Subfigure b) shows scattering significance distributions, with S being wider for the fake muons. c) displays similar scattering neighboring significance and finally d) is muon candidate pseudorapidity.

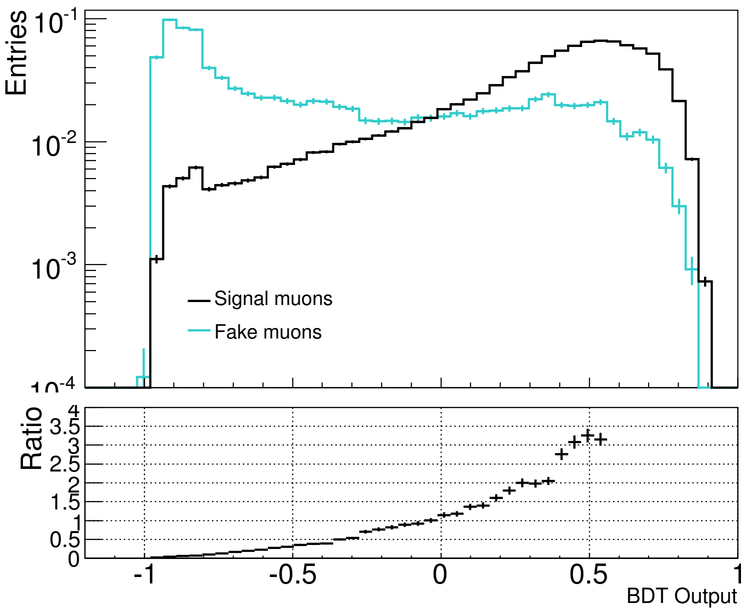

Figure 4.2.: Shape of the BDT output distribution for signal muons (black) and background fake muons (cyan). The true muon distribution tends to peak at positive values of BDT output discriminant, while fake muon distribution peaks at negative.

Chapter 5.

Monte Carlo simulations and real data selection

5.1. Dataset selection

The integrated luminosity during the LHC Run I data-taking campaign is shown in figure 5.1. The ATLAS experiment has collected approximately 22 fb^{-1} of proton-proton collisions at a center-of-mass energy of 8 TeV during the 2012 data taking. During the data taking, the LHC has reached the highest instant luminosity ever reached at particle accelerator ($7.73 \times 10^{33}\text{cm}^{-2}\text{s}^{-1}$). The data available for analysis are usually less than the amount delivered by the LHC due to data taking inefficiencies and data quality losses.

The total integrated luminosity of the sample used in this analysis with Standard-GRL_All_Good good run list[1] is 11.449 $\pm$ 2.8% fb^{-1}. The luminosity was calculated using the iLumiCalc tool.

For the measurement presented in this thesis, 2012 the ATLAS B-physics stream data in periods C6-G at $\sqrt{s} = 8$ TeV were selected. This selection takes into consideration the availability of appropriate triggers. Earlier data taking periods do not contain the EF_2mu4T_Jpsimumu_L2StarB trigger in the trigger menu used for triggering on J/ψ events. In earlier periods of 8 TeV running, the di-muon trigger was biased towards lower J/ψ lifetimes.

[1] Good run list (GRL) is a list of runs and lumiblocks where relevant subsystem Data Quality (DQ) status flags signalize good quality of data for physics use. The flags are assigned for every detector subsystem per luminosity block.

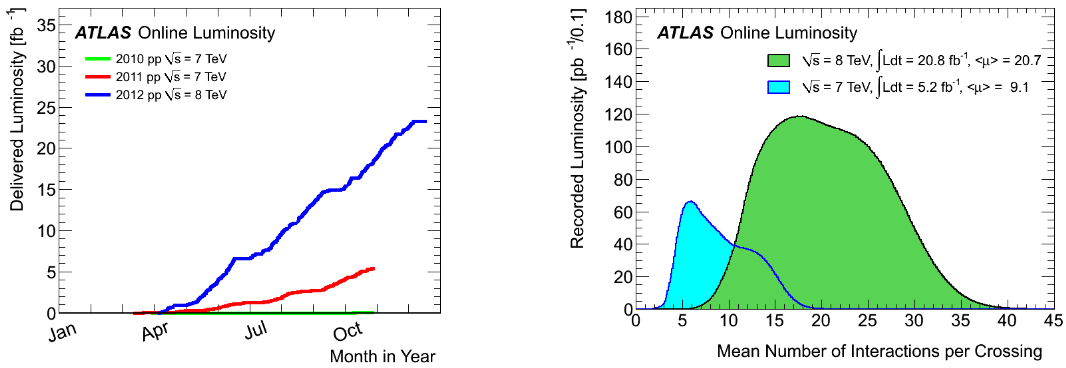

(a) Delivered luminosity for 2010, 2011 and 2012 *pp* data taking (LHC run I).

(b) Number of interactions per bunch crossing (μ).

Figure 5.1.: a) Cumulative online luminosity versus day delivered to ATLAS during stable beams and for *pp* collisions. b) Luminosity-weighted distribution of the mean number of interactions per crossing (μ) for the 2011 and 2012 data taking period. The integrated luminosities and the mean μ values are given in the figure. The mean number of interactions per crossing corresponds the mean of the Poisson distribution on the number of interactions per crossing calculated for each bunch. It is calculated from the instantaneous per bunch luminosity as $\mu = \mathscr{L}_{bunch} \cdot \sigma_{\text{inel}}/f_r$, where $\mathscr{L}_{bunch}$ is the per bunch instantaneous luminosity, σ_{inel} is the inelastic cross section which we take to be 71.5 mb for 7 TeV collisions and 73.0 mb for 8 TeV collisions and f_r is the LHC revolution frequency. More details on this can be found in [83].

In both ot the the 2012 ATLAS dataset and MC simulation, muons come from the so-called 3^{rd} chain (see section 3.2.10 for details), which combines the best properties of STACO and MUID algorithms. For selected events in both data and MC samples, following conditions must be satisfied:

- There must be at least three reconstructed muons in the event. In addition, all of these muons must be combined (i.e. must have ID and MS tracks)
- *Medium+* muon selection criteria, recommended by the ATLAS muon combined performance group.
- All muons must fall within the $|\eta| < 2.5$ volume of the detector, and must pass the requirement of 6 GeV p_T
- Number of pixel detector hits $> \ 0$
- Number of SCT hits+number of crossed dead SCT sensors > 4

- Number of pixel holes + number of SCT holes < 3
- If track 0.1 <η <1.9: number of TRT hits and number of TRT outliers > 5
- Fraction of TRT hits and TRT outliers that are TRT hits > 90 %
- There must be at least one reconstruced J/ψ candidate vertex in event with di-muon invariant mass within range of 2.6-3.5 GeV to have sufficient space for sidebands sampling
- Event must be triggered by EF_2mu4T_JPsimumu_L2starB trigger (required only on the data sample)

Furthermore, muons that form a J/ψ candidate must fall within the $|\eta| < 2.3$ interval and reconstructed J/ψ muons must be matched to the trigger objects (required only in the data sample). Since this analysis considers events with more than two muons, formation of more than one J/ψ candidate vertex frequently happens. In such events, the opposite-charge di-muon pair with invariant mass closest to the J/ψ PDG value is taken to be the J/ψ candidate in the event.

The trigger selected for this analysis is EF_2mu4T_Jpsimumu_L2StarB. It is a di-muon trigger with minimum muon p_T of 4 GeV. In addition, it imposes a loose cut on the di-muon mass and muons are also required to have opposite charge and be consistent as coming from the same production vertex.

This trigger is a dedicated trigger for analysis in the B-physics group at ATLAS and therefore it is not heavily prescaled throughout the running. The early runs of 2012 suffered from low efficiency for events with large lifetimes (EF_2mu4T_JPsimumu used IDSCAN for L2 track reconstruction), hence the trigger was modified to compensate for that loss. It is required that event fired the EF_2mu4T_JPsimumu_L2starB trigger. It is a B-physics topological trigger, which requires two muon RoIs on the LVL1 level with transverse momentum greater than 4 GeV. On the second level, it must pass the L2_2mu4T_Jpsimumu_L2StarB trigger. This trigger is an improvement over older triggers used in B-physics analyses which had a bias towards J/ψs with small pseudo-proper lifetime.

5.2. Monte Carlo truth samples

Events originating in MC simulation are used for multiple purposes in this analysis. Two MC samples were used for creation of templates, the BB template which simulates the event topologies, and PP MC which simulates the prompt J/ψ production background.

In General, ATLAS MC generation process can be divided into five steps:

1. Physics event generation using MC event generator such as Pythia into a HepMC compatible format. Final state particles deemed stable by the generator are fed into following processing stages.
2. Simulation of the detector response using Geant4 package. This simulation includes detailed ATLAS geometrical and material model. Geant4 provides suitable physics models for unstable particle decays and for simulation of particle interactions with matter.
3. Creation of hit collections, digitization. During the digitization, hits from particles coming from pile-up (multiple interactions) are added from the minimum-bias MC sample. Therefore, there is no truth information for pile-up.
4. Event reconstruction, creation of physics objects.
5. Skimming, slimming and thinning of produced datasets and collections which serve as input into analysis.

5.2.1. $pp \rightarrow J/\psi + X$

A sample of 10^7 $pp \rightarrow J/\psi(\mu\mu) + X$ events was used to simulate direct production of J/ψ. Here, the J/ψ is created by Pythia 8.175 by a combination of color octet and color singlet mechanisms implemented as matrix elements. The dataset is designated as mc12_8TeV.208002.Pythia8B_AU2_CTEQ6L1_pp_Jpsimu6mu6.merge.AOD with config tags e1331_a159_a180_r3549. This dataset was processed into ROOT-readable ntuples, with cut on event kinematics and reconstruction defined in section 5.1.

The simulation is performed corresponding to the LHC 2012 running with 50 ns bunch spacing. There are two variants of MC12 with respect to added pile-up interactions, a and b. While the former contains only an estimate of number of parallel interactions before the 2012 running, the MC12b has updated pileup samples with a smaller beam spot size compared to MC12a, which mimic recorded data more closely. Furthermore, the μ (number of multiple interactions) profile is updated modeling more closely the μ distribution in the 2012 8 TeV data. The default physics list for Geant4 is QGSP_BERT. Detector response simulation was performed in ATHENA package with standard geometry, pile-up events are generated by Pythia8 minimum bias events with the AM2 tune.

The prompt template was filled using the $pp \to J/\psi$ Pythia MC, but with a modified event selection. Events were required to have at least two muons, as only a small fraction contained three reconstructed muons passing the quality cuts, all the other cuts were the same as the nominal selection. Without three muons in every event the differential variables cannot be calculated, so the same template formed on the inclusive MC sample is used for the prompt template in each differential fit. To minimize the impact of statistical fluctuations, the differential templates are smoothed using a kernel estimation procedure [84] before being fit to data.

5.2.2. $pp \to BB \to J/\psi + X$

The sample was generated using new Pythia 8.186. A Wrapper called PythiaB is used in ATLAS B-physics groups to speed-up the event generation. PythiaB [85] is an interface to Pythia, dedicated solely to simulation of beauty events. It is basically an event filter, speeding up the event simulation process. It allows end user to select physics channels of interest and setting kinematic cuts on events. Pythia8B is a dedicated interface to Pythia8.

Symmetric BB sample

The default B-physics MC available for user analyses has J/ψ coming from the b-quark hadron. In an event with a $b\bar{b}$ pair which subsequently hadronizes into a pair of $B\bar{B}$ hadrons, B has closed all decay channels except $J/\psi + X$ and is therefore forced to decay this way. On the other hand, $\bar{B}$ meson has all its decay channels opened and can decay in any way programmed into the generator.

Due to the design of PythiaB, the J/ψ decay channels are closed on the generator level. All J/ψs in the event (if there are more) must decay into a $\mu^+\mu^-$ pair. This causes an overestimate of the number of events containing four muons from di-J/ψ decays. To correct for this effect, events containing four muons from two different J/ψ mesons are weighted by the factor $1/\mathrm{Br}(J/\psi \to \mu^+\mu^-)$, which is $\approx 5.93\%$.

At the end, b-quark in the other $\bar{B}$ meson decays weakly which dictates the charge of the 3^{rd} muon coming from the semileptonic decay. This is sufficient for most analyses, but it might introduce a bias in events where more than two muons are necessary. In order to minimize systematic error, a symmetric sample was devised where the J/ψ is a product of decay of either B or anti-B hadron.

There are two $b\bar{b} \to J/\psi + \mu$ samples, in the first one b-quark is forced to hadronize into a B meson which is in turn forced to decay into a J/ψ. The second sample is charge-symmetric to the first one.

Detector simulation

The full detector simulation is time consuming, and therefore ATLAS has opted for fast simulation. In average, 80 percent of the full simulation time is utilized by simulation of particle interactions in the calorimetry region. It is caused primarily by electron and photon showers in the electromagnetic calorimeter and hadronic cascades in the hadronic calorimeter, where a large count of secondary particles is created in cascades in a complex geometry of the calorimetric system. To speed up the tedious computation process, the ATLAS collaboration has developed detector simulation techniques to achieve this goal embodied in the AtlfastII (Atlas Fast Simulation package version II). It makes use of the FastCaloSim package [86] which reduces the simulation time requirement by one order of magnitude by means of parameterizations of the longitudinal and lateral shower energy profile. These models contain parameterization of detector energy deposition response and resolution in calorimetric layers. Shower shape parameterization is based on average single particle shapes, fluctuations of shapes are not taken into account.

In a more detailed observation, AtlfastII is a combination of full detector simulation and fast simulation. Typically, the ATLAS-generated MC samples are simulated fully only in the ID region by a full G4 simulation. When particles leave the ID area and are about to enter the calorimeter regions, propagation of all particle types but muons is terminated and further simulation is done using FastCaloSim. For muon simulation, Geant4 full-sim is used in the whole ATLAS region. For simulation of single K, π, γ and electrons, parameterized shower model is used.

This approach is applicable with little or no physics penalty in most physics analyses, but it is not the case for the analysis presented here. Due to the long lifetime and other physics properties of pions and kaons, which can decay-in-flight into muons, full detector simulation is obviously necessary to the cover entire volume of ATLAS.

Final $B\bar{B}$ Monte Carlo

Each of the $b\bar{b} \to J/\psi + X$ datasets has 10^7 events:

- mc12_8TeV.208207.Pythia8B_AU2_CTEQ6L1_anti_bb_Jpsimu6mu6.merge. AOD.e3363_s1986_s1776_r4485_r4540 Inclusive $BB \to J/\psi + \mu$ production, J/ψ comes from $\bar{B}$ hadron
- mc12_8TeV.208202.Pythia8B_AU2_CTEQ6L1_bb_Jpsimu6mu6.merge. AOD.e3363_s1986_s1776_r4485_r4540 is similar than the one above, except that J/ψ comes from B hadron.

Pythia8 was tuned using the AU2 CTEQ6L1 tune [87] and [88]. Additionally, Pythia8B was set to require at least two muons in the final state with transverse momentum at least 6 GeV and their pseudorapidity must fall within the fiducial volume of the pixel detector within $|\eta| < 2.5$.

In the analysis presented in the following chapters, both samples are combined together.

In addition to this sample, an inclusive sample was produced using the Herwig++ v2.7.1 event generator [89]. The generator was tuned using the UE-EE-5-CTEQ6L1 tune, which incorporates CTEQ6L1 parton distribution function set and UE-EE5 [32] tune of the underlying event parameters. This sample was not processed through full detector simulation, and it is rather used as an alternative model to Pythia8 for backgrounds in data.

5.2.3. $B\bar{B}$ MC event categories and event selection

Since this sample is an important source of templates, each muon in an event is categorized according to its origin, therefore eight categories were devised. These categories are coming from the truth-matching of reconstructed muons to the particle-level MC truth collection contained in data. The truth-matching is performed with a ΔR matching between the reconstructed and truth object. The ΔR is set 0.02 for true muons and 0.15 for muons coming from the decays-in-flight.

In order to model signal and backgrounds in the BB MC, muons have been classified into eight classes according to the 3^{rd} muon heritage. Each muon can belong to a single class only.

- 1 - Muons coming from the J/ψ decay, which is in turn coming from a B hadron.
- 2 - Signal category where the $3^{rd}\mu$ coming from the other B hadron, but not from J/ψ decay. It can also include chained semileptonic decays such as $B \rightarrow D + X$, where $D \rightarrow \mu + Y$
- 3 - Muon has B heritage but also a J/ψ parent, probably di-J/ψ event or B_c
- 4 - Muon coming from generator-level stable particle
- 5 - Other matched muons, not other categories
- 6 - Decays in flight muons, $K^{\pm}/\pi^{\pm}$ are decayed by Geant4
- 7 - Not truth-matched muon, probably a pile-up muon added during digitization
- 8 - Charmed hadron decays, muons from promptly produced charmed hadrons

The signal selection criteria require p_T of all three muons to be greater than 6 GeV, in addition to:

- Out of three or more muons in an event, two must come from a J/ψ decay which has B-hadron in its lineage, which correspond to the first category introduced above.
- Third muon is the highest p_T muon of the muons which have B hadron in lineage and come from category 2.

All truth muons are dressed by a 4-vector addition of real photons with non-hadronic heritage within a cone of $\Delta R < 0.1$ from the muon. Otherwise, reconstructed object cuts are identical to the cuts applied to 2012 data as described in the previous section.

5.3. Muon triggering and offline reconstruction efficiency

In order to measure cross section, measured event yields must be cleaned from the detector effects such as limited reconstruction and triggering efficiencies. The inclusive cross section is calculated as:

$$\sigma_{(J/\psi+\mu)} = \frac{N_c}{\mathscr{L}},$$

where $\mathscr{L}$ is the integrated luminosity of the analysis sample and N_c is the number of signal events seen by the detector after correction for triggering and reconstruction inefficiencies. Each event is assigned weight calculated according to its global efficiency, including trigger and reconstruction efficiencies. The weight w is defined as

$$w = \frac{1}{\epsilon_{reco} \cdot \epsilon_{trig}},$$

where ϵ_{trig} is the per-event efficiency of the di-muon trigger firing for the signal event and the ϵ_{reco} is the combined offline efficiency of reconstruction of all signal muons in the event. Both trigger and offline reconstruction efficiency are extracted from the 2012 data.

5.3.1. Trigger efficiency Correction

The inefficiencies associated with the EF_2mu4T_Jpsimumu_L2StarB trigger are treated by correction, which is applied as a part of the event weight. This correction is factorized into four terms:

$$\epsilon_{trig} = \epsilon^1_{ROI}(p_T, q\cdot\eta) \times \epsilon^2_{ROI}(p_T, q\cdot\eta) \times c_{\mu\mu}(\Delta R, y_{\mu,\mu}) \times c_{\mu\mu\mu}(\Delta R_{min}),$$

where $\epsilon^{1,2}_{ROI}$ are the single muon trigger efficiency corrections related to single muon ROI. They are identical for muons of both charges. The $c_{\mu\mu}$ factor connects the two single muon trigger RoIs into a di-muon trigger. It corrects for overlapping of muon ROIs and also accounts for vertexing and opposite muon charge requirements. The c_{μ^3} factor corrects inefficiency of a di-muon trigger in three muon events and it is discussed in section 5.3.3.

The $c_{\mu\mu}$ correction factor for the di-muon trigger is composed of two components and it can be factorized as:

$$c_{\mu\mu}(\Delta R, |y^{\mu\mu}|) = c_a(y^{\mu\mu}) \cdot c_{\Delta R}(\Delta R, |y^{\mu\mu}|),$$

where c_a is a correction for the di-muon vertex and opposite charge requirements [90]. It is derived using the EF_2mu4T_DiMU_noVTX_noOS trigger which does not perform a vertex fit and does not require muon tracks of the opposite charge. The $c_{\Delta R}$ correction corrects for effects of efficiency loss of the di-muon trigger if the two muons are close enough together and fall into a single RoI. The ϵ_{ROI} efficiency is parameterized as a 2D map in bins of p_T and $q \cdot \eta$, see figure 5.2. The $c_{\mu\mu}$ factor is parameterized as a function of the ΔR separation of the trigger muons, it is calculated in three separate di-muon rapidity intervals ($|y| < 1.0, 1.0 < |y| < 1.2$ and $1.2 < |y| < 2.3$) The data-driven $c_{\mu\mu}$ values are shown in figure 5.3, subfigures on top.

The single muon trigger efficiency map is extracted using a tag and probe method on 2012 di-muon J/ψ candidate data. In this method, one of J/ψ muons is required to fire a single muon trigger. The single muon trigger efficiency map is acquired for the probe muon as the ratio of fitted J/ψs for events firing the single muon trigger in question and EF_2mu4T_Jpsimumu_L2StarB, to the ratio of fitted J/ψs firing just the single muon trigger. The resulting map $\epsilon_{ROI}(p_T, q \cdot \eta)$ carries the efficiency information, but due to the high-p_T tag muons it requires correction to the low-p_T region.

During the 2012 data taking period, very high trigger prescale was set on the low p_T single muon triggers. This resulted in the tag muon is a single muon trigger having a 18 GeV threshold. Because of this high muon p_T threshold, the J/ψ candidates in events passing both the EF_2mu4T_Jpsimumu_L2StarB and single muon trigger are biased towards a high p_T. The resulting boost of the J/ψ candidates does not correspond to the events triggered by the EF_2mu4T_Jpsimumu_L2StarB trigger, since it applies a 4 GeVmuon p_T threshold for each muon ROI, and therefore it accepts events with wider opening angles of the J/ψ decay muons.

The correction for this high-p_T bias in data-driven trigger efficiency map is based on an inclusive J/ψ MC sample. Two new MC-derived trigger efficiency maps are produced, first one using the exactly same procedure as for the data-driven map, and the second map using a 4 GeV p_T threshold single muon trigger, which is available in the MC. The ratio between the low- and high-p_T threshold maps derived from simulation is applied to the data driven map. This step corrects the map to the full kinematic range of J/ψ decay

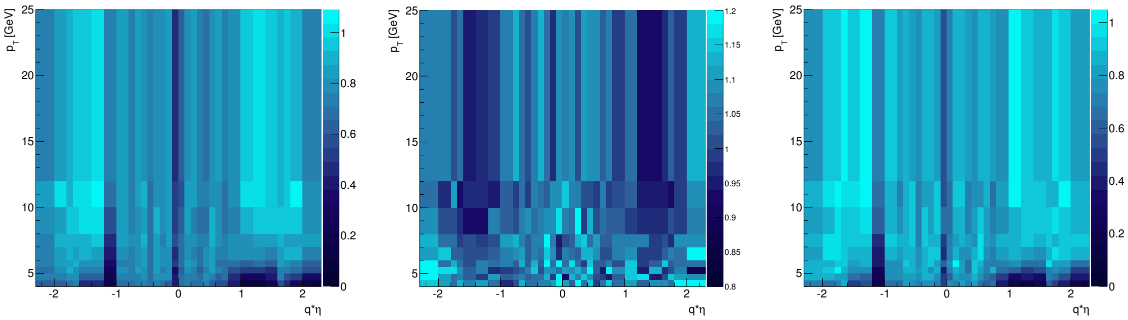

(a) Data-Driven with high-p_T tag muon **(b)** MC-based correction for low p_T J/ψ **(c)** Data-Driven map with MC correction applied

Figure 5.2.: Color-coded 4 GeV single muon trigger efficiency maps showing data-acquired map biased with high-p_T tag muon, the MC-derived correction and finally the data-driven map with MC correction applied.

muons in the dataset. The original data driven ϵ_{ROI} map, the MC based corrections and the corrected maps used for the analysis can be seen in figure 5.2. The $C_{\mu\mu}$ term is also corrected by a MC factor using the same procedure and is shown in figure 5.3, bottom. Interested reader can find more details about the trigger efficiency corrections in [80].

5.3.2. Trigger efficiency event weight

Since the event weight is taken to be the reciprocal value of efficiency, a non-linear effect arises which may bias the analysis. Since taking the inverse of a variable is a non-linear transformation, propagating the uncertainty on the efficiency to the uncertainty of the event weight must be performed carefully. Considering the shape of the $f(x) = 1/x$ transformation, small perturbations around $x \pm \delta x$ result in larger deviations of $\delta f(x)$ for x values close to 0 than they are for values close to 1. With the symmetric error on efficiency maps, this translates to a larger contribution for downward fluctuations of the efficiency.

A method was developed to counter this effect. Each bin in the trigger efficiency map has an associated uncertainty, resulting from the statistics of the data control regions used in the derivation of the map. A Gaussian probability density function can be formed for each map bin, representing the range of possible efficiency values. The Gaussian probability density functions are constructed using the measured trigger efficiency (for

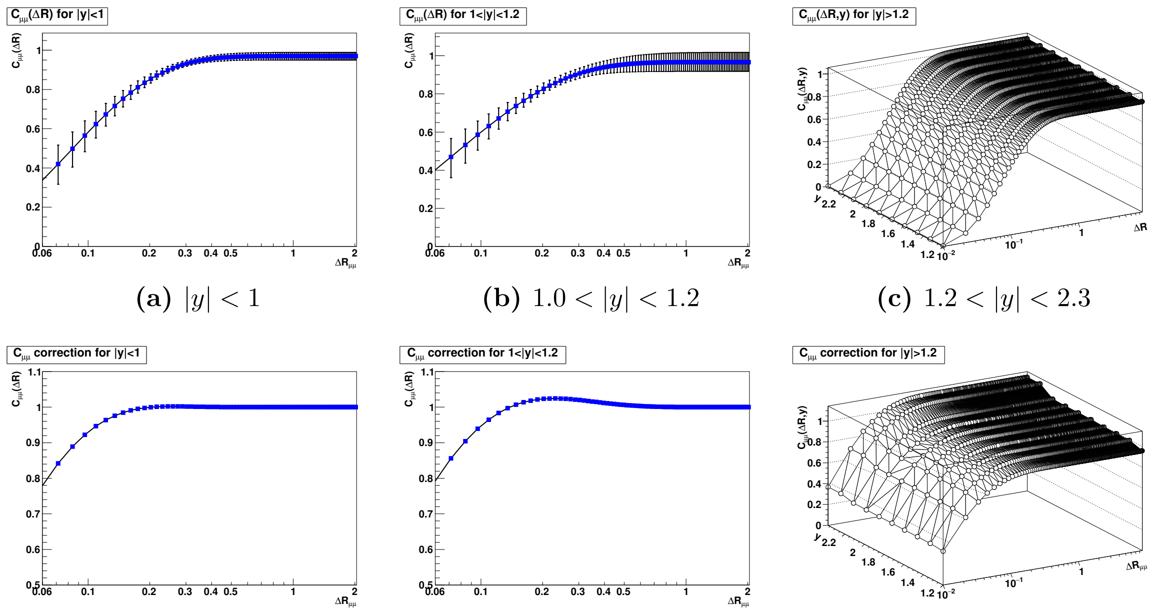

(a) $|y| < 1$ **(b)** $1.0 < |y| < 1.2$ **(c)** $1.2 < |y| < 2.3$

(d) $|y| < 1$ **(e)** $1.0 < |y| < 1.2$ **(f)** $1.2 < |y| < 2.3$

Figure 5.3.: The values of $c_{\mu\mu}$ for different bins of rapidity. Top row of plots represents data-driven factors for three different J/ψ rapidity regions. Bottom row shows the MC-based correction to data-driven $c_{\mu\mu}$ correction in the same rapidity binning.

a given map bin) as the mean value and associated uncertainty as the width of the corresponding Gaussian distribution.

The method consists of three steps:

1. Formation of a pseudo-efficiency map by random sampling for each map bin from the associated Gaussian distribution function. A set of 200 pseudo-efficiency maps is created by repeating this procedure 200 times. The data are corrected for trigger efficiency using each pseudo-map in turn to find the total number of events in the re-weighted dataset after applying the trigger efficiency correction. The distribution of the number of weighted events in the dataset, from using each pseudo-map, is used to assess the impact of the average efficiency correction and its uncertainty.

2. The total weighted event yield for the dataset after correction from each pseudo-map is fitted with a Gaussian function, $\mathcal{G}_{tot}$.

3. The mean of $\mathcal{G}_{tot}$ gives the nominal weighted event yield after corrections for trigger efficiency and the width is taken as a systematic uncertainty on the trigger efficiency weighting procedure. The mean of $\mathcal{G}_{tot}$ is not equal to the event yield using the

nominal efficiency map because of the $1/x$ transformation from efficiency to event weight, although the effect is small ($< 1\%$).

The weighted event yield after re-weighting the inclusive dataset by each pseudo-map and the fitted $\mathcal{G}_{tot}$ function can be seen in figure 5.4, the nominal map event yield is indicated with the vertical arrow. The analysis is performed using the nominal reconstruction map, the difference between the mean of $\mathcal{G}_{tot}$ and the result using the nominal map is applied as a correction to the event yield used to determine the cross section. This correction is calculated and applied separately to each differential observable bin.

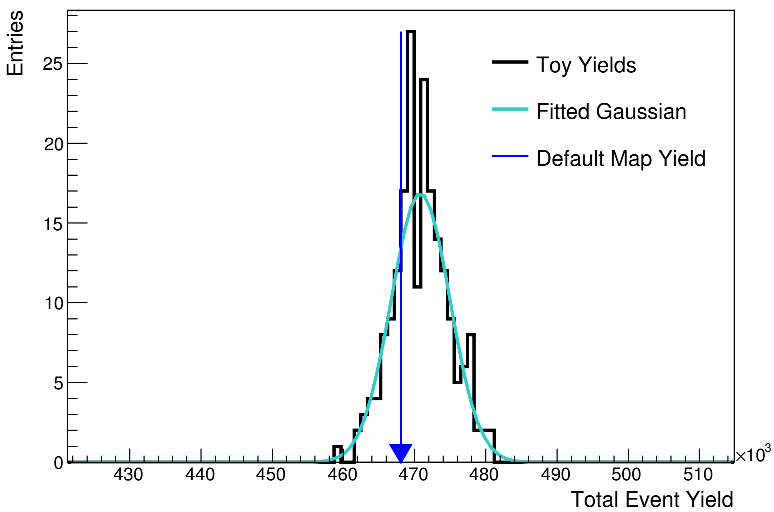

Figure 5.4.: Total weighted event yield (black histogram) when using the toy trigger efficiency maps. The distribution is fitted with a Gaussian which corrects the event yield.

The efficiency provided by the ATLAS collaboration was obtained by the Tag-and-probe method [91].

5.3.3. Third muon trigger efficiency corrections

The motivation for this correction is to correct for trigger inefficiency in the case of multiple muons falling into the same trigger region of interest (RoI). In three-muon events, the muon coming from the semileptonic decay of another B hadron can fall close to the RoIs of J/ψ muons. This effect is more pronounced when the muons are of the opposite charge.

The MC based correction factor is taken to be the reciprocal value of triggering efficiency, parameterized as a function of ΔR_{min} for two combinations of muon charge between the third muon and the closest of the trigger muons. This efficiency is derived by fitting a linear function to the ratio of signal MC events firing the trigger to all true signal events as a function of the separation of the third muon to the closest J/ψ muon. Events are corrected on the event-by-event basis by applying additional event weight.

The linear function used for fitting is defined as $C_{3\mu}(\Delta R_{min}) = min(c_1 + c_2 \cdot \Delta R_{min}, k)$, where c_1 is the intercept and c_2 is the slope. The c_{3mu} is limited to a maximum value of k. The value of k is extracted by a fit of a constant function in a range of $2 < \Delta R_{min} < 4$. The triggered events are already corrected for di-muon trigger inefficiency by a weight factor, which includes RoI efficiency maps and $C_{\mu\mu}(\Delta R, y_{\mu,\mu})$.

Figure 5.5 shows the three-muon trigger efficiency as a function of ΔR between the closest J/ψ muon to the selected third muon in the event.

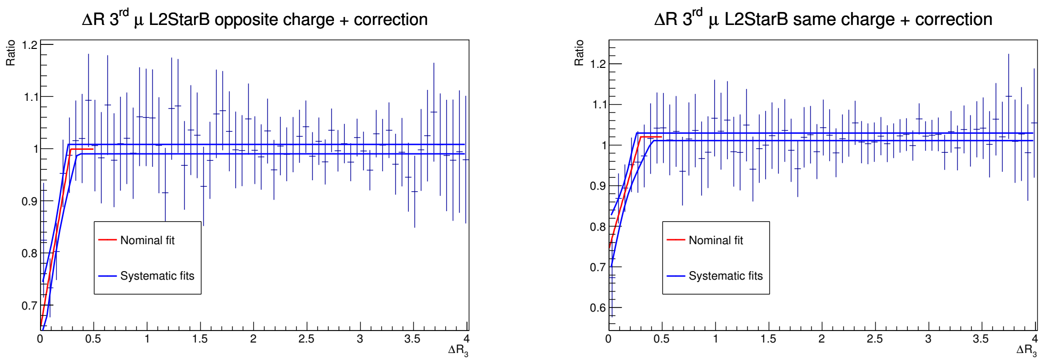

(a) Same charge **(b)** Opposite charge

Figure 5.5.: The trigger efficiency for same and opposite sign muons combinations as a function of ΔR between the closest J/ψ muon to the selected third muon in the event. The red function is the nominal fit to the efficiency drop.The blue functions show the systematic variation used by varying the fitted parameters from the nominal fit within errors.

This method is limited by statistical uncertainties at low values of ΔR. The systematic errors induced by this correction are taken to be fit errors calculated from error propagation using fit covariance matrix.

5.3.4. Muon offline reconstruction efficiency

Similarly to the trigger efficiency corrections, events are corrected for muon reconstruction efficiency for each of the signal muons in an event. The muon offline reconstruction efficiency consists of two terms, the probability that a track is reconstructed in the ID and also in the MS.

The efficiency for a single muon is given by:

$$\epsilon_{reco} = \epsilon_{trk}(p_T, \eta) \times \epsilon_{\mu}(p_T, q \cdot \eta),$$

where q is the electric charge of the muon, ϵ_{trk} is the efficiency of inner detector track reconstruction, measured to be $99.5 \pm 0.5\%$ over the full kinematic range [92]. Each muon has a 0.5% uncertainty on this track reconstruction assigned as a systematic. The total muon offline reconstruction efficiency in the event is taken as the product of the three individual efficiencies for each muon. The $\epsilon_{\mu}(p_T, q \cdot \eta)$ is the muon reconstruction efficiency map assuming there is an ID track. It was acquired using a tag and probe method on $Z \to \mu^+\mu^-$ high-p_T muons and $J/\psi \to \mu^+\mu^-$ low-p_T data [92]. The correction map can be seen in figure 5.6.

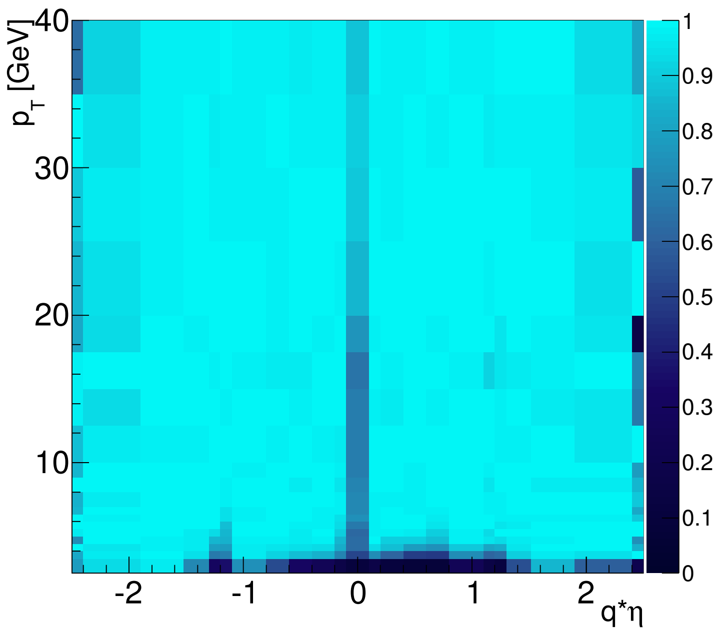

Figure 5.6.: Muon reconstruction efficiency map as a function of (p_T vs $q \cdot \eta$). The hole around the $\eta \approx 0$ is due to the MS region which is only partially equipped with muon chambers due to cabling.

An identical procedure outlined for the trigger efficiency is used to correct the data yield for muon reconstruction inefficiencies. A set of pseudo single muon efficiency maps is produced by sampling in each bin from a Gaussian distribution function, with mean taken from nominal muon reconstruction map value and width from the error on this. The data is weighted using each pseudo map and output for all the total weighted event yields is fitted with a Gaussian function, shown in figure 5.7. The difference between the mean of this distribution and the result using the nominal map is applied as a correction for the event yield in each differential analysis bin, the width is taken as a systematic uncertainty on the muon reconstruction efficiency. As the muon reconstruction efficiency is generally close to unity over the kinematic range of muons in the analysis, the effect of the non-linear behavior when considering the errors on the nominal map is less pronounced here. Thus the correction taking the result using the nominal map to the mean of the toy maps is small, typically $< 0.2\%$, although it is still derived and applied for each differential observable bin.

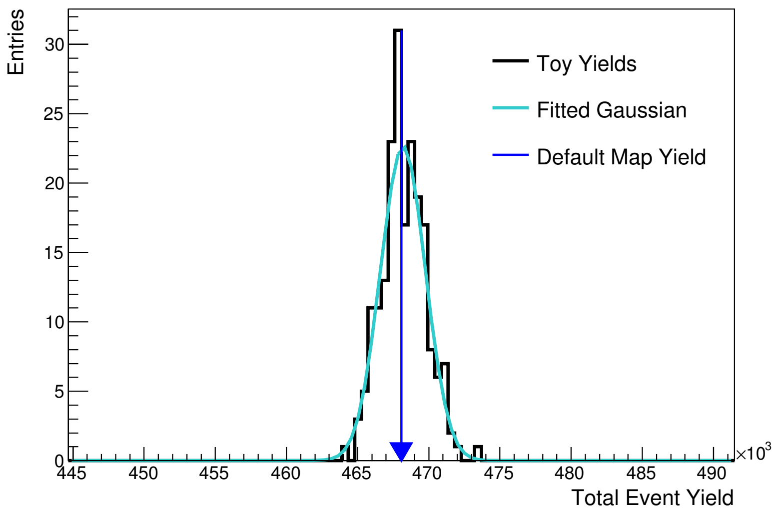

Figure 5.7.: Total weighted event yield when using the pseudo muon reconstruction efficiency maps (black histogram). The distribution is fitted with a Gaussian which corrects the event yield.

5.3.5. Monte Carlo muon reconstruction efficiency corrections

A correction for muon reconstruction efficiency is applied to muons in the Pythia MC samples so they are consistent with the dataset. The MC is used to form templates that are fit to the reweighted dataset, so it is important that the muons in the MC have been unfolded in the same manner as the muons in the dataset used in the fits. The correction was parameterized in the same $(p_T, q \cdot \eta)$ bins as the correction in data. It is calculated as the ratio of the number of reconstructed muons to the truth muons, for reconstructed muons that have been matched spatially to a truth muon, $\Delta R(\mu^{truth}, \mu^{reco}) < 0.02$, and is derived only for reconstructed muons passing the standard muon selection criteria. The efficiency map is shown in figure 5.8. An event-by-event re-weighting corrects for each muon reconstructed in the MC samples.

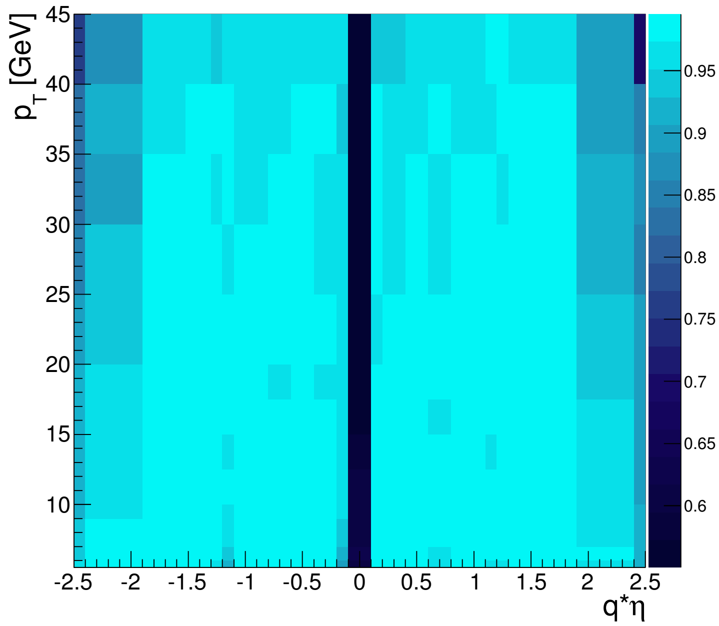

Figure 5.8.: 2D MC muon reconstruction efficiency map parameterized in bins of $(p_T, q \cdot \eta)$.

Chapter 6.

Signal and background modeling

In this chapter, modelling of signal and background components is discussed. For the fitting, a two-dimensional model of J/ψ mass and lifetime was devised. Also, a second 2D model for the 3^{rd} muon was implemented. These models are combined together to extract event yield of signal events.

6.1. Signal and background models

6.1.1. J/ψ mass and lifetime model

The J/ψ reconstruction employs the J/ψ reconstruction algorithm $JPsiFinder$, which combines the information from muon tracks and it uses only track parameters from ID track collection. The $JPsiFinder$ performs a muon vertex refit.

The J/ψ can emerge directly from the pp collision (prompt production), it may come from the decay of higher excited state of charmonium or finally it may be a product of the decay of B hadrons (non-prompt production). B hadrons have the lifetime measured in picoseconds and therefore, in order to identify the non-prompt J/ψ, an useful discriminating variable is the pseudo-proper lifetime, defined as:

$$\tau = \frac{L_{xy}\, m_{\mathrm{PDG}}^{J/\psi}}{p_T^{J/\psi}},$$

where L_{xy} is the transverse distance of the J/ψ vertex from the primary interaction vertex, $m_{\mathrm{PDG}}^{J/\psi}$ is the world average J/ψ invariant mass and $p_T^{J/\psi}$ is the transverse momentum of the quarkonia system. Prompt J/ψ has τ consistent with 0, while the J/ψ which is produced in B hadron decay has a decay vertex displaced from the primary vertex due to the B lifetime.

The simultaneous mass-pseudoproper lifetime fit consists of the following five components:

- **Prompt J/ψ component**, representing prompt production of J/ψ. the invariant mass is modeled as a Crystal Ball function [1] plus a Gaussian. The lifetime part is modeled as a detector lifetime resolution function, since prompt J/ψ have ab definitio $\tau \equiv 0$.

- **Non-prompt J/ψ component**, representing J/ψ candidates originating in decays of B hadrons. While the mass component is modeled in the same fashion as in the prompt J/ψ case, the lifetime component is a single-sided exponential convoluted with the same detector lifetime resolution function.

- **Prompt J/ψ background** (fake prompt J/ψ candidates) is modeled as a 0^{th} order polynomial. The lifetime part is modeled as a detector lifetime resolution function.

- **Single-sided fake J/ψ background**, where di-muon invariant mass is represented by an exponential function and a single-sided exponential convoluted with a detector lifetime resolution function models τ.

- **Double-sided fake J/ψ background**, where the di-muon invariant mass distribution is modeled by an exponential function for the mass part and a double-sided exponential for background convoluted with a detector lifetime resolution function.

The last two components model together the non-prompt J/ψ background contribution to the τ distribution.

The final probability distribution function is a sum of all components:

$$PDF(m, \tau) = \sum_{i=1}^{5} f_i(m) \cdot (h_i(\tau) \otimes r(\tau)),$$

where the corresponding τ model is convoluted with a lifetime resolution model function $r(\tau)$.

[1] The Crystal Ball function, named after the Crystal Ball Collaboration, where it was devised and first used [93].

The mass and pseudo-proper lifetime distributions components and their effective roles are shown in figure 6.1 and enumerated in table 6.1.

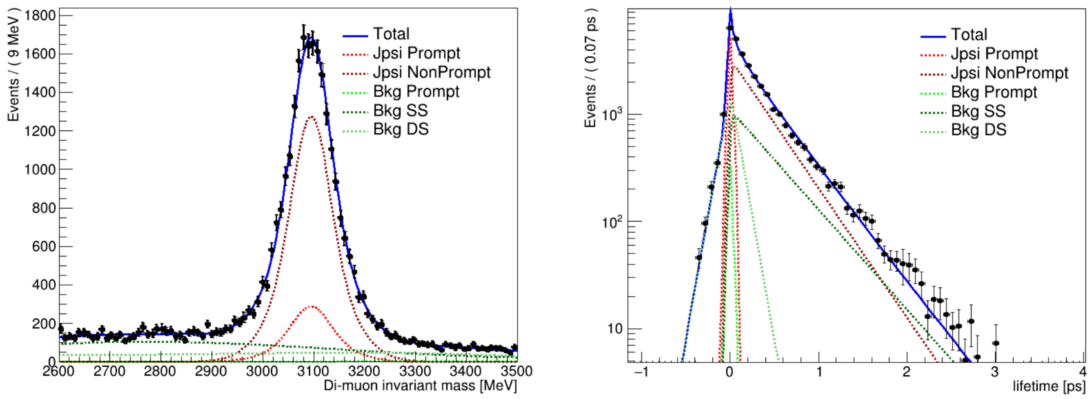

(a) J/ψ mass model **(b)** J/ψ lifetime model

Figure 6.1.: The sample invariant mass (a) and lifetime (b) parts of a J/ψ 2D model. Blue continuous curve represents a sum of all components. Red and pink components are the mass and lifetime models of prompt and non-prompt J/ψ respectively. The backgrounds models (green) are more discernible on the lifetime plot.

Component type	f_i(Mass term)	h_i(τ term)
Non-prompt J/ψ signal	$CB_1(m) \oplus G_1(m)$	$Exp_{J/\psi-SS_1}(\tau)$
Prompt J/ψ background	$CB_1(m) \oplus G_1(m)$	$\delta(\tau)$
Prompt fake J/ψ background	$P_3^{(0)}(m)$	$\delta(\tau)$
Single-sided fake J/ψ background	$Exp_5(m)$	$Exp_{Bkg-SS}(\tau)$
Double-sided fake J/ψ background	$P_4^{(1)}(m)$	$Exp_{Bkg-DS}(\|\tau\|)$

Table 6.1.: Breakdown of the component probability distribution functions (PDFs) that build the di-muon mass and lifetime simultaneous fit probability distribution function. The CB represents a Crystal Ball function, G is Gaussian, $P^{(n)}$ denotes a polynomial where n defines the order, Exp represents an exponential function and finally $\delta(\tau)$ is a Dirac delta function.

The resolution model, $r(\tau)$, is formed from two Gaussian terms, $r(\tau) = G_1(\tau) \oplus G_2(\tau)$. In all fit function components, the parameters of the lifetime detector resolution function are identical. For the prompt and non-prompt J/ψ, the parameters determining the position and shape of the J/ψ mass peak are the same. Overall, fit functions have 17 free parameters which can be varied during fitting.

The enumeration of parameters of invariant mass models $\boldsymbol{f_i}$

- **Prompt/Non-Prompt $\boldsymbol{J/\psi}$ Parameters**
  - $\boldsymbol{C_{G_1/CB_1}}$ **:** Crystal Ball function plus a Gaussian unit normalized fraction co-efficient. $f_{1/2}(m) = C_{G_1/CB_1} \cdot CB_1(m) + (1 - C_{G_1/CB_1}) \cdot G_1(m)$
  - $\boldsymbol{k_{\sigma_{G_1}/\sigma_{CB}}}$ **:** The scaling of the Gaussian standard deviation (σ_{G_1}) to the Crystal Ball standard deviation (σ_{CB_1}), such that the width of the Crystal Ball is defined as $\sigma_{CB_1} = \sigma_{G_1} \cdot k_{\sigma_{G1}/\sigma_{CB}}$
  - $\boldsymbol{\mu_{G_1}}$ **:** The mean of the Gaussian used to model the J/ψ candidate invariant mass peak.
  - $\boldsymbol{\sigma_{G_1}}$ **:** The standard deviation of the Gaussian model of the J/ψ candidate invariant mass peak.
- **Fake $\boldsymbol{J/\psi}$ Parameters**
  - $\boldsymbol{\lambda_5}$ **:** The exponential decay constant for the non-prompt fake J/ψ single-sided mass component pdf ($E_5(m)$).
  - $\boldsymbol{a_{SS}^{(1)}}$ **:** The first order co-efficient for the non-prompt double-sided fake J/ψ mass model. $P_4^{(1)}(m) = N_{DS}(a_{DS}^{(1)} x + 1)$.

The parameters of lifetime models $\boldsymbol{h_i(\tau)}$

- **Double Gaussian Resolution Parameters**
  - $\boldsymbol{C_{g_1(\tau)/g_2(\tau)}}$ **:** The unit normalized fraction relating the two Gaussians that make the resolution model $r(\tau) = C_{g_1(\tau)/g_2(\tau)} \cdot g_1(\tau) + (1 - C_{g_1(\tau)/g_2(\tau)}) \cdot g_2(\tau)$.
  - $\boldsymbol{\sigma_{g_1(\tau)}}$ **:** The standard deviation of the first Gaussian component used in lifetime resolution model.
  - $\boldsymbol{k_{\sigma_{g_1}/\sigma_{g_2}}}$: Scale factor relating the standard deviation of the first Gaussian ($\sigma_{g_1(\tau)}$) to the second in the lifetime resolution model. $\sigma_{g_2(\tau)} = k_{\sigma_{g_1}/\sigma_{g_2}} \cdot \sigma_{g_1(\tau)}$
- **$\boldsymbol{J/\psi}$ Parameters**
  - $\boldsymbol{\lambda_{J/\psi-SS}}$**:** Exponential decay constants of the single-sided exponential forming the non-prompt J/ψ lifetime model, $Exp_{J/\psi-SS}$.

- **Fake J/ψ Parameters**
  - $\boldsymbol{\lambda_{Bkg-SS}}$, $\boldsymbol{\lambda_{Bkg-DS}}$ **:** The exponential decay constants of the lifetime models for the fake J/ψ single sided ($Exp_{Bkg-SS}(\tau)$) and double sided ($Exp_{BkgDS}(|\tau|)$) backgrounds.

Furthermore, there are general normalization coefficients representing event count for each of the 5 model components in preceding equation. The model parameters $N_{J/\psi-Prompt}$, $N_{J/\psi-NonPrompt}$, $N_{Bkg-Prompt}$, $N_{J/\psi-SS}$, $N_{J/\psi-DS}$ are the number of prompt J/ψ, non-prompt J/ψ, prompt fake J/ψ, non-prompt fake J/ψ with single and double sided background.

6.1.2. Third muon template

In contrast to the J/ψ model, the third muon template model is not parameterized by analytic functions, but it is rather extracted from the MC and data. The role of this template is extraction of the yield of non-prompt third muons in events. It is implemented as two-dimensional maximum likelihood fit. There are two variables attributed to the third muon candidate. First is implemented as a fit to a boosted decision tree (BDT) output, which is trained to separate fake muons from true muons (backgrounds such as such as in-flight decays), and the second is d_0 significance of muon track which is employed for non-prompt muon yield extraction.

The third muon BDT and d_0 significance distributions are fitted simultaneously to determine the non-prompt real muon component. The fit is performed on a subset of the data passing the event selection, in a region with less backgrounds. The phase space cuts have been documented in the preceding sections but are summarized here. Events must be in the non-prompt J/ψ region ($\tau > 0.25$), the J/ψ candidate invariant mass must be within the J/ψ mass peak, $2.95 < m_{J/\psi} < 3.25$, and finally events must be in the signal Δz_0 region, $|\Delta z_0| < 40$ mm. The fit is an extended maximum log-likelihood fit, fitting data events using templates derived for each expected third muon component.

In principle and with regard to this analysis, the input dataset contains third muons which belong exclusively to a single category of the following:

- **Prompt muons** are true muons which are produced at the primary interaction vertex

- **Non-prompt muons** are true muons which are by definition the signal, and originate in semi-leptonic decays of B-hadrons or cascade decays such as $B \to D \to \mu + X$
- **Fake muons** are other particles reconstructed as muons, the bulk is represented by $K^{\pm}$ and $\pi^{\pm}$ particles reconstructed as muons, for description see discussion in section 6.1.4.

In addition the third muon could be produced in background events containing a fake J/ψ, see section 6.1.3, or pile-up events, where the J/ψ and third muon produced in different p-p interactions (see section 6.1.5). This results in a model of third muons composed of five individual components. Each of these are modeled by templates taken from either MC (non-prompt, prompt and fake muon) or data-driven techniques (fake J/ψ and pile-up) which are used to fit the data.

The following list details the five fitted third muon components as well as the source of the templates used for each.

- Prompt muon produced in a pp collision in a primary vertex. Template shapes of BDT output and d_0 are extracted from the PP MC. These muons are real and peak at the high values in the BDT output distribution. In addition, they have a narrow d_0 significance distribution since they are produced at the interaction point. The shape of the templates are fixed, but the normalization is let to float in the fit.
- Non-prompt signal muon, produced in a decay of B hadron. The BDT and d_0 significance templates are extracted from the BB mc sample. Reconstructed muons must match to a truth muon which has a B heritage. This component populates the BDT output region of real muons and it has a wide d_0 significance distribution, indicating production away from the primary vertex. Similarly as in the previous case, the shape of the templates is fixed but for the normalization which can float in the fit.
- Fake muons, mainly a $K^{\pm}$ or $\pi^{\pm}$ decaying at significant distance from the primary vertex into a muon and a neutrino. The fake muons are defined in the same way as for BDT training in section 4.3. For the sake of more accurate data description, the fake muon contribution is split into prompt and non-prompt components. In both cases the BDT template has a large contribution at low values. For the non-prompt fake muon component, the d_0 significance template is the same as in the case of

non-prompt muons. The prompt fake muon d_0 template is identical as the d_0 distribution for prompt muons.

- Fake J/ψ 3^{rd} muon templates are taken from J/ψ sidebands. This template is extracted from the 2012 data and is discussed in section 6.1.3.
- Pile-up background, muons at a considerable longitudinal distance to the J/ψ vertex. This template is extracted from 2012 data and is discussed in detail in section 6.1.5.

The templates are shown in figure 6.2.

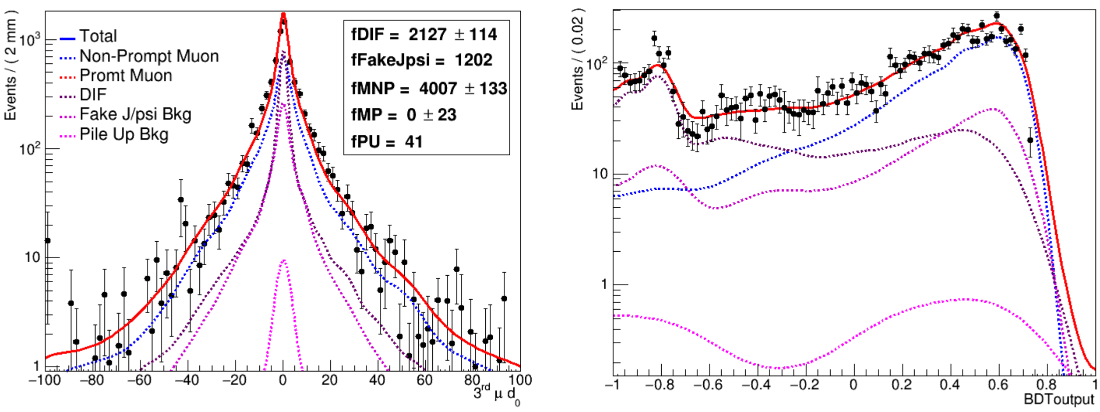

(a) 3^{rd} muon d_0 model **(b)** 3^{rd} muon BDT model

Figure 6.2.: 3^{rd} muon d_0 (a) and BDT (b) parts of a third muon 2D model. The red continuous curve represents a sum of all components. Non-prompt muons from B semileptonic decays are shown as blue dashed line, while the decays-in-flight are dark violet. Fake J/ψ background is taken from mass sidebands. This plot is taken from the fit in $\Delta\phi$ variables in the low $\Delta\phi$ region contaminated with decays-in-flight and is showing the discriminating power of BDT.

6.1.3. Fake J/ψ background

The background arising from the fake J/ψ events have the third muon not produced in association with a real J/ψ, so these events are removed in a two step process. First, a tighter window around the $J\psi$ candidate invariant mass peak is devised. The signal window was chosen to be 2.95-3.25 GeV. Then residual background events under the invariant mass peak are removed using a side-band subtraction method. The two sideband regions are defined to be $2.60 < m_{\mu^+\mu^-} < 2.95$ GeV and $3.25 < m_{\mu^+\mu^-} < 3.50$ GeV. Events falling within these sidebands are used for modeling fake J/ψs in the 2D J/ψ

mass-τ fit and also for templates of the BDT and d_0 significance distributions of third muons. The normalization of the templates is taken from the fit of a 2D J/ψ model, where the three fake J/ψ background models are integrated over the phase space used for the third muon fits ($2.95 < m_{\mu^+\mu^-} < 3.25$ GeV, with $\tau > 0.25$). Using this method, the fake J/ψ background is fully constrained so the templates representing fake J/ψ background are kept fixed when fitting the third muon distributions in data.

It is assumed that the three fake J/ψ background components have the same third muon BDT output and d_0 significance distributions. In order to verify this assumption, data in the upper and lower mass side-bands are compared. Due to the different di-muon mass parameterizations for each of the fake J/ψ backgrounds, the relative contribution of each is different in the two side-band regions. The BDT and d_0 significance distributions for each sideband are compatible as shown in figure 6.3 showing there is no di-muon τ dependence to the shape of the third muon fit variables in fake J/ψ events.

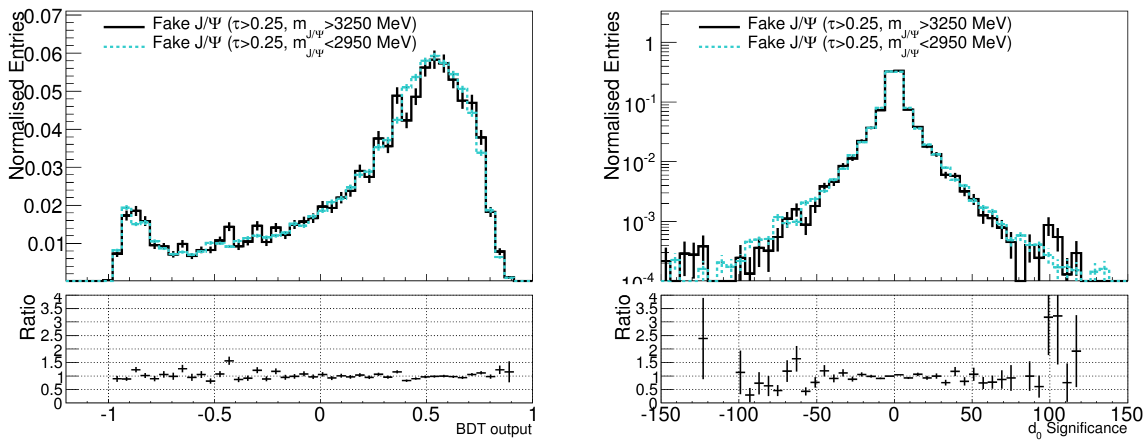

(a) a) **(b)** b)

Figure 6.3.: Unit normalized histograms of third muon fit variable distributions in high and low J/ψ mass side-bands for a) BDT output, b) d_0 significance.

The uncertainty on this background is assessed by changing the normalization of the fake J/ψ templates in the third muon fits by the uncertainty on the normalization of the single-sided fake J/ψ background. The single-sided component is the only background to contribute non-negligibly to the high τ region and as the third muon fit is performed inside the J/ψ mass window, only the uncertainty on the fraction of events in this region is taken from the 2D J/ψ fit. The fits are repeated with fake J/ψ template normalization altered by $\pm 1\sigma$ uncertainty on the normalization of the single-sided background.

Fake J/ψ candidates are treatable with the help of mass sidebands, assuming the di-muon composition is identical under the J/ψ peak and in the sidebands. The pile-up background is treatable with a cut on longitudinal difference between the z coordinate of the 3^{rd} muon perigee and the z-position of the fitted J/ψ vertex.

6.1.4. Fake muon background

The most challenging background in this analysis is decays in flight (DIF), a $K^\pm$ or $\pi^\pm$ decaying to a muon and a corresponding neutrino while traversing the detector. Usually the charged K/π leaves a track in the ID and daughter muon born in parent particle decay leaves a track in the MS. The small mass difference between$K^\pm/\pi^\pm$ and $\mu^\pm$ results in a small angular deflection of the muon so it continues in the direction of the hadron. The muon reconstruction algorithms then combine the resultant tracks and form a muon candidate. Decays such as $B \to J/\psi + K^\pm + X$ with $K^\pm$ reconstructed as a muon result in a background which is concentrated in the low $\Delta\phi$ region where the signal of gluon splitting class of QCD processes occurs. This is a region of considerable interest so it is crucial to have an accurate identification of DIFs so they do not interfere with the $b\bar{b}$ cross section measurement.

Another important background relevant to this analysis are fake muons from leakage of charged hadrons into the MS. Charged hadrons leave a perfect track in the ID and they shower in the HCAL, with some charged shower particles penetrating to the MS. Such events can be combined into a muon candidate track. Unfortunately, this background has the same characteristics as DIF.

The BDT used for fake muon identification along with variables used for fake muon discrimination is discussed in section 4.3

The third fake muon category is named punch-through for historical reasons, more appropriate name would be tunneling. It is defined as a $K^\pm$, $\pi^\pm$ or proton with sufficient p_T which traverses the detector to the MS without decaying or interacting hadronically with the material. This background appears on the detector level same as true muons, since it has a well-defined track in the ID and a track in the MS which matches well to the ID track. The punch-through estimate is taken from the MC simulation, where a reconstructed muon has no match in the truth muon collection, but it is matched to a $K^\pm$ or $\pi^\pm$, which has no decay or interaction vertex within the ATLAS detector volume. The distribution of punch-through is similar to the DIFs as it is originating from $K^\pm/\pi^\pm$.

The only difference with regard to the standard DIF being that punch-trough hadrons have a higher contribution in the detector regions with less material to traverse in the particle flight path. The ratio of the number of punch-through to standard fake muons is extracted from simulation and it is $\approx 1\%$. This value is used in the normalization of the background in the number of fake muons fitted in data. The correction for the third muon yield is devised for each differential bin by removing the expected number of punch-through events.

6.1.5. Pile-up background

The multiple proton interactions during bunch crossings create muons, which are uncorrelated background in this analysis. The number of pile-up interactions in the data and the model used in MC12b MC samples is shown in figure 6.4 .

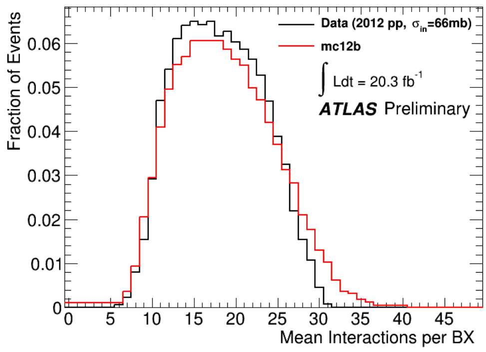

Figure 6.4.: Luminosity weighted distribution of the mean number of interactions per crossing used in the MC12b Monte Carlo production campaign. The distribution has been generated at the end of the 2012 *pp* data taking, based on the observed data distribution. Enough statistics has been generated on the tails of the distribution to take into account systematic uncertainties of the measurement of the luminosity and rescaling factors. It is superimposed on the luminosity distribution observed in the 2012 *pp* good quality data averaged over all BCIDs. The data luminosity distribution has been converted to the mean number of interactions per beam crossing using an inelastic cross section of 66 mb. This value was found to give the best Monte Carlo description of luminosity sensitive quantities in data such as the vertex multiplicity distribution. [94]

In order to handle this background, the most useful handle is the difference in the reconstructed track z_0 position, Δz_0 defined as:

$$\Delta z_0 = z_0^{\mu_{J/\psi}} - z_0^{3^{rd}\mu},$$

where $z_0^{\mu_{J/\psi}}$ is the z_0 track parameter at the point of closest approach to the beam axis of a J/ψ candidate muon and $z_0^{3^{rd}\mu}$ is the z_0 parameter taken from the track of the third muon at the point of its closest approach to the beam axis. The are two Δz_0 combinations and the maximal Δz_0 is selected on an event by event basis.

In order to remove significant part of the pile-up events, a hard cut is placed at $|\Delta z_0| < 40$ mm. Only the events passing this cut are used in following steps for fitting of the third muon distributions.

The numerical value for Δz_0 cut was decided with the help of a Pythia simulation. The normalized distribution for signal events is shown in figure 6.5, which justifies the selected cut value.

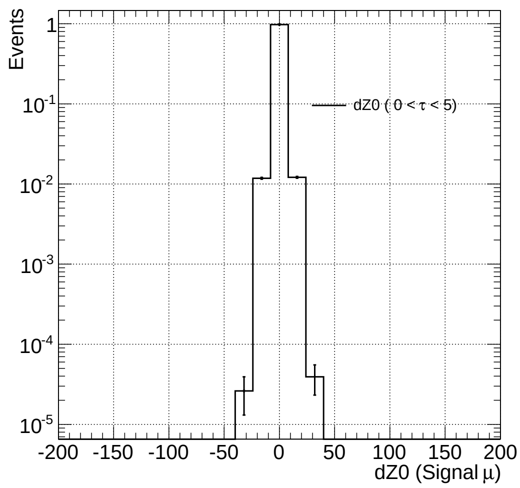

Figure 6.5.: Δz_0 distribution of signal events taken from the BB signal event simulation.

The situation in the 2012 ATLAS *pp* data is illustrated in figure 6.6, where the Δz_0 distribution is shown after all event selection cuts. The two components of compound distribution are obvious. A narrow peaked structure centered at zero Δz_0 represents events where the J/ψ candidate and third muon are produced in the same *pp* primary vertex and a wide Gaussian distributed pileup background spanning a significant Δz_0 range.

The residual pile-up background present within the $|\Delta z_0| < 40$ mm is removed using a side-band subtraction method. First, events which satisfy $|\Delta z_0| > 40$ mm are fit with a Gaussian model. Then the normalization of the fitted Gaussian within the area of the $|\Delta z_0| < 40$ mm cut gives the estimate of residual pile-up events in the signal region. With the event count normalization from under the signal peak and the Gaussian shape from outside the signal peak, third muon distributions for pile-up events are fully constrained. Figure 6.6 shows the Gaussian fit to the Δz_0 distribution for the pile-up events in ATLAS 2012 dataset.

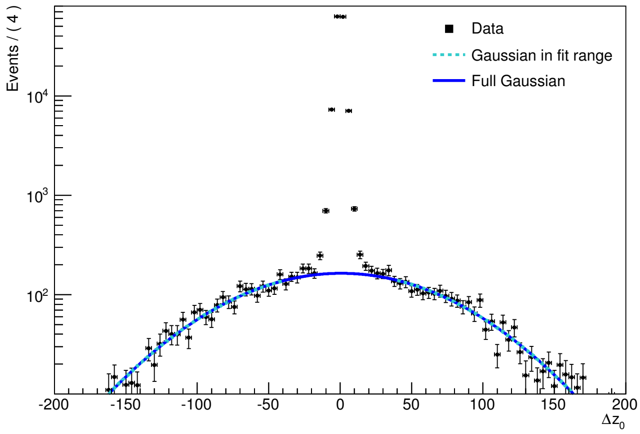

Figure 6.6.: Data Δz_0 distribution for the inclusive dataset including the Gaussian pile-up background fit.

.

The pile-up distribution templates for the third muon distributions are extracted from the pure pile-up region outside of the cut. The uncertainty on the fraction of pile-up events in the third muon fit templates is evaluated by modifying the pile-up normalization within Gaussian fit uncertainty, and it is applied as a $\pm 1\sigma$ variation to nominal pile-up templates.

6.1.6. B_c-meson background

An additional source of important irreducible background are B_c mesons, more specifically the decay of a B_c meson into $B_c \to J/\psi + \mu + X$. This process mimicks the signal of gluon-splitting class of processes, because the $J/\psi + \mu$ are distributed predominantly at the low range of values of $\Delta R(J/\psi, \mu)$. However, due to the low B_c production cross section and branching ratio of $B_c \to J/\psi + \mu + X$, the B_c background is expected to be small. Studies show the production fraction in hadronisation $\frac{\sigma(B_c^+)}{\sigma(\bar{b})} = (2.08^{+1.06}_{-0.95}) \times 10^{-3}$ [95] and the branching fraction $\mathrm{BR}(b \to B_c) \cdot \mathrm{BR}(B_c \to J/\psi + l + X = (5.2^{+2.4}_{-2.2}) \times 10^{-5}$, where l represents any lepton [6].

Due to the statistical limitations of B_c events, the $B_c \to J/\psi\mu + X$ background is taken directly from the MC. In order to reduce dependence of B_c modelling in Pythia, additional sample was generated in Herwig++. The predictions from both generators were averaged and subtracted from the fitted signal yield to remove the B_c background. The derived B_c predictions used for each differential bin are included in Appendix A.3. The template is normalized to the fitted number of $BB \to J/\psi\mu + X$ events.

Figure 6.7 shows the $\Delta R(J/\psi, \mu)$ and third muon p_T distributions as examples. In most distributions, the B_c events are comparable to BB events, but in ΔR there is an obvious difference.

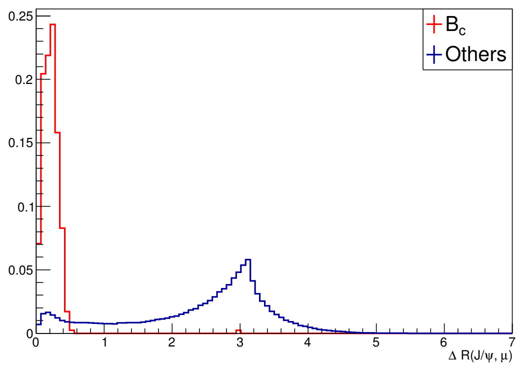

(a) a)

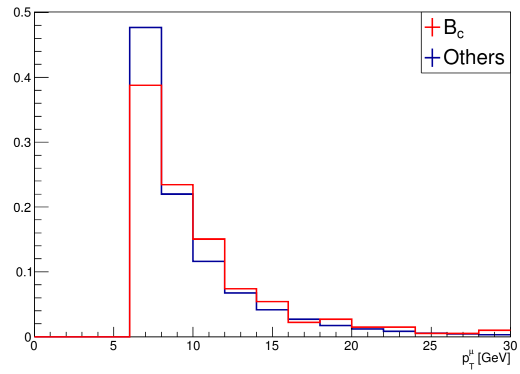

(b) b)

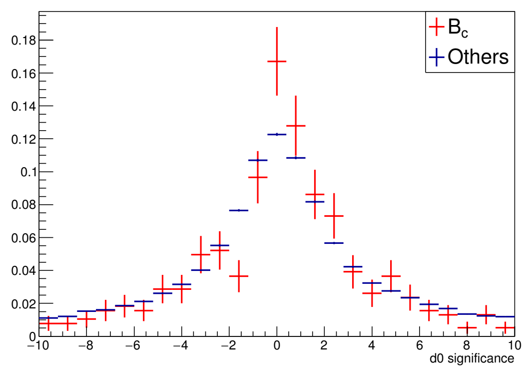

(c) c)

Figure 6.7.: Comparing $B_c \to J/\psi\mu + X$ events to $BB \to J/\psi\mu + X$. All plots are unit normalised. (a) shows the distribution of $\Delta R(J/\psi, \mu)$, (b) the distribution of third muon p_T and (c) the distribution of d_0 significance.

6.1.7. $B+D$-hadron background

Another important source of muons in this analysis are D mesons, which contain a charm-type quark and can decay semileptonically via emission of a virtual W boson. Even when produced promptly at pripary pp vertex, their relatively long lifetime translates into a relatively-large flight distance before decaying, with $c\tau$ ranging from 122.9 μm in the D^0 case to 311.8 μm in the case of $D^\pm$. This fact complicates the signal muon identification, because it is difficult to experimentally distinguish third muons from D and B-hadron decays, as both will have a wider d_0 significance distribution indicating production away from the beam line.

In general, there are four categories of charm (and consequent D meson) sources in $b\bar{b}$ events:

- Production in B-meson decays, where $b \to c + W^*$
- Production in multiple proton interactions (pile-up)
- Production in multi-parton interactions/double parton scattering
- Production during parton shower (gluon splitting) and $b\bar{b}$ hadronization.

The first category comprises B meson decays into a D meson. It proceeds via decay of a b quark into a c-type quark. It is considered signal because it still carries information of the original B meson.

The D mesons produced in pile-up proton collisions are not correlated to the J/ψ, and are flat in $\Delta\phi(J/\psi, \mu)$ distribution and will be removed through the pile-up removal procedure outlined in section 6.1.5.

In the third category, muons from multi-parton interactions are considered. As the cross sections of charm production is large compared to the beauty $\frac{\sigma_{b\bar{b}}}{\sigma_{c\bar{c}}} \approx \frac{1}{20}$, the contribution of the double parton scattering and production of $b\bar{b}c\bar{c}+X$ events in a single pp interaction is possible. They are semi-hard processes ($\mathrm{m}_q \gg \lambda_{\mathrm{QCD}}$) and theoretical calculations are available, but suffer from large uncertainties. Detailed modeling differs between MC generators. Even though the current interleaved evolution MPI model employed by Pythia8 includes limited re-scattering, it provides decent description of most data.

The fourth category includes events where a $c\bar{c}$ pair emerges in a $b\bar{b}$ hard scatter event either in the parton shower via gluon splitting ($g \to c\bar{c}$), or it is created during the hadronization. However, during hadronization, the flavor composition of the created $q\bar{q}$ pair is assumed to derive from a quantum mechanical tunneling process, which in turn implies a suppression of heavy quark production $u : d : s : c \approx 1 : 1 : 0.3 : 10^{-11}$ such that charm and bottom production can be neglected in the hadronization step.

In Pythia MC studies, it was found that $\approx 5\%$ of 3^{rd} muons passing selection are originating in decays of D mesons which do not have a B meson in their lineage. Since it is experimentally difficult to distinguish muons from the decay of D mesons compared to muons from the decay of B mesons, we cannot remove any D meson sources of third muon in data.

A MC correction removes the expected B+D-hadron contribution from the fitted number of signal events. The correction is derived from an average estimate of this background taken from the Pythia and Herwig++ MC samples. Figure 6.8 shows the distribution of B+D-hadron and B+B hadron events passing the event selection for two of the kinematic distributions in the Pythia. $J/\psi + \mu$ events from $B + D$ hadrons have different correlations between the J/ψ and third muon compared to double-B hadron events, so the B+D event background is determined separately for each differential observable bin. The $B + D$ contribution is removed from the signal yield after the third muon fits by subtracting the fraction of B+D events compared to B+B events using the average MC prediction. The derived $B + D$ predictions used for each differential bin are included in Appendix A.4.

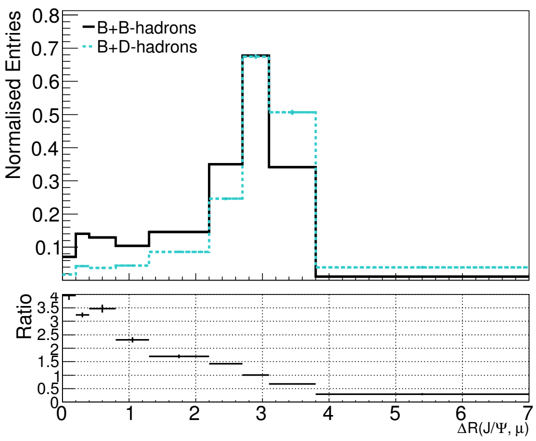

(a) $\Delta R(J/\psi, \mu)$

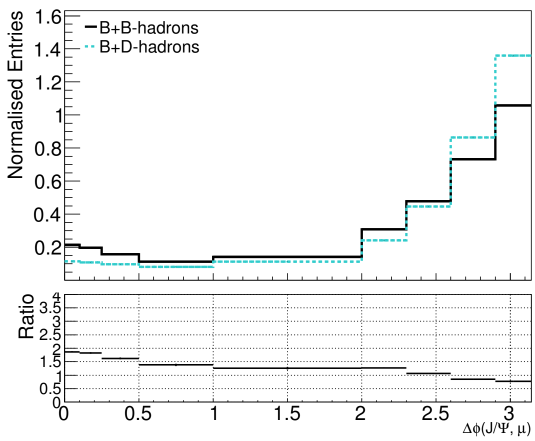

(b) $\Delta\phi(J/\psi, \mu)$

Figure 6.8.: Unit normalized ΔR and $\Delta\phi$ muon level distributions comparing MC events from two B-hadrons to events with a B and D hadron.

6.2. Fit procedure

The fit is executed in bins of the $J/\psi + \mu$ observables listed in table 4.1. The non-prompt, fake muon, fake J/ψ and pile-up templates are derived in the same observable bin as fitted to in data.

For the implementation of models and fitting, the RooFit [96] package is used. The MC ntuples used as input to this analysis are created from the AOD files from the reconstructed physics objects. The data ntuples are provided by the B-physics group.The actual fitting procedure consists of two steps, with first being the J/ψ mass and pseudo-proper lifetime model fit. Then, with the non-prompt J/ψ contribution fully determined, another 2D maximum likelihood fit is done using variables assigned to the third muon with focus on extraction of the yield of non-prompt third muons in events.

6.2.1. J/ψ mass and lifetime fit

Figure 6.9 shows the sample result of the 2D fits to the data taken from three observables in random bins. All of the differential 2D fits are shown in appendix A.1.

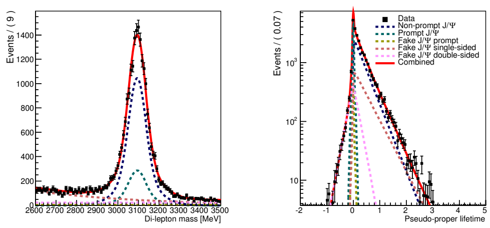

(a) $0.25 < \Delta\phi < 0.5$

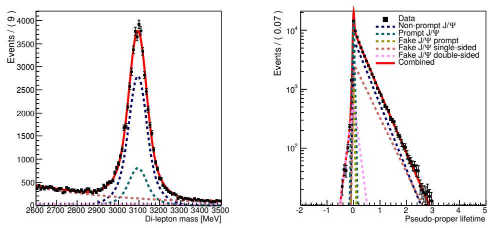

(b) $15 < p_T < 20$ GeV

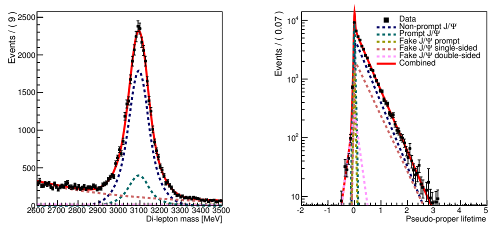

(c) $35 < M(J/\psi + \mu) < 50$ GeV

Figure 6.9.: Example of J/ψ fit results for sample bins of $\Delta\phi$, p_T and $M(J/\psi + \mu)$.

The robustness of the J/ψ fit performance was tested by the Monte Carlo closure test. A number of toy datasets, each with 20000 events were produced. Each toy dataset combined random amounts of non-prompt and prompt J/ψ extracted from $pp \to J/\psi + X$ and $pp \to BB \to J/\psi + X$ datasets. Events used in creation of toy datasets have passed the standard data selection. Then the 2D J/ψ mass-lifetime model is fit to each toy dataset, and the fraction of prompt and non-prompt J/ψ is extracted from the fit. The fraction is then directly compared to the known fractional composition of the toy dataset.

Figure 6.10 shows the fractional difference between the true and fitted number of prompt and non-prompt J/ψs used in its creation. It can be seen that the fit model is performing well with deviations from the true composition consistently below 2%.

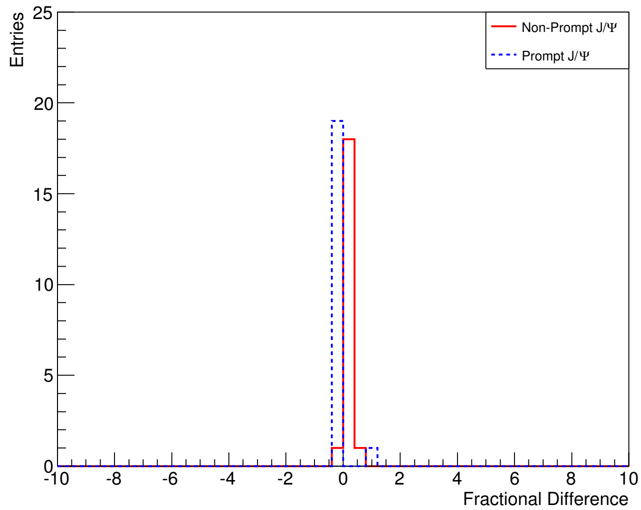

Figure 6.10.: Fractional difference (%) of the number of fitted J/ψ components, both prompt and non-prompt, when compared to the known fraction from MC.

.

6.2.2. 3^{rd} muon d_0 and BDT fit

The 3^{rd} muon BDT and d_0 significance distributions are fit simultaneously to determine the nonprompt muon component. The fit is carried out on a subset of the data passing the standard event selection. In addition, events must be in the non-prompt J/ψ region $\tau > 0.25$ and in the signal Δz_0 region defined as $|\Delta z_0| < 40$ mm. The fit is an extended maximum log-likelihood fit, fitting data events using templates derived for each expected third muon component, defined in section 6.1.2.

Figure 6.11 shows the result of the 3^{rd} muon fits to the data for a bin taken from three of the differential variables as defined in table 4.1. The differential fits for all the other differential bins can be found in appendix A.1.

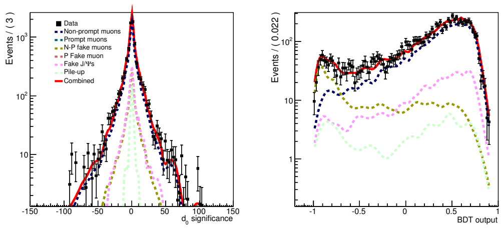

(a) 0.25 $<\Delta\phi<$0.5

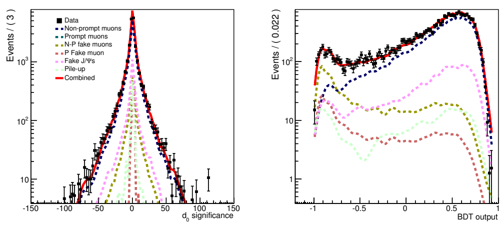

(b) 15 $<p_T<$20 GeV

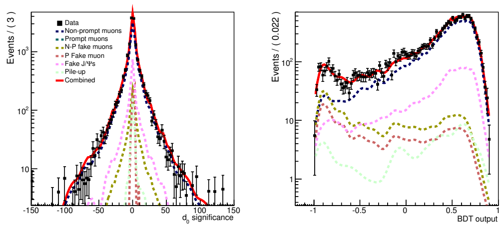

(c) 35 $<M(J/\psi+\mu)<$50 GeV

Figure 6.11.: Example of third muon fit results for sample bins of $\Delta\phi$, p_T and $M(J/\psi+\mu)$.

3^{rd} muon d_0 fit robustness test

Similarly as in the J/ψ invariant mass and pseudo-proper lifetime fit, another MC closure test was implemented for the stability and robustness of the third muon d_0 significance fit. Toy datasets of 20000 events were produced by combining random amounts of events with expected non-prompt third muons and events with expected prompt third muons. The non-prompt third muon contribution comes from events in the Pythia $BB\to J/\psi+X$ MC, where the third muon contribution is dominated by muons from decay of a B-hadron. The prompt third muon contribution comes from events in the Pythia $pp\to J/\psi$ sample, where the third muon composition is mostly prompt muons candidates. Both samples are required to pass the data selection cuts, as outlined in chapter 5, before sampling. A 1D maximum likelihood fit of the d_0 significance distribution was performed on the third muons in the toy datasets. The normal fitting procedure was performed using the same MC templates used in the data analysis to model the prompt and non-prompt d_0 significance templates. The fake J/ψ and pile-up backgrounds were removed using the usual procedure; however, fake muon background was set to zero for the fits. The numbers of fitted third muons are compared to fractions of the non-prompt and prompt MC sources used in the toy dataset construction. Figure 6.12 shows the fractional difference for both the prompt and non-prompt third muon components compared to the true number. It can be seen that the model is performing well with only small deviations for the prompt distribution.

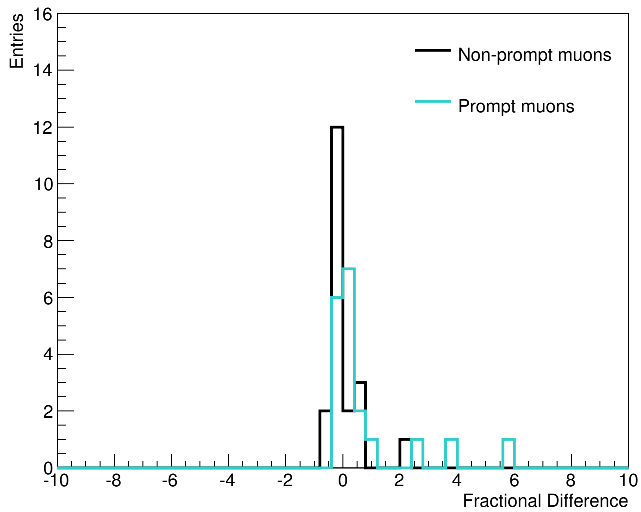

Figure 6.12.: Fractional difference of the number of fitted muon components, both prompt and non-prompt, when compared to true fraction

3^{rd} muon BDT fit robustness test

The fake muon component peaks in the region of most interest to this analysis, so it is important that the amount of fake muons is accurately modeled in the third muon fits. Two qualitative cross checks on the modeling of the fake muon component were defined by looking at independent orthogonal data control regions expected to contain more fake muons. The first control region is defined by reversing the pile up cut, so looking at events with $|\Delta z_0| > 40$ mm. This means the J/ψ candidate and third muon have been created in separate pp collisions and as QCD interactions dominates at a hadron collider, the probability of $K^\pm/\pi^\pm$ faking a third muon increases in this region. The second control region is defined by looking at prompt di-muon events, which is realized by reversing of the pseudo-proper lifetime cut to $\tau < 0.25$ In this region, prompt J/ψ production is from the QCD processes, which increases the probability of $K^\pm/\pi^\pm$ faking a third muon. The fits in these control regions were performed inclusively as statistics did not allow for a splitting into differential bins. The third muon fit procedure was the same as the usual, with the exception of no pile-up template used in the pile-up control region. The result of these fits can be seen in figure 6.13, while table 6.2 details the amount of fake muons (both prompt and non-prompt) fitted in the two control regions as well as the main inclusive fit. It can be seen, that in both control regions the fit is behaving as expected and fitting a higher fraction of fake muons..

Fit Region	Fake muons %	Non-prompt %	Prompt %
Standard	13	87	0
Pile-up	48	33	19
Prompt	24	76	0

Table 6.2.: Components of third muon fits in nominal and fake muon control regions. The amount of each variable third muon component is listed as a percentage of the total number of fitted floating components, excluding the pile-u p and fake J/ψ contributions.

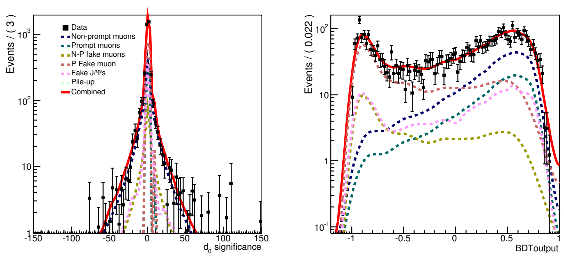

(a) nominal fit

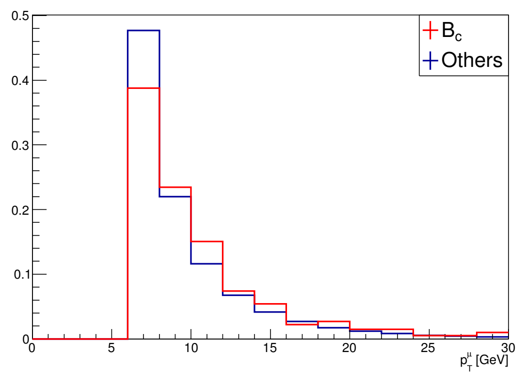

(b) fit in pile-up region

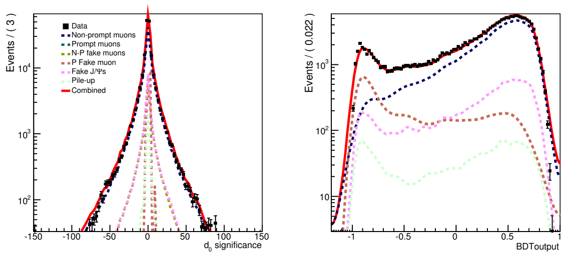

(c) fit in prompt region

Figure 6.13.: Inclusive 2D third muon fit result, for the nominal fit, fit in pile-up region and fit in prompt region.

6.2.3. Extrapolation to full τ region

To account for the signal events below the J/ψ $\tau < 0.25$ cut, the number of fitted non-prompt third muons needs to be extrapolated over the full pseudo-proper lifetime range of the J/ψ. The assumption used is that the composition of third muons is unchanging in τ for a non prompt J/ψ, i.e. for an event with a non-prompt J/ψ the probability of the third muon being from a B-hadron is independent of τ. This was confirmed in data by looking at inclusive fits in different τ-slices and looking at how the fitted third muon composition changes. Figure 6.14 shows for bins of J/ψ pseudo-proper lifetime, the ratio of fitted number of non-prompt J/ψ's to fitted number of third muons types, for each of the three floating third muon components, non-prompt, prompt and fake muon. It shows that above the lifetime cut used in the analysis ($\tau > 0.25$), the third muon composition with respect to non-prompt J/ψ's is constant as a function of τ. Below values of $\tau < 0.1$, deviation from flatness is observed. This region has a much larger background contamination for both the J/ψ and the third muon fits. Non-prompt J/ψ events are no longer the dominant contribution for the di-muon fits, with lager contributions from prompt J/ψ's and fake J/ψ's. The reduced number of non-prompt J/ψ's in the low τ region explains the deviation in figure 6.14, as the di-muon background events can also contain non-prompt third muons, changing the ratio of fitted non-prompt J/ψ's to non-prompt muons.

As a cross check, the τ dependence of the third muon composition has also been checked in MC. For events containing a J/ψ, which comes from a B-hadron decay, the fraction of non-prompt muons and fraction of fake muons is plotted as a function of τ in figure 6.15. The non-prompt third muon composition was found to be extremely consistent over the whole range including below $\tau = 0.1$ which validates the extrapolation assumption.

The extrapolation to the full τ-spectrum is then performed by simply correcting the third muon yield found in the $\tau > 0.25$ region by an extrapolation factor taken as the ratio of all non-prompt J/ψ's over the full τ range to the number of J/ψ's found above the $\tau > 0.25$ cut. This correction is taken from the 2D J/ψ fit results and accounts for all of the non-prompt J/ψ events below the $\tau < 0.25$ cut. The correction is derived individually for each differential observable bin.

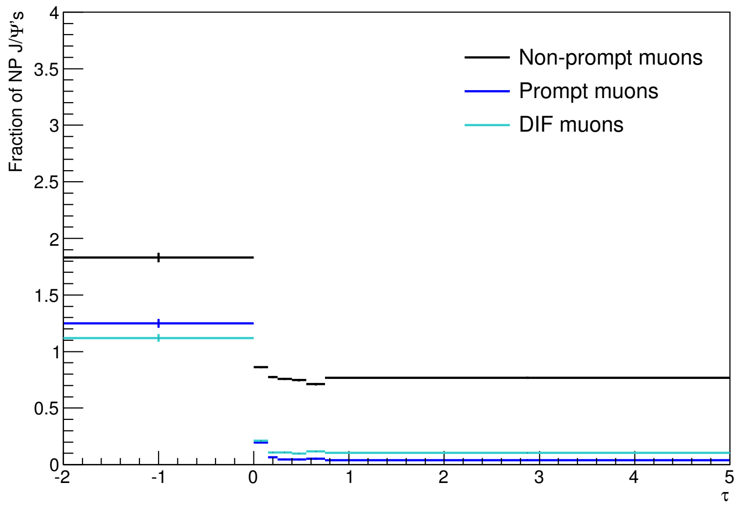

Figure 6.14.: In bins of J/ψ lifetime, the ratio of numbers of non-prompt J/ψ's to number of third muons determined from fits to data, for each of the three floating third muon components, non-prompt, prompt and fakes.

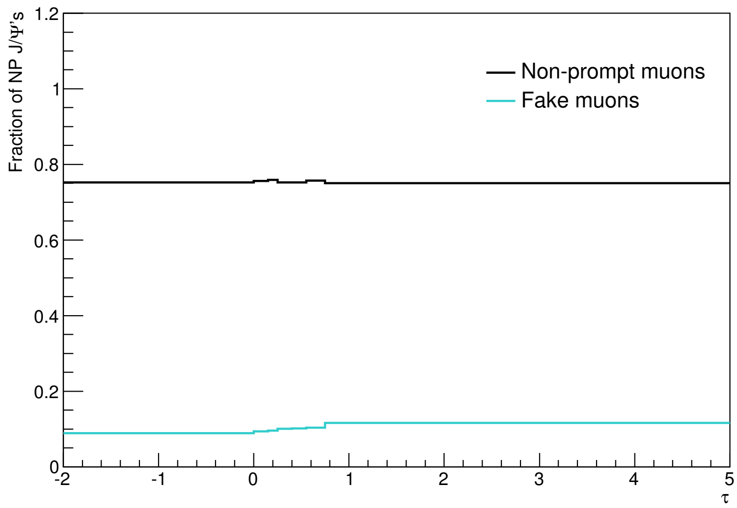

Figure 6.15.: In bins of J/ψ lifetime, the ratio of numbers of non-prompt J/ψ's to number of third muons determined from MC, for non-prompt and fakes muons.

6.2.4. Propagation of statistical uncertainty

The statistical uncertainty on the number of signal events, and therefore the cross section, comes from two sources. Firstly, the uncertainty on the number of fitted non-prompt third muons.

Secondly, a source of statistical uncertainty from the $\tau < 0.25$ cut on the dataset for the third muon fits is included, as this limits the number of events going into the third muon fit. This is derived from the fitted uncertainty on the slope parameter (i.e. the exponent of exponential function) of the non-prompt J/ψ lifetime component. The slope parameter was found to be uncorrelated with any of the other J/ψ model parameters and is solely responsible for how many non-prompt J/ψ's populate the high τ region. The number of non-prompt J/ψ's above the lifetime cut was varied by changing the slope parameter by $\pm 1\sigma$ uncertainty from the non-prompt J/ψ model, with the error taken from the 2D J/ψ fit. The extrapolation factor, described in section 6.2.3, is recalculated for the varied non-prompt J/ψ model with the largest difference from either the plus or minus variation, as compared to the default extrapolation factor taken as the error. This error estimate is then combined with the third muon fit uncertainty on the number of non-prompt third muons to define the total statistical uncertainty on the number of signal events.

6.3. Unfolding

The data are already corrected for trigger and reconstruction efficiencies through the application of event weights. However, the distributions must still be corrected for the effects of detector resolution on the p_T and η of the muons. These effects can be split into two components:

- Events that pass both particle level and detector level selections may be reconstructed in different bins of the differential cross sections.
- Events may pass the particle level selection, but fail the detector level selection, or vice versa. This can be due to migrations across the 6 GeV p_T cut, or the muon η cuts, and as a result, the measured events in data may not correspond to the full fiducial particle level selection.

These effects must be unfolded to correct the detector level measurement to a full particle level cross section.

6.3.1. Bin-to-bin migrations

First, we consider the effects due to migrations between bins. This is studied using the Pythia signal MC, by applying the particle level and detector level event selection (as defined in section 5.2.2 and 5.1, though without a trigger requirement on the detector level), and matching all reconstructed muons to a truth muon within $\Delta R < 0.03$. Migration matrices are then formed by plotting measured quantities at particle level vs the measured quantities at detector level for each event. Figure 6.16 shows these migration matrices for all observables defined in table 4.1, where matrices are normalised in a such way that the sum of values in a row adds up to 1. It can be seen that these matrices are highly diagonal, and therefore bin migrations effects are very small. This makes sense when comparing the bin widths to the detector resolution on p_T and η. As a result, we do not use one of the advanced unfolding techniques to correct these effects. Instead, a simple bin-by-bin correction is applied, which is combined with the correction for the other effect in the list: migrations in and out of the fiducial volume.

6.3.2. Fiducial correction

To study migrations in and out of the fiducial volume, the same Pythia signal MC sample is used, and it is necessary to loosen the event selection. Particle level events are first selected by applying the full particle level selection. These events are required to also pass full detector level selection, but with looser cuts: $p_T > 4$ GeV and $|\eta| < 3$. Therefore, we keep the events which pass the particle level selection, but fall just outside the standard detector level selection. In these events, the same matching of $\Delta R < 0.03$ between particle and reconstructed muons is applied to reject events containing background muons at the detector level. For these events, the particle level cross sections are plotted.

This process is then repeated for the detector level: applying the full detector level selection, and matching the reconstructed muons to particle level muons which pass the full particle level selection, but with looser cuts, $p_T > 4$ GeV and $|\eta| < 3$. For these events, the detector level cross sections are plotted.

To derive the unfolding correction, the ratio of these two distributions is taken. This accounts both for migrations in and out of the fiducial volume, and migrations between bins within the distributions themselves. This ratio of (detector level) / (particle level) is shown in figure 6.17 for all observables considered in this analysis, and are typically at the %-level. Uncertainties shown on the distributions are calculated from statistical uncertainties of numerator and denominator, which is an overestimate of the true statistical uncertainty as it neglects the (large) statistical correlation between the numerator and denominator. However, this uncertainty is kept for now, as it is negligible in the final result. The inverse of these ratios is then applied to the data to fully correct from detector level quantities to particle level quantities.

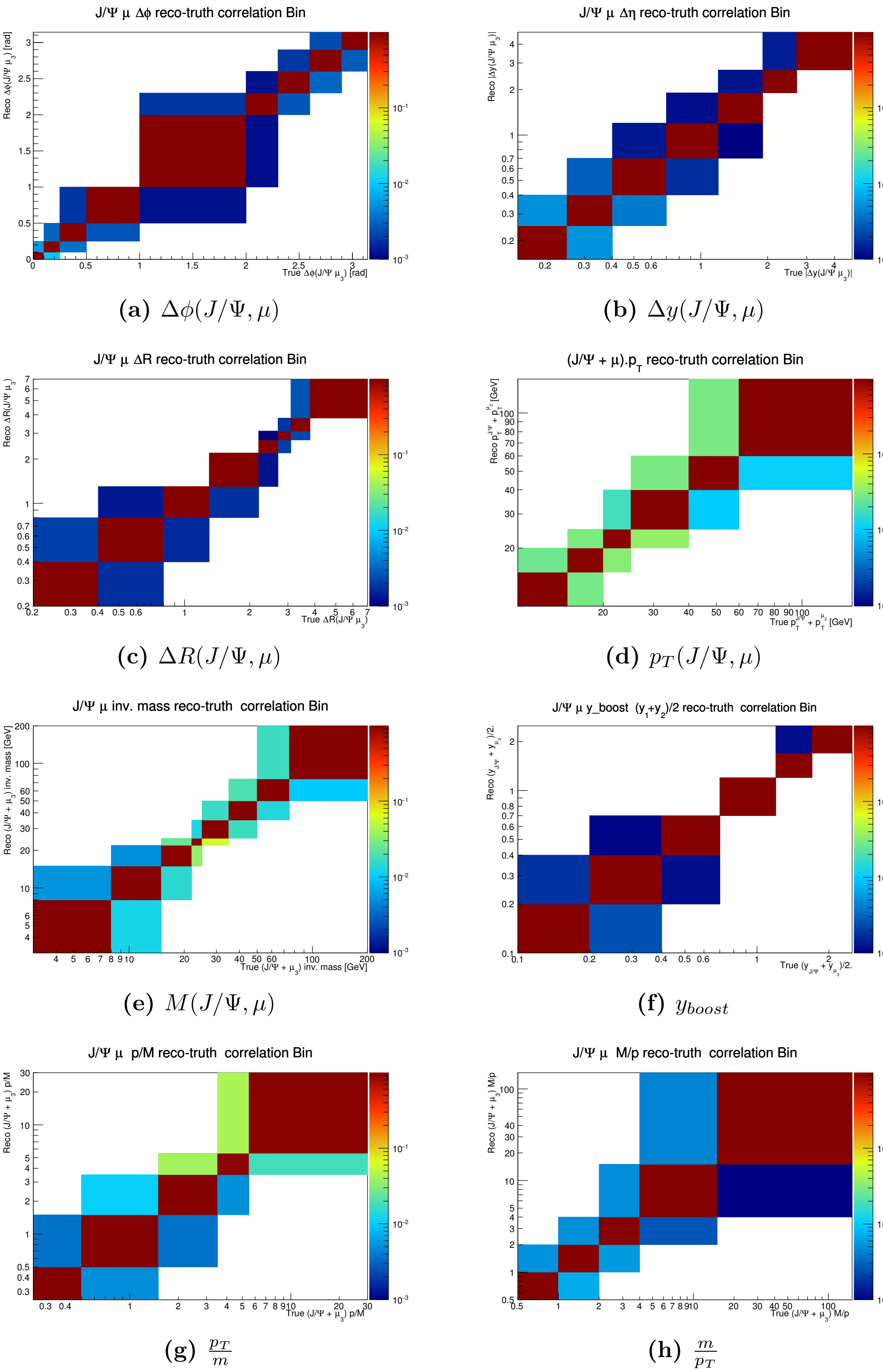

(a) $\Delta\phi(J/\Psi, \mu)$ **(b)** $\Delta y(J/\Psi, \mu)$

(c) $\Delta R(J/\Psi, \mu)$ **(d)** $p_T(J/\Psi, \mu)$

(e) $M(J/\Psi, \mu)$ **(f)** y_{boost}

(g) $\frac{p_T}{m}$ **(h)** $\frac{m}{p_T}$

Figure 6.16.: The bin migration matrix for all observables. Plots are formed by plotting measured quantities at particle level vs. the measured quantities at detector level.

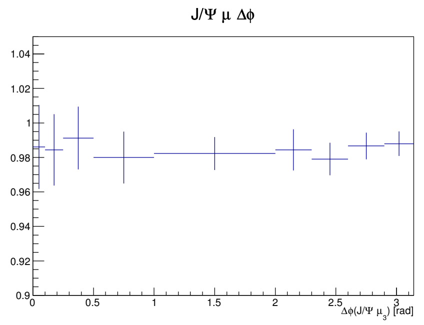

(a) $\Delta\phi(J/\Psi, \mu)$

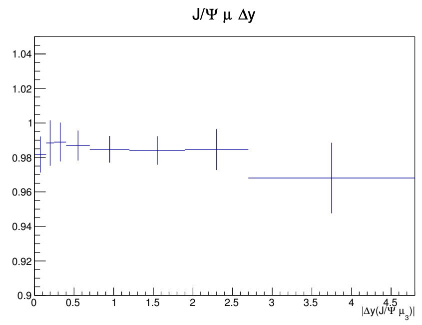

(b) $\Delta y(J/\Psi, \mu)$

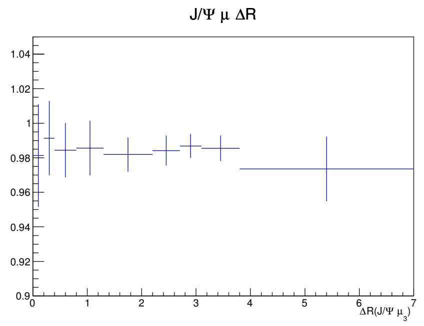

(c) $\Delta R(J/\Psi, \mu)$

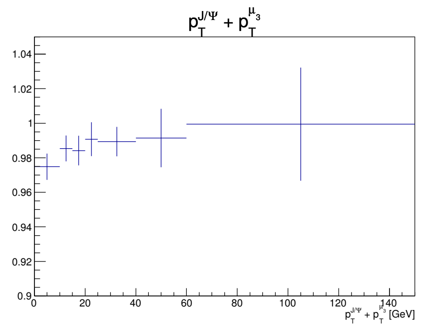

(d) $p_T(J/\Psi, \mu)$

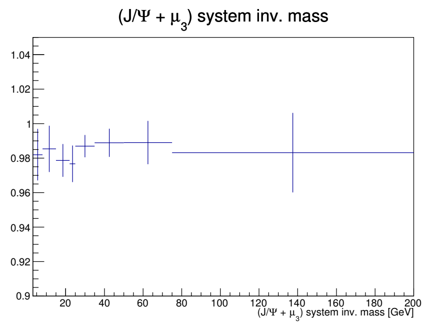

(e) $M(J/\Psi, \mu)$

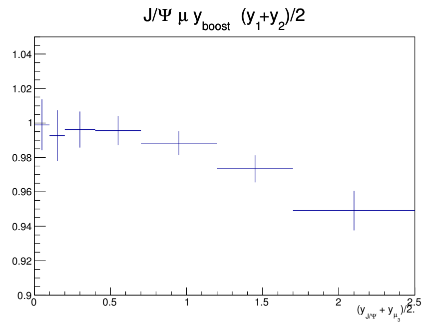

(f) y_{boost}

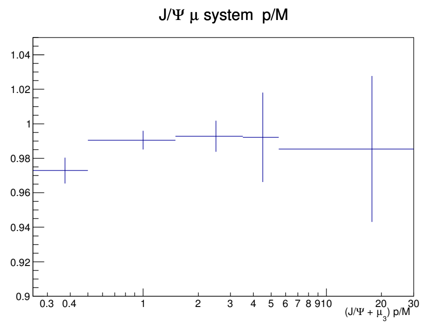

(g) $\frac{p_T}{m}$

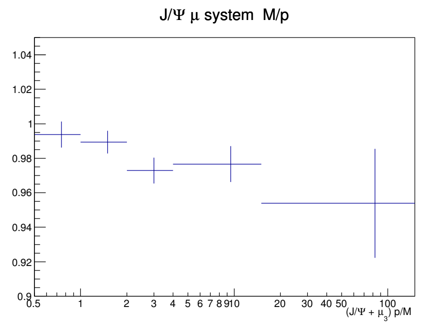

(h) $\frac{m}{p_T}$

Figure 6.17.: The fiducial volume correction for all observables. It accounts both for migrations in and out of the fiducial volume, and migrations between bins within the distributions themselves. The ratio of (detector level) / (particle level) event selection is shown.

Chapter 7.

Analysis results

In this chapter, preliminary measurement results are presented. At the time of writing of this thesis, the analysis note [80] is in its final approval stage, and when approved, it will be submitted for publication.

7.1. Results of the $J/\psi + \mu$ fit

Measurements of BB production via the $J/\psi + \mu$ proxy are presented as differential cross sections parameterized in the difference in azimuthal angle $\Delta\phi$, difference in rapidities Δy and ΔR distance between the J/ψ and μ. The results are also calculated for average rapidity y_{boost}, mass and transverse momentum of the $J/\psi + \mu$ system as well as for their ratios $\frac{p_T}{m}$ and $\frac{m}{p_T}$.

The measurements are compared with the theoretical predictions obtained with various MC event generator programs, based on LO and NLO perturbative QCD calculations.

Figures 7.1-7.8 show the cross section plots for data for each of the differential variables. The cross section is shown at the $J/\psi + \mu$ level; it has not yet been unfolded to the B hadron level. Information on corrections to the B hadron level cross section are included in note [80] as an appendix. Both Pythia and Herwig++ predictions are in principle LO generators, and therefore they are not expected to correctly estimate the normalization. The predictions have been scaled to data in a way that the normalization is matched in the high $\Delta R(J/\psi, \mu) > 3$ region, where they are expected to be most accurate because of the dominance of the LO flavor creation process. The data points show both the statistical error as well as the combined statistical and systematic error, where they have been added in quadrature.

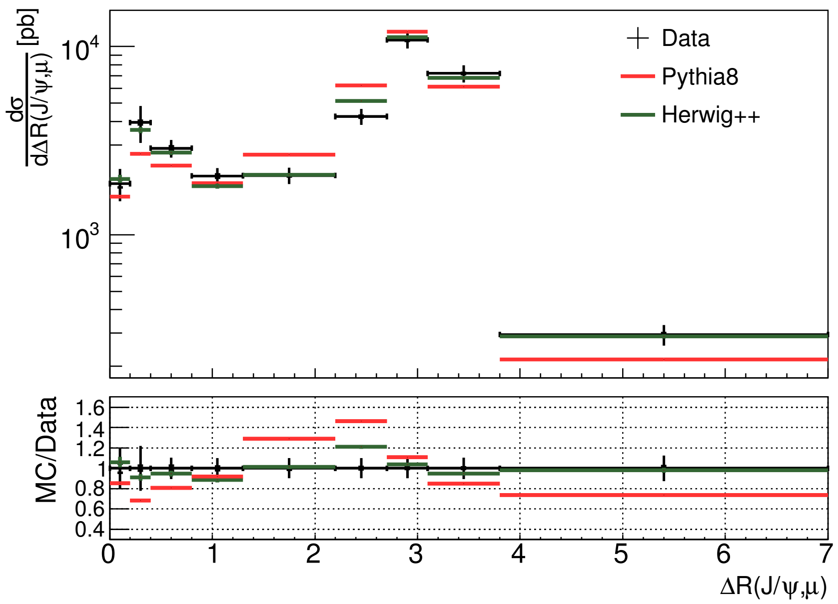

Figure 7.1.: The measured differential cross section binned in $\Delta R(J/\psi, \mu)$. The distribution compared to the Monte Carlo predictions from Pythia and Herwig++ [80].

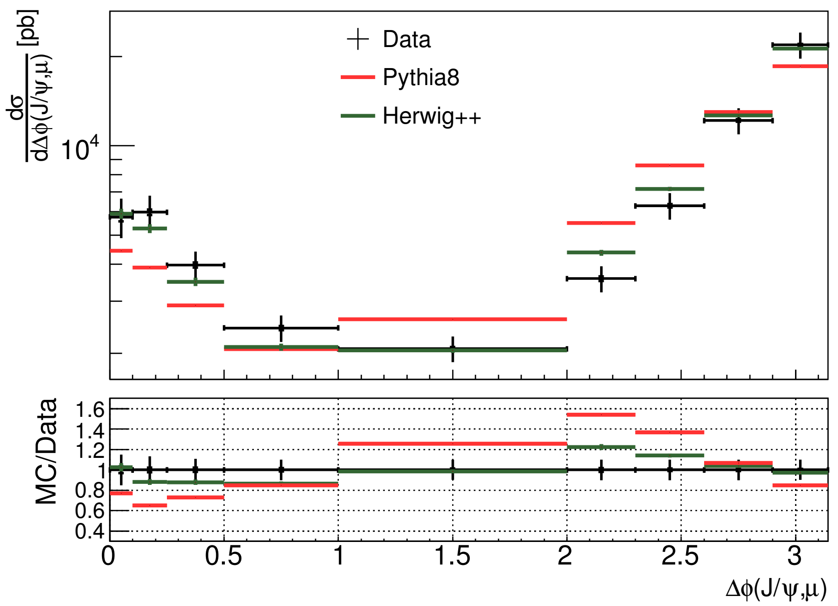

Figure 7.2.: The measured differential cross section binned in $\Delta\phi(J/\psi, \mu)$. The distribution compared to the Monte Carlo predictions from Pythia and Herwig++ [80].

In general, the Herwig++ generator reproduces the shape of the 2012 ATLAS data more accurately in the case of distributions of angular variables. This is especially apparent at low $\Delta R(J/\psi, \mu)$; in this region, the Pythia prediction considerably underestimates

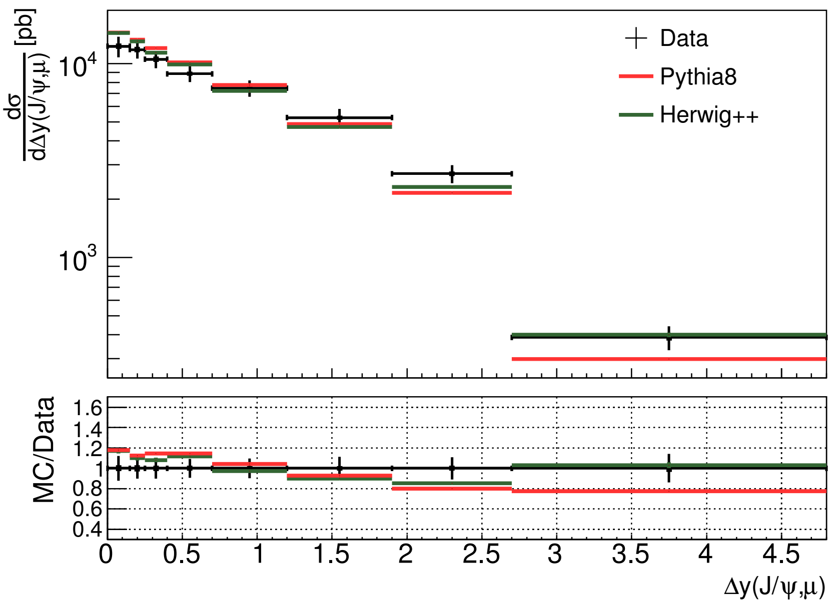

Figure 7.3.: The measured differential cross section binned in $\Delta y(J/\psi, \mu)$. The distribution compared to the Monte Carlo predictions from Pythia and Herwig++ [80].

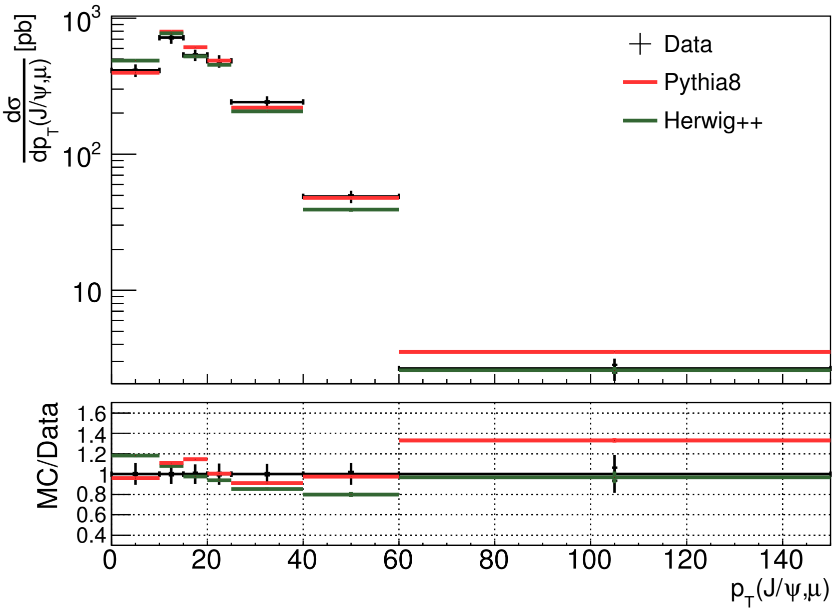

Figure 7.4.: The measured differential cross section binned in $p_T(J/\psi, \mu)$. The distribution compared to the Monte Carlo predictions from Pythia and Herwig++ [80].

the data. However, Herwig++ does not seem to describe the shape of the $p_T(J/\psi, \mu)$ distribution and overestimates events in the low $p_T(J/\psi, \mu)$ region. This distribution is well reproduced by Pythia. Both predictions seem to have a shape dependence for the

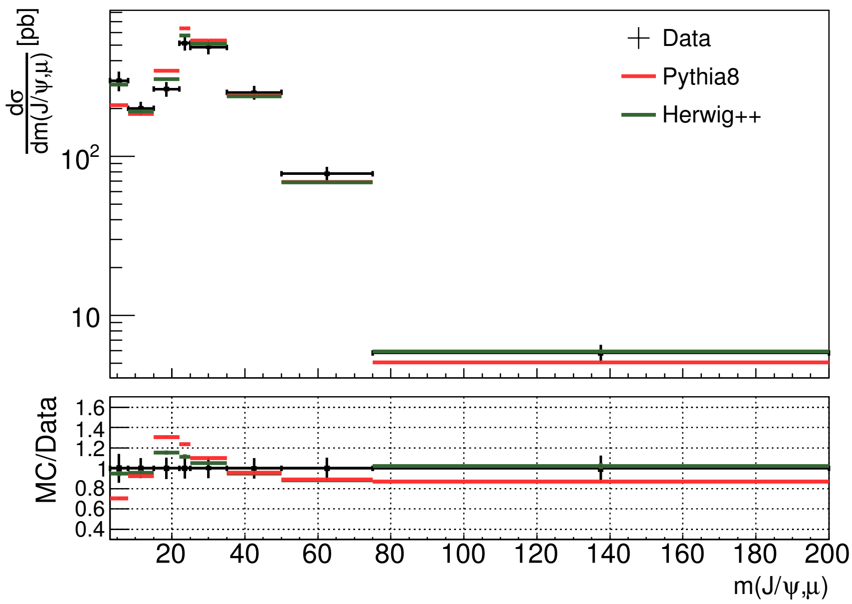

Figure 7.5.: The measured differential cross section binned in $m(J/\psi, \mu)$. The distribution compared to the Monte Carlo predictions from Pythia and Herwig++ [80].

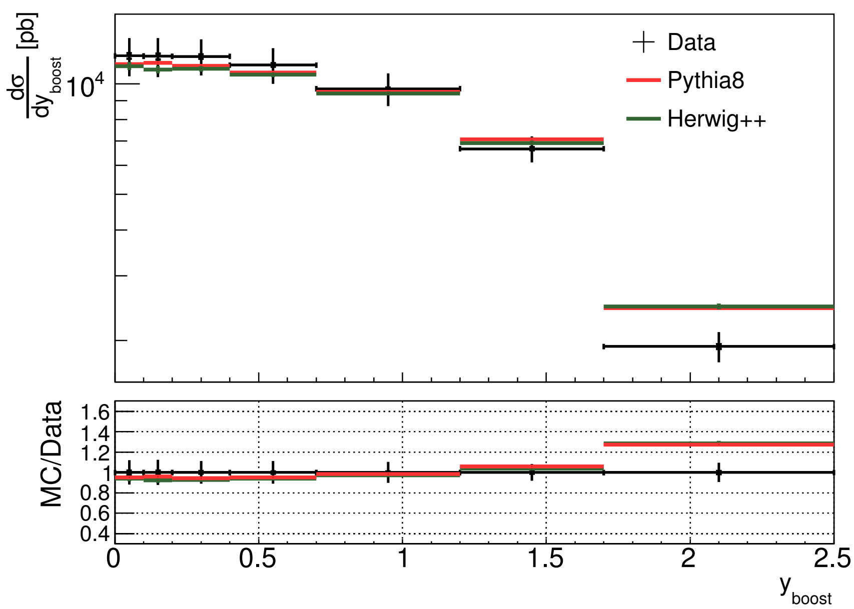

Figure 7.6.: The measured differential cross section binned in y_{boost} distribution compared to the Monte Carlo predictions from Pythia and Herwig++ [80].

$m(J/\psi, \mu)$ distribution, underestimating events in the low and high $m(J/\psi, \mu)$ regions. The y_{boost} distribution for both predictions is very similar with positive deviations from data at high values of y_{boost}.

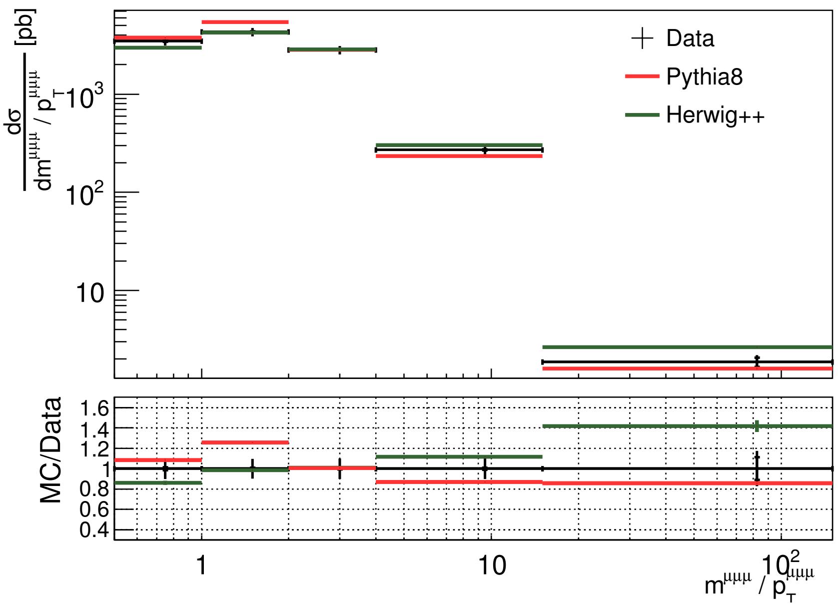

Figure 7.7.: The measured differential cross section binned in for $\frac{m}{p_T}$. The distribution compared to the Monte Carlo predictions from Pythia and Herwig++ [80].

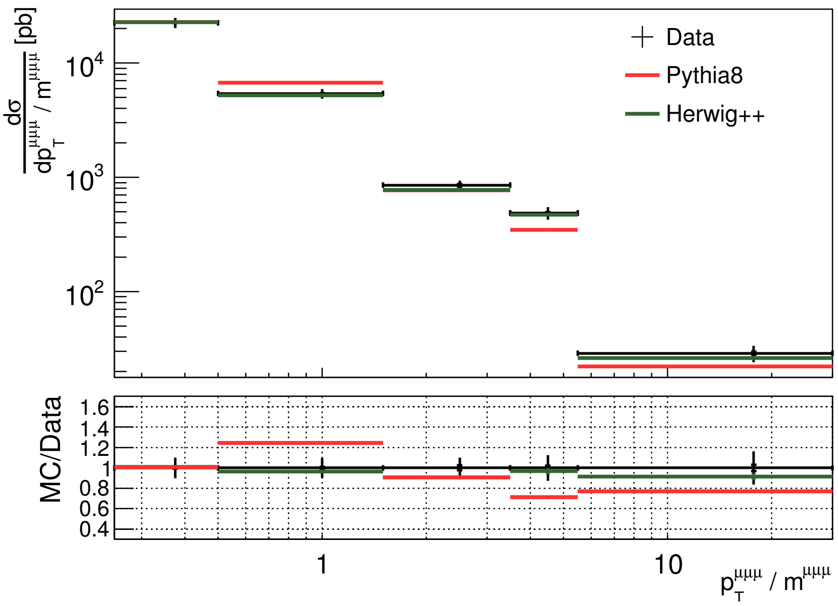

Figure 7.8.: DThe measured differential cross section binned in for $\frac{p_T}{m}$. The distribution compared to the Monte Carlo predictions from Pythia and Herwig++ [80].

7.2. Systematic uncertainties

In this measurement, a wide range of systematic uncertainties is considered. The systematics that were accounted for can be loosely categorized into three groups:

- Uncertainties associated with luminosity and efficiency corrections to the data,
- uncertainties related to the signal and background modeling and
- uncertainties with regard to the backgrounds in the fits.

In the following subsections, each considered source of experimental systematic uncertainty is discussed.

In the presented analysis, the systematic uncertainties are tackled in a way that each systematic error source is considered individually by repeating the fit with systematic change carried out. Then, the difference from the nominal fit result is considered to be the uncertainty for that specific source.

All of the systematics, apart from those concerning J/ψ modeling, are double sided and are varied in both directions. The total systematic uncertainty of the measurement is implemented as the quadrature sum, with all positive (upward) and negative (downward) fluctuations summed accordingly. Then, the maximal deviation of the combination of positive or negative systematics is symmetrized and considered to be the total systematic uncertainty of the measurement.

7.2.1. Luminosity uncertainty

The uncertainty of the delivered integrated luminosity has the assigned value of 2.8%. The exact method of deriving this value is defined in [97].

7.2.2. Trigger and muon reconstruction efficiency uncertainty

The uncertainty of the trigger and muon reconstruction maps was detailed in section 5.3. The trigger efficiency is factorized into two components: the single muon trigger maps and the $c_{\mu\mu}$ factor. The uncertainty of $\epsilon^{x}_{ROI}(p_T, q \cdot \eta)$ has been derived from the spread in dataset yields by using a series of pseudo maps to re-weight the dataset. This spread is propagated to the number of fitted signal events to define the trigger map uncertainty.

The uncertainty of $c_{\mu\mu}$ is applied separately by varying the nominal function by $\pm 1\sigma$, its associated error, consistently when re-weighting the dataset. In addition, an uncertainty of the efficiency correction is applied for cases when the third muon is close to a trigger muon, as discussed in section 5.3.3. The parameters of the function describing the correction are varied within errors to define two systematic functions used in lieu of the nominal function to determine the uncertainty. These are included along with the nominal correction in figure 5.5 for the case where the muons are of opposite charge.

The uncertainties of muon reconstruction efficiencies are defined for both components of of event weight. A 0.5% uncertainty is included for the efficiency of reconstructing a muon track in the ID, ϵ_{trk}. This is added coherently for each muon of the three muons in an event resulting in a flat 1.5% systematic uncertainty. Similarly as the trigger map efficiency, the uncertainty of the muon reconstruction maps, $\epsilon_{\mu}(p_T, q \cdot \eta)$, is defined by the spread on the dataset yields when using a set of pseudo maps.

Figure 7.9 shows the relative fractional uncertainty for each of these detector efficiency corrections for the differential distributions. The uncertainty of $c_{\mu\mu}$ in general gives the largest systematic for the efficiency corrections with a fractional uncertainty of $\approx 3\%$.

7.2.3. Template statistical uncertainty

The statistical uncertainty template of the Monte Carlo templates used for the 3^{rd} muon fits is assessed by performing each fit repeatedly 100 times with a set of toy templates. In each of those toy templates used in the fit, non-prompt, prompt real and fake muons are randomly sampled to produce a toy template that has the same number of events as the nominal case. The fit is then repeated using the toy templates and the number of fitted signal muons is recorded. The non-prompt muon yield distribution acquired in the toy fits is fitted with a Gaussian function, with the width taken as a systematic uncertainty of the statistical fluctuations of the Monte Carlo templates. Figure 7.9 includes the relative fractional uncertainty due to template statistics for the $\Delta\phi(J/\psi, \mu)$ distribution, where it typically contributes at the 1% level.

7.2.4. Fake J/ψ pile-up events

The contribution from events with a fake J/ψ candidate which is combined with a third muon from another pp interaction, i.e. an event which falls in both the fake J/ψ and pile-up categories, is double counted by the fitting process. It was found by fitting the Δz_0 distribution of events outside the signal mass window that approximately 2% of fake J/ψ events are from pile-up events. This is in agreement with events inside the mass window, where pile-up also contributes 2% of selected events. As the fake J/ψ background is typically 10% of the signal, the effect of the double counting is expected to be small ($10\% \times 2\%$). A systematic to cover the effect of any double counting of these backgrounds is defined for each differential bin. The signal yield is altered by the level of double counting in that bin. Explicitly, this is the multiplication of the fraction of the fitted dataset that is pile-up and the fraction of the fit that is fake J/ψ. Figures 7.9 and 7.10 include the relative fractional uncertainty due to background double counting for the $\Delta\phi(J/\psi, \mu)$ distribution, where it typically contributes below 1%.

7.2.5. Unfolding uncertainty

An uncertainty of the correction factors used to correct for events migrating in and out of acceptance is defined by the statistical uncertainty of the Monte Carlo sample used to define the correction. The correction, as described in section 6.3, is derived from the ratio of events passing the truth selection to events passing the reconstructed selection. The uncertainty of this ratio is calculated assuming these samples are uncorrelated, which is not the case as they are derived from the same Monte Carlo sample, so this represents a conservative estimate of an uncertainty of this correction. Figures 7.9 and 7.10 include the relative fractional uncertainty due to the unfolding correction for the $\Delta\phi(J/\psi, \mu)$ distribution, where it typically contributes at the 1% level.

7.2.6. Fake muon template uncertainty

The fake muon template contains two types of background with similar behavior: DIF and hadronic leakage, as explained in section 6.1.4. Both backgrounds are due to the decay or interactions of $\pi^\pm$ and $K^\pm$. To assess the robustness of the Monte Carlo modeling of the fake muon background the templates used in the third muon fits were systematically altered.

Firstly, the fraction of $\pi^\pm$ to $K^\pm$ populating the fake muon templates is changed by $\pm 50\%$. The BDT response is subtly different for $\pi^\pm$ and $K^\pm$, but due to limited statistics of fake muon candidates in Monte Carlo, the two sources of fake muons have been combined, changing the ratio which should cover any effect of the combination.

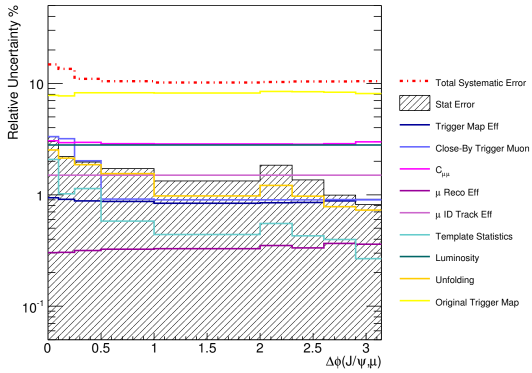

(a) $\Delta\phi(J/\psi, \mu)$

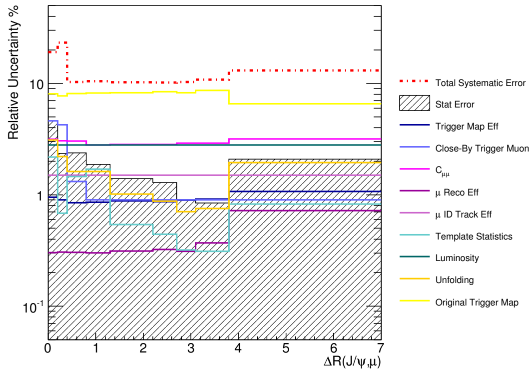

(b) $\Delta R(J/\psi, \mu)$

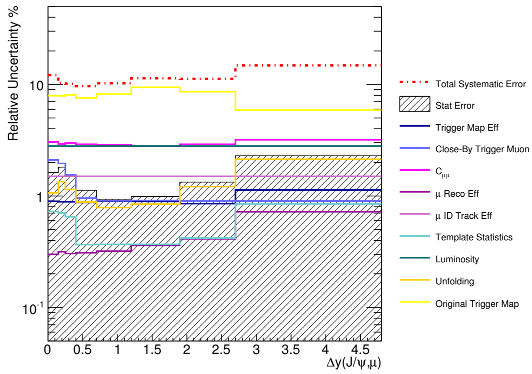

(c) $\Delta y(J/\psi, \mu)$

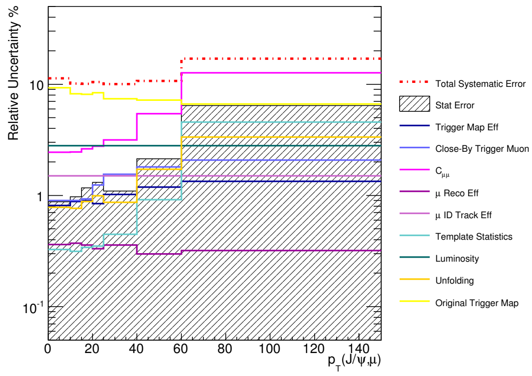

(d) $p_T(J/\psi, \mu)$

Figure 7.9.: Relative systematic uncertainties for trigger and muon reconstruction efficiencies, luminosity uncertainty and template statistical uncertainty as a function of a corresponding variables. The statistical uncertainty and total systematic uncertainty is included for comparison. Only the largest relative uncertainty of either the upward or downward systematic is plotted [80].

Secondly, the ratio of the number of decays of DIF muons inside the ID and outside the ID is varied by $\pm 50\%$. As the BDT has variables that specially pick out fake muons in certain parts of the detector, it is important to assess a potential mismodeling of the radial decay position of fake muons in MC. Finally, the ratio of DIF muons and hadronic leakage muons in the fake muon template is changed by $\pm 50\%$. The BDT response is different for the two types of fake muons, as two of the BDT variables are based on ID variables which have little discriminative power for hadronic leakage faking muons. The fake muon template from MC is composed of approximately 75% DIF muons, with the available Monte Carlo statistics not allowing separation of the two contributions. Changing the fractional composition of the fake muon template should

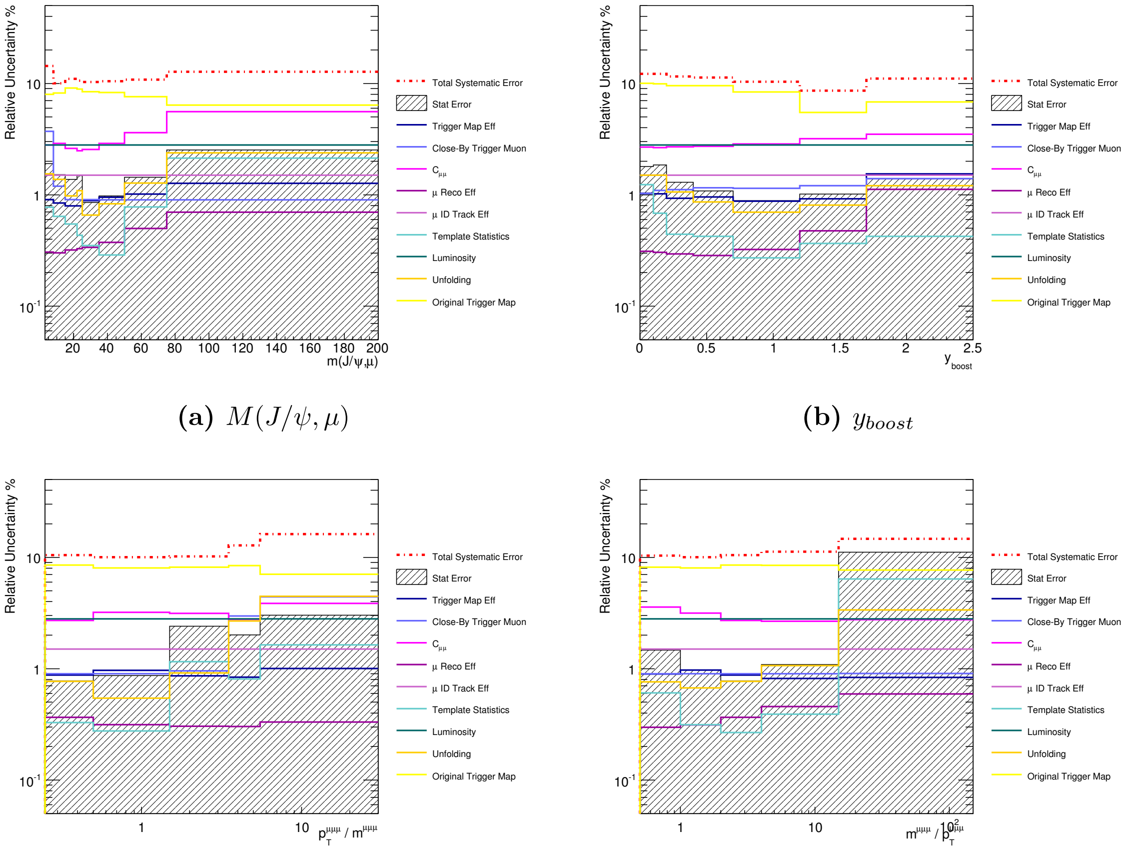

(a) $M(J/\psi, \mu)$ (b) y_{boost}

(c) $\frac{p_T}{m}$ (d) $\frac{m}{p_T}$

Figure 7.10.: Relative systematic uncertainties for trigger and muon reconstruction efficiencies, luminosity uncertainty and template statistical uncertainty as a function of a corresponding variables. The statistical uncertainty and total systematic uncertainty is included for comparison. Only the largest relative uncertainty of either the upward or downward systematic is plotted [80].

cover any mismodeling in Monte Carlo of the composition of the two sources of fake muons.

The effects these systematic shifts have on the BDT template can be inferred from figure 7.11, where the Monte Carlo fake muon template is broken down into all the individual sources that are varied as part of the fake muon template uncertainties.

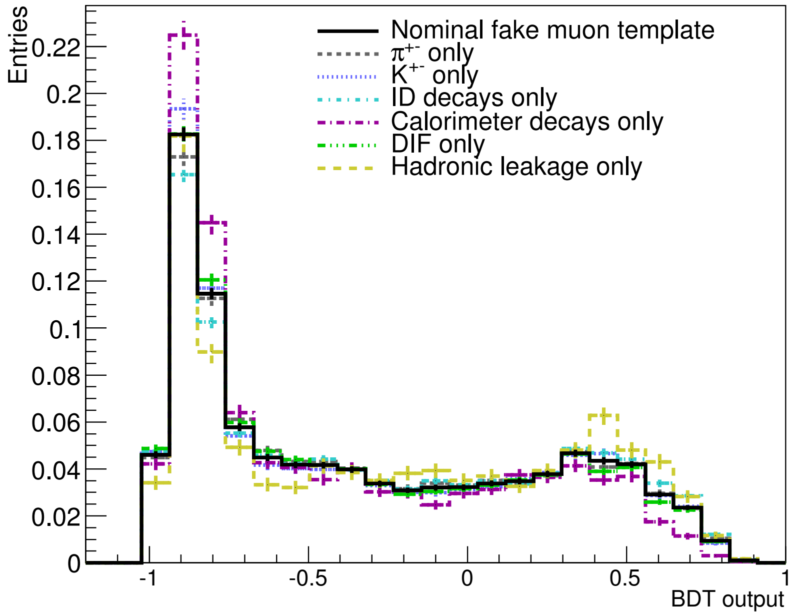

Figure 7.11.: Unit normalised BDT output distribution for fake muons. The nominal fake muon template is split into six contributing components [80].

7.2.7. B_c background uncertainty

The B_c background prediction is taken from the average of Pythia and Herwig++ Monte Carlo predictions, as discussed in section 6.1.6. The difference between the two predictions is assigned as an uncertainty of the number of B_c mesons in the dataset.

7.2.8. $B+D$ events uncertainty

Similarly to the B_c meson background, and as discussed in section 6.1.7, the number of events estimated to be from $B + D$ hadrons is taken from the average of Pythia and Herwig++ Monte Carlo predictions. A systematic uncertainty to this prediction is applied, using the difference between Pythia and Herwig++ for the rate of $B + D$ events.

7.2.9. Punch-through background

The punch-through background prediction taken from the simulation is varied by $\pm$ 50% to serve as an estimate of the uncertainty of this background.

7.2.10. Data-Driven background uncertainties

The uncertainty of the fake J/ψ background is assessed by changing the normalization of the fake J/ψ templates in the 3^{rd} muon fits. The number of fake J/ψ events was extracted from the 2D di-muon fits, given by normalization of the of the three fake J/ψ components within the di-muon signal mass window. Due to the di-muon pseudo-lifetime cut in the third muon fit region, the single sided fake J/ψ component is the only background to contribute non-negligibly to the high pseudo-proper lifetime region. The differential fits are repeated with fake J/ψ template normalization altered by $\pm 1\sigma$ error of the normalization of the single-sided background.

For the estimation of the pile-up background uncertainty, a similar procedure is used. The templates used in the 3^{rd} muon fits are changed by altering the normalization within the fit result uncertainty. The uncertainty is derived from the Gaussian fit to Δz_0, see figure 6.6, and is applied as a $\pm 1\sigma$ variation to nominal pile-up templates.

Figures 7.12 and 7.13 show the relative uncertainty of all the background systematic variations for each differential distribution.

7.2.11. J/ψ Model Uncertainty

The uncertainty of the J/ψ model in the extracted number of non-prompt J/ψ candidates taken from the simultaneous mass-lifetime di-muon fit was assessed by perturbing the five fit components of the model.

The fitting was repeated for each of the varied J/ψ models, with only one change at a time. To avoid double counting of uncertainty, the envelope of the largest deviation from the nominal event yield is taken as the total systematic for the J/ψ model uncertainty when considering all the individual model changes. This envelope is calculated separately in each differential bin. The nominal fit model is listed in table 6.1, with the individual systematic changes to the J/ψ model listed below:

- The J/ψ mass model was switched to two Gaussian functions.
- The non-prompt J/ψ pseudo-proper lifetime model was changed to double exponential function convoluted with the same resolution function.
- The resolution model was changed to a single Gaussian.

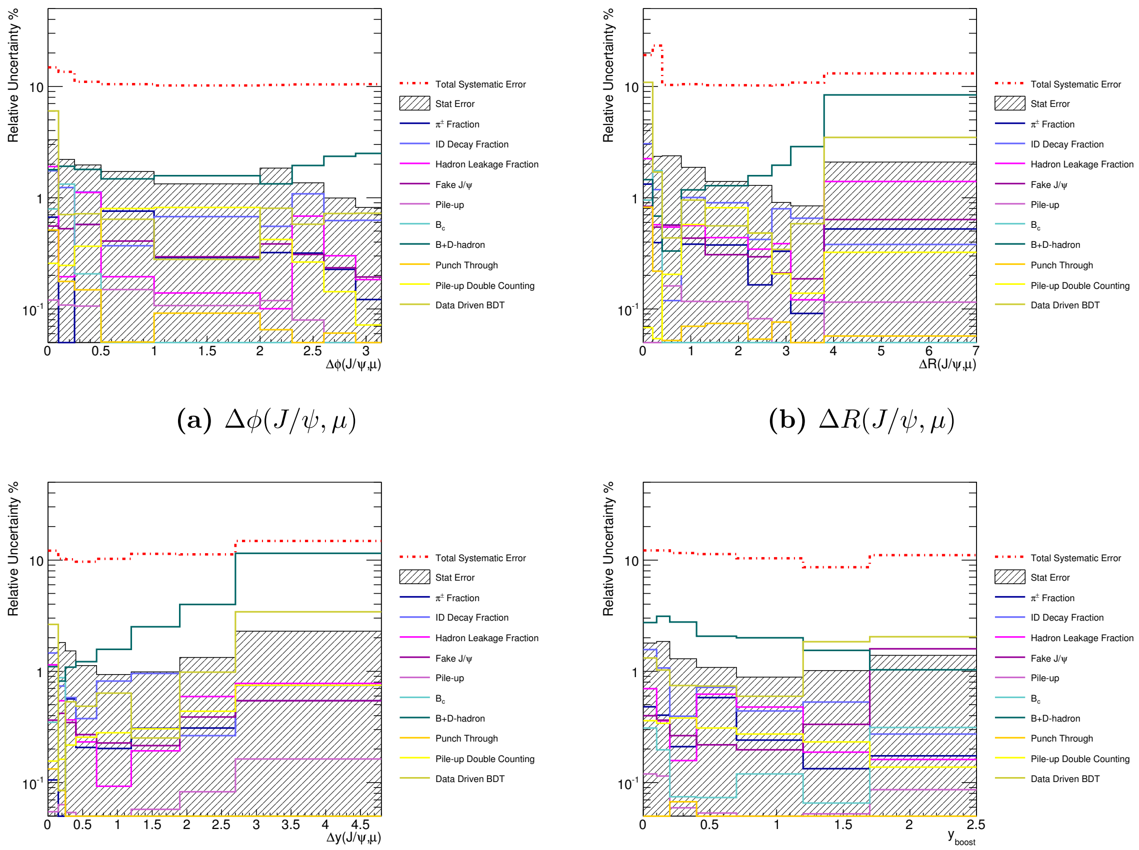

(a) $\Delta\phi(J/\psi, \mu)$ **(b)** $\Delta R(J/\psi, \mu)$

(c) $\Delta y(J/\psi, \mu)$ **(d)** y_{boost}

Figure 7.12.: Relative background modeling uncertainties as a function of corresponding variables. The statistical uncertainty and total systematic uncertainty is included for comparison. Only the largest relative uncertainty from either the upward or downward systematic is plotted [80].

- The Crystal Ball function's fixed parameters are varied by $\pm 10\%$.
- The prompt fake J/ψ background had its di-muon mass model interchanged with an exponential function.
- The double sided fake J/ψ background had its di-muon mass model interchanged with an exponential function.
- The single sided fake J/ψ background had its di-muon mass model interchanged with a first order polynomial function.
- The single sided fake J/ψ pseudo-proper lifetime model was swapped from a single to a double exponential function.

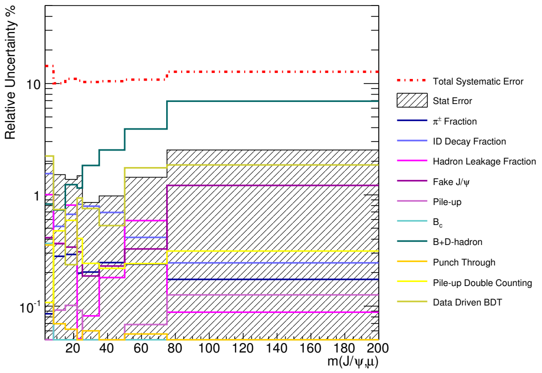

(a) $M(J/\psi, \mu)$

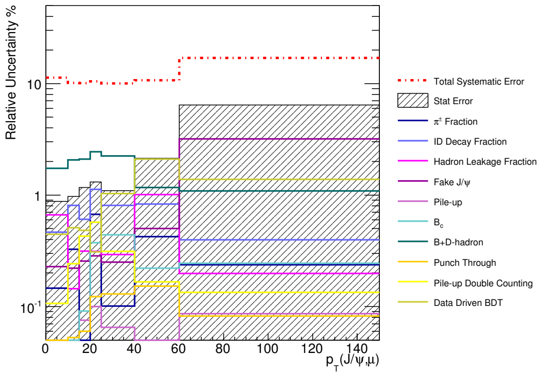

(b) $p_T(J/\psi, \mu)$

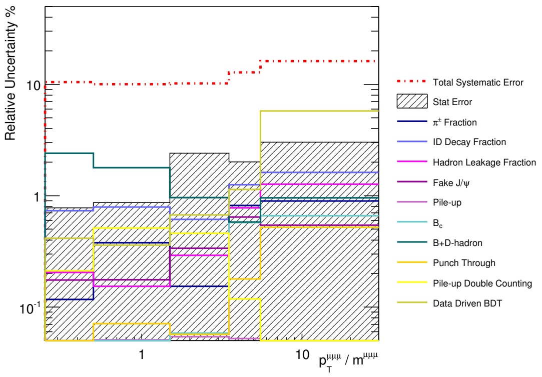

(c) $\frac{p_T}{m}$

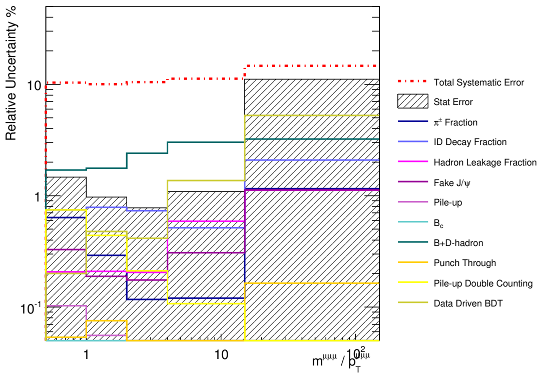

(d) $\frac{m}{p_T}$

Figure 7.13.: Relative background modeling uncertainties as a function of corresponding variables. The statistical uncertainty and total systematic uncertainty is included for comparison. Only the largest relative uncertainty from either the upward or downward systematic is plotted [80].

Figures 7.14 and 7.15 show the model systematics as a function of each differential observable, which includes the envelope which is taken as the uncertainty of the J/ψ modeling. The dominating model uncertainties are from changing the lifetime parameterization of the non-prompt J/ψ and mass parameterization of the single sided fake J/ψ background.

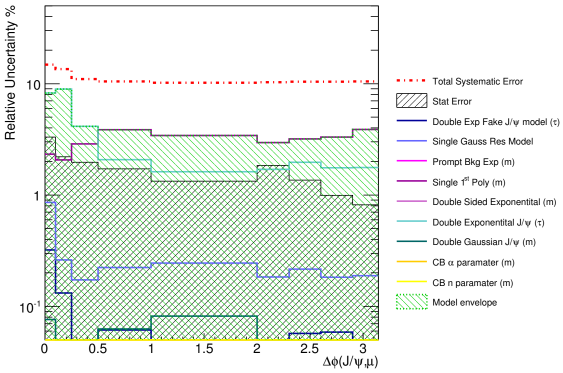

(a) $\Delta\phi(J/\psi, \mu)$

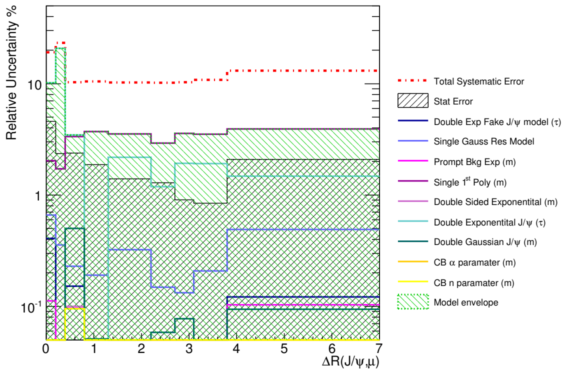

(b) $\Delta R(J/\psi, \mu)$

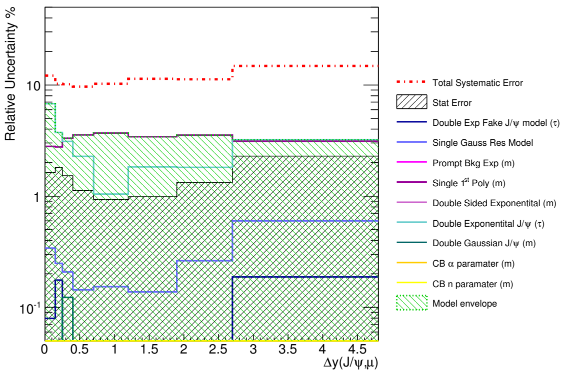

(c) $\Delta y(J/\psi, \mu)$

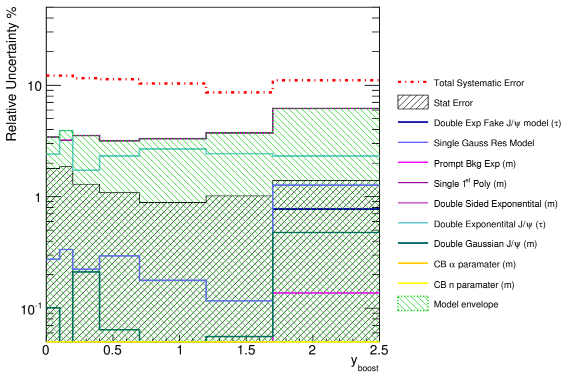

(d) y_{boost}

Figure 7.14.: Relative uncertainty for J/ψ model systematics as a function of corresponding variables. The individual model changes are plotted including the envelope used to define the model systematic. The statistical uncertainty and total systematic uncertainty is included for comparison [80].

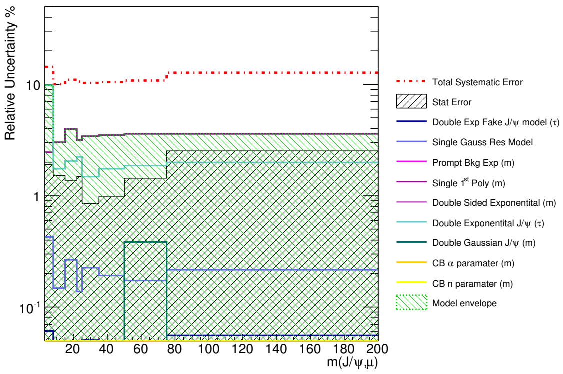

(a) $M(J/\psi, \mu)$

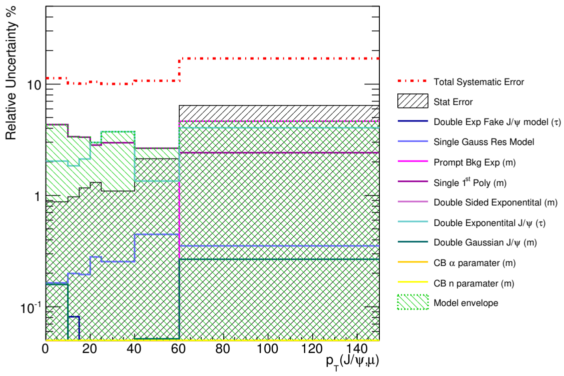

(b) $p_T(J/\psi, \mu)$

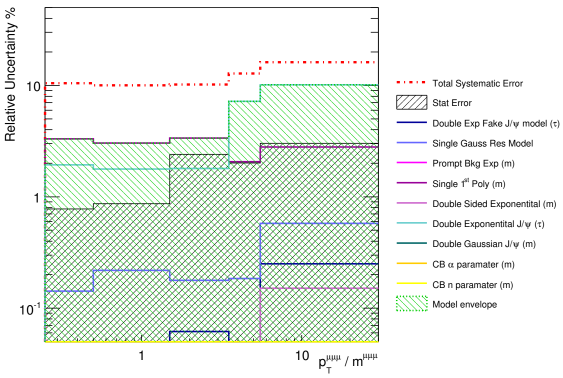

(c) $\frac{p_T}{m}$

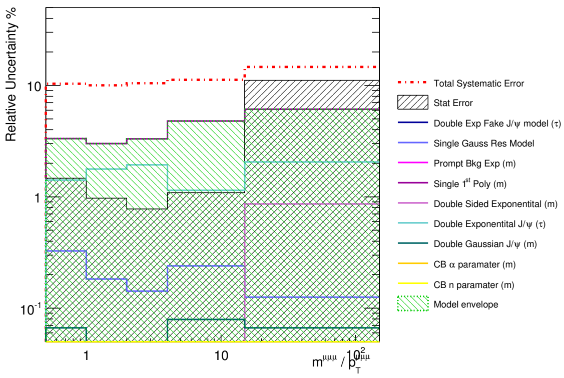

(d) $\frac{m}{p_T}$

Figure 7.15.: Relative uncertainty for J/ψ model systematics as a function of corresponding variables. The individual model changes are plotted including the envelope used to define the model systematic. The statistical uncertainty and total systematic uncertainty is included for comparison [80].

Chapter 8.

Conclusions

The first analysis of bottom quark production of terms of the Quantum Chromodynamics theory in pp collisions at $\sqrt{s}$= 8 TeV at the ATLAS experiment has been performed. This analysis follows up on the historical measurements by UA1, D0, CDF and CMS collaborations.

Detailed bottom quark production studies provide an essential information about the underlying dynamics of the QCD processes. At the Large Hadron Collider, beauty quarks play an important role in some physics analyses, such as in top quark physics or Higgs studies. At the same time, $b\bar{b}$ pairs are one of the main backgrounds for many new physics searches and detailed understanding of the background is crucial. Analysis of $b\bar{b}$ correlations represents a complex task, because the physical signatures are burdened by many abundant backgrounds, several of which are highly correlated to the measured signal. Advanced multivariate methods for dealing with backgrounds were devised in the course of the analysis and were successfully applied.

The resulting cross section measurements were performed on the 2012 ATLAS $\sqrt{s}$ = 8 TeV data, using models and templates derived from data and Monte Carlo methods. The sample corresponds to an integrated luminosity of $\approx$ 11.44 fb $^{-1}$.

The differential $b\bar{b}$ cross sections are measured via the $J/\psi + \mu$ proxies. The measurements of the differential cross sections presented in this thesis are binned in angular observables $\Delta\phi, \Delta y, \Delta R$, kinematic observables of average rapidity y_{boost}, invariant mass m and p_T of the $J/\psi + \mu$ system, and their ratios p_T/m and m/p_T. The azimuthal angle distribution between $b\bar{b}$ pair is shown in Figure 7.2, where abundance of events in the low $\Delta\phi$ region is evident, which indicates the dominance of NLO over LO contributions of the flavor creation-like processes.

The analysis progress and its results were periodically presented at the corresponding workgroup and collaboration meetings. The presented work contains the first clear observation of the gluon splitting effects at $\sqrt{s} = 8$ TeV. The data presented here are consistent with older CMS measurements at $\sqrt{s} = 7$ TeV and the growth of an event yield at low $\Delta\phi$ is a result of growing proportion of the gluon-splitting processes as is discussed in section 1.3. After approval of the analysis note [80] by the ATLAS collaboration, it will be submitted for publication.

Appendix A.

Appendices

A.1. Details of fit for each observable

Figures A.7-A.15 show differential J/ψ mass-lifetime fits for all differential observables. Figures A.8-A.16 show differential third muon fits for all differential observables.

A.2. Proxy transfer functions

The proxy transfer functions (PTFs) allow transformation of variables from the $J/\psi + \mu$ system into the $B\bar{B}$ system. They are. $\Delta\phi$, ΔR, Δy and the p_T, invariant mass and rapidity of the $J/\psi + \mu$ system. The PTFs are shown in figures A.17 and A.18.

A.3. B_c background

Table A.1 shows the B_c correction subtracted from the dataset for each differential bin defined in table 4.1.

A.4. D meson background

Table A.2 shows the D meson correction subtracted from the dataset for each differential bin defined in table 4.1.

Bin number	$\Delta\phi$	Δy	ΔR	p_T	Mass	y_{boost}	$\frac{p_T}{m}$	$\frac{m}{p_T}$
1	3.4	1.1	4.9	0.3	3.5	0.3	0	1.2
2	3.1	1.2	3.9	0.1	0	0.1	0	0
3	0.6	0.3	0.1	0.2	0	0.2	0	0
4	0	0	0	0.2	0	0.2	0	0
5	0	0	0	0.3	0	0.3	1.3	0
6	0	0	0	0.3	0	0.3	3.1	0
7	0	0	0	0.7	0	0.7		
8	0	0	0		0			
9	0		0					

Table A.1.: The B_c meson corrections subtracted from the fitted data for each corresponding bin.

Bin number	$\Delta\phi$	Δy	ΔR	p_T	Mass	y_{boost}	$\frac{p_T}{m}$	$\frac{m}{p_T}$
1	1.5	1.3	0.8	2.5	0.7	4.5	3.7	0.8
2	1.1	1.4	0.4	2.5	1.1	3.0	3.0	1.9
3	1.6	1.6	0.9	2.9	1.3	3.3	2.6	2.7
4	2.1	1.7	1.3	2.7	1.8	3.1	1.3	3.0
5	2.3	2.3	1.6	2.6	2.2	2.6	0.7	3.7
6	2.4	3.1	2.0	3.1	3.4	2.1	0.8	4.0
7	2.4	5.2	2.7	3.7	5.5	1.5		
8	3.1	9.6	3.8		8.0			
9	3.4		7.8					

Table A.2.: The D meson corrections subtracted from the fitted data for each corresponding bin.

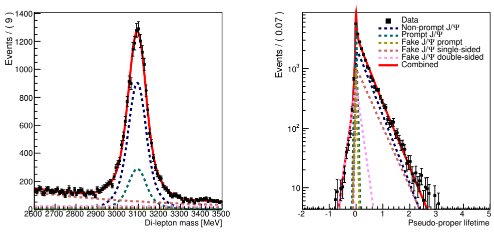

(a) $0<\Delta\phi<0.1$

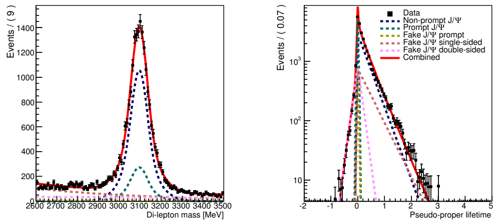

(b) $0.1<\Delta\phi<0.25$

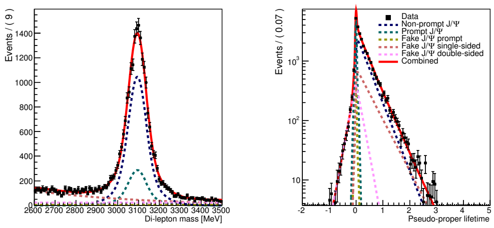

(c) $0.25<\Delta\phi<0.5$

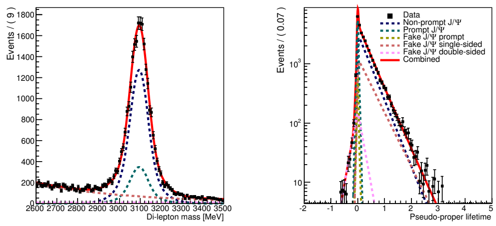

(d) $0.5<\Delta\phi<1.0$

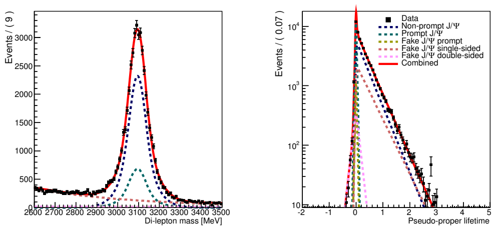

(e) $1.0<\Delta\phi<2.0$

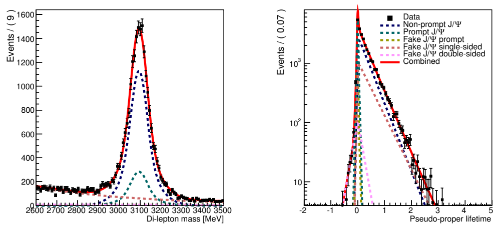

(f) $2.0<\Delta\phi<2.3$

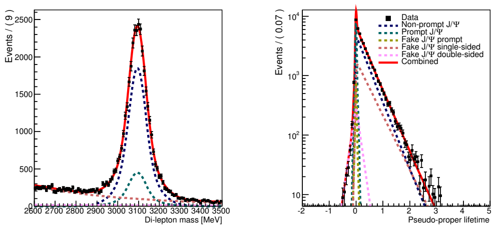

(g) $2.3<\Delta\phi<2.6$

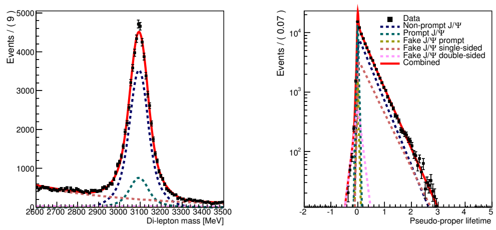

(h) $2.6<\Delta\phi<2.9$

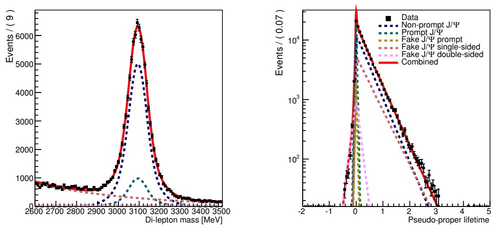

(i) $2.9<\Delta\phi<\pi$

Figure A.1.: 2D J/ψ fit results for $\Delta\phi$ obsevable.

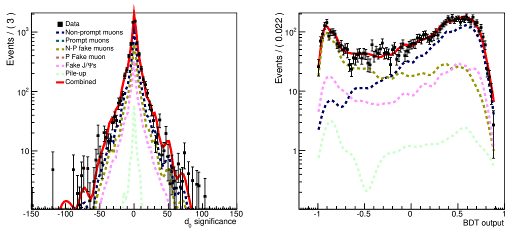

(a) $0<\Delta\phi<0.1$

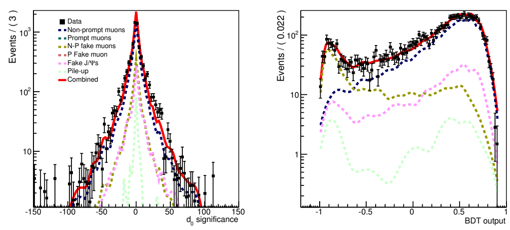

(b) $0.1<\Delta\phi<0.25$

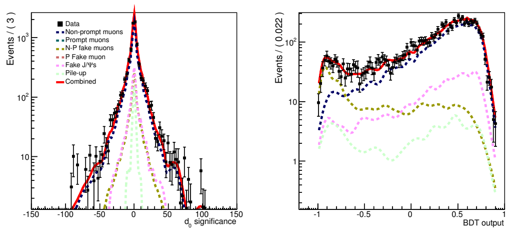

(c) $0.25<\Delta\phi<0.5$

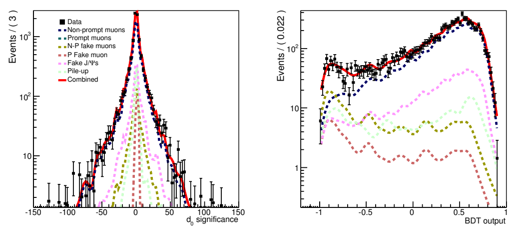

(d) $0.5<\Delta\phi<1.0$

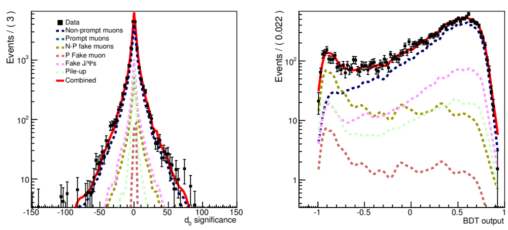

(e) $1.0<\Delta\phi<2.0$

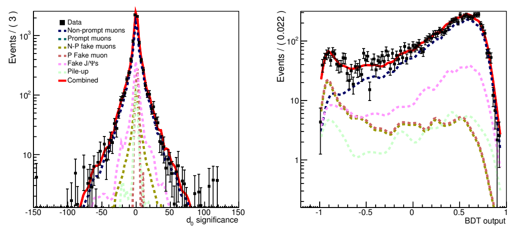

(f) $2.0<\Delta\phi<2.3$

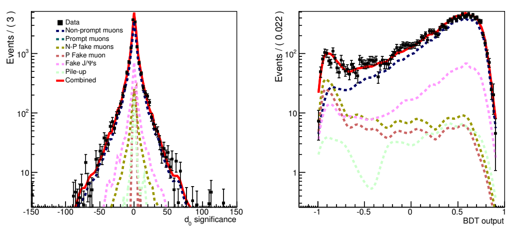

(g) $2.3<\Delta\phi<2.6$

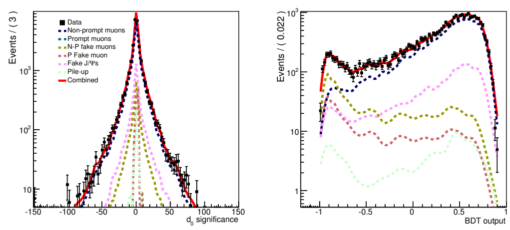

(h) $2.6<\Delta\phi<2.9$

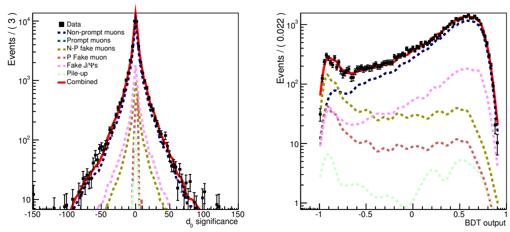

(i) $2.9<\Delta\phi<\pi$

Figure A.2.: 2D 3^{rd} muon fit results for $\Delta\phi$ obsevable.

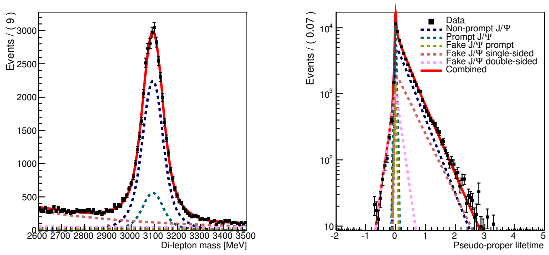

(a) $0<\Delta y<0.1$

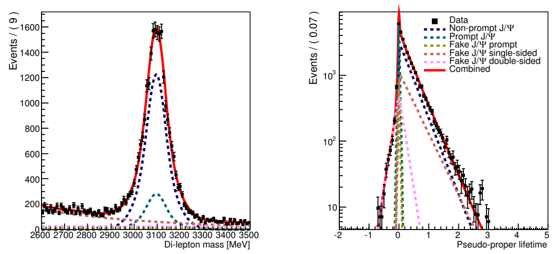

(b) $0.1<\Delta y<0.2$

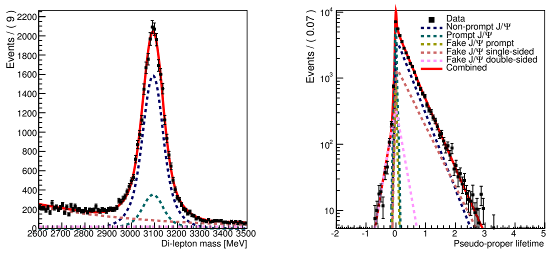

(c) $0.2<\Delta y<0.4$

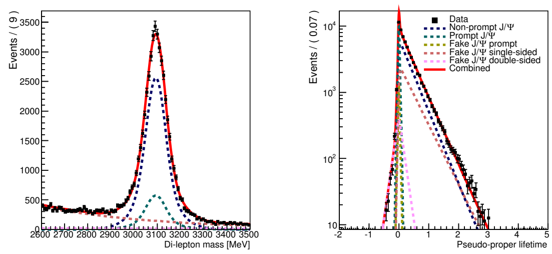

(d) $0.4<\Delta y<0.7$

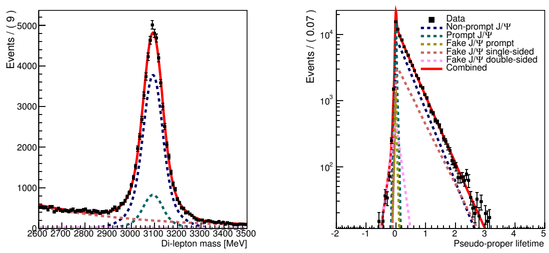

(e) $0.7<\Delta y<1.2$

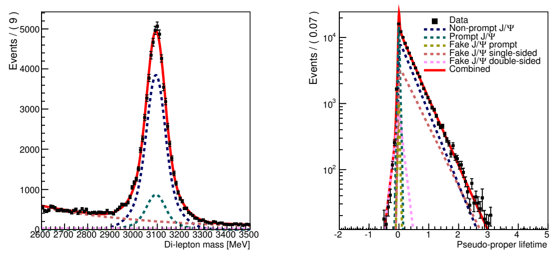

(f) $1.2<\Delta y<1.9$

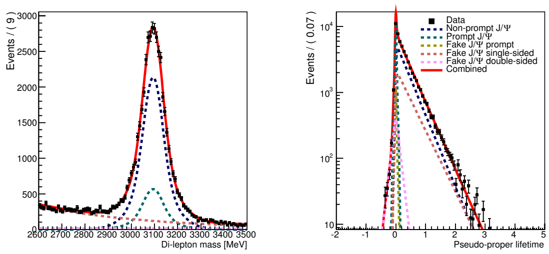

(g) $1.9<\Delta y<2.7$

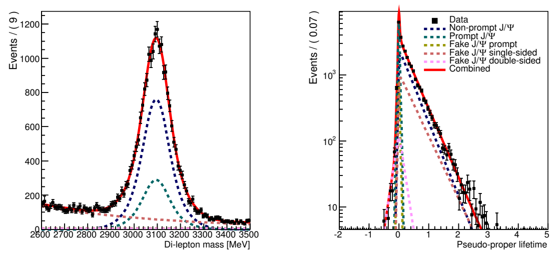

(h) $2.7<\Delta y<4.8$

Figure A.3.: 2D J/ψ fit results for Δy obsevable.

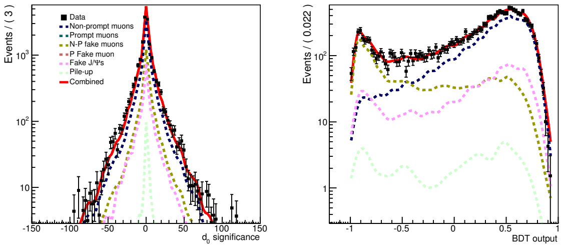

(a) $0<\Delta y<0.1$

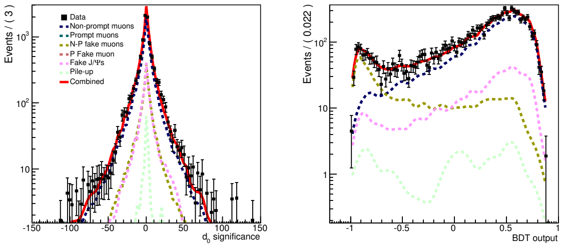

(b) $0.1<\Delta y<0.2$

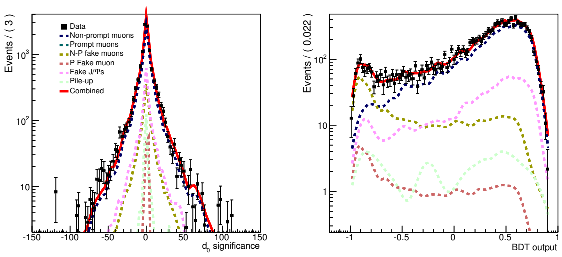

(c) $0.2<\Delta y<0.4$

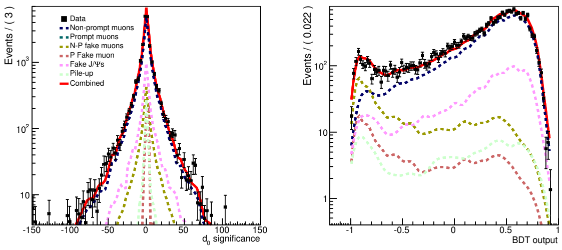

(d) $0.4<\Delta y<0.7$

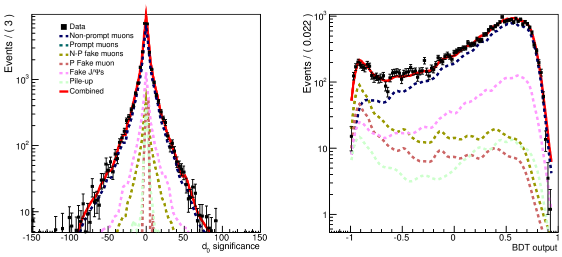

(e) $0.7<\Delta y<1.2$

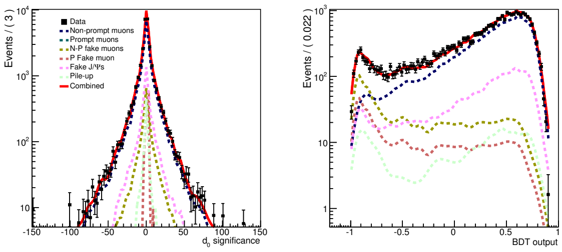

(f) $1.2<\Delta y<1.9$

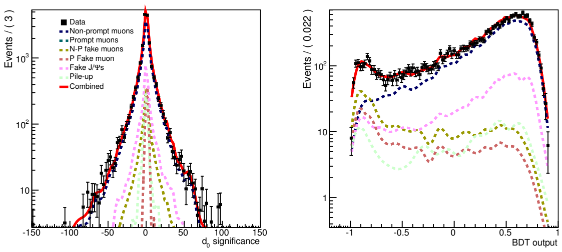

(g) $1.9<\Delta y<2.7$

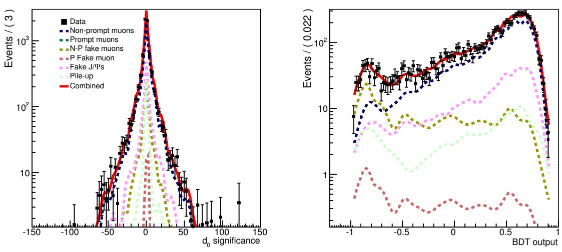

(h) $2.7<\Delta y<4.8$

Figure A.4.: 2D 3^{rd} muon fit results for Δy obsevable.

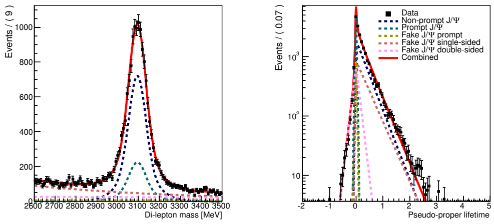

(a) $0<\Delta R<0.2$

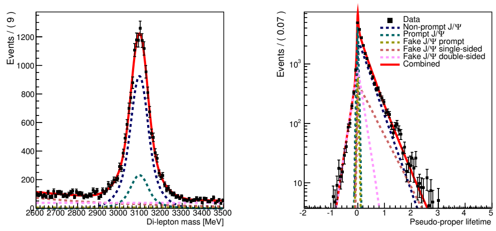

(b) $0.2<\Delta R<0.4$

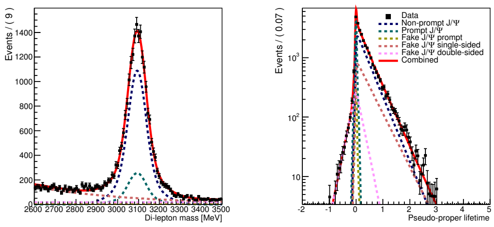

(c) $0.4<\Delta R<0.8$

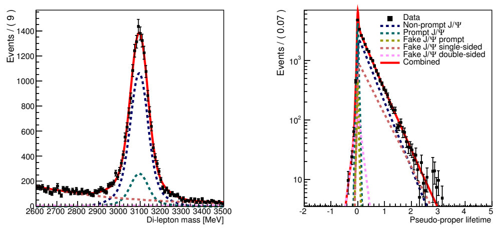

(d) $0.8<\Delta R<1.3$

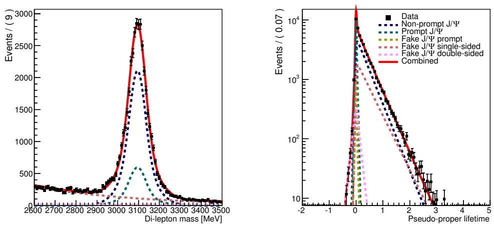

(e) $1.3<\Delta R<2.2$

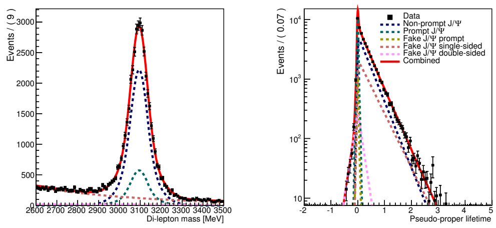

(f) $2.2<\Delta R<2.7$

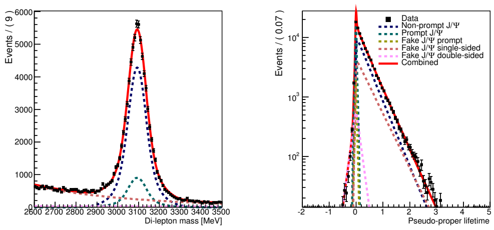

(g) $2.7<\Delta R<3.1$

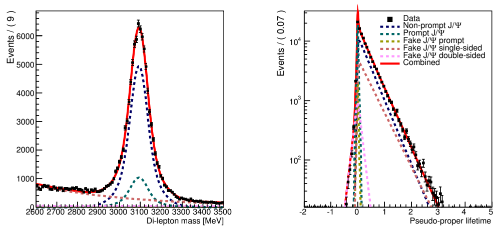

(h) $3.1<\Delta R<3.8$

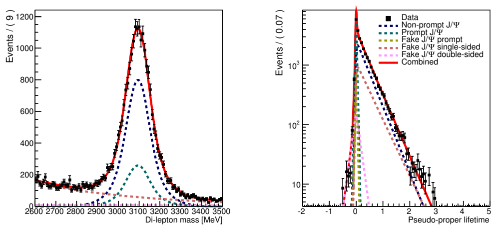

(i) $3.8<\Delta R<7$

Figure A.5.: 2D J/ψ fit results for ΔR observable.

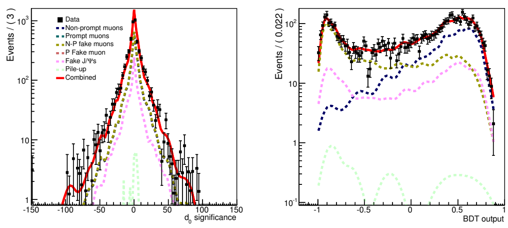

(a) $0<\Delta R<0.2$

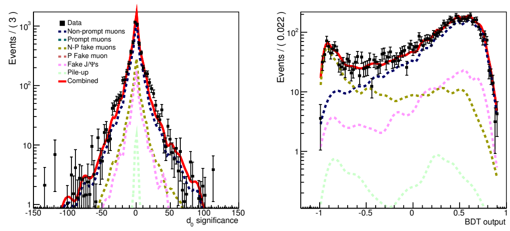

(b) $0.2<\Delta R<0.4$

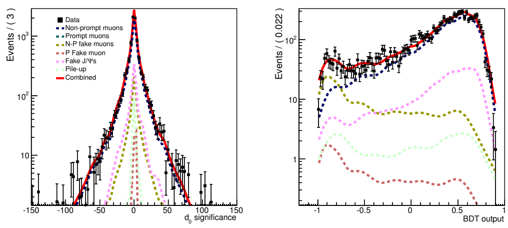

(c) $0.4<\Delta R<0.8$

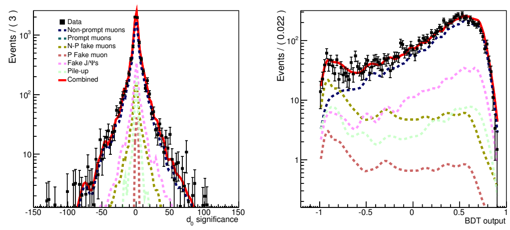

(d) $0.8<\Delta R<1.3$

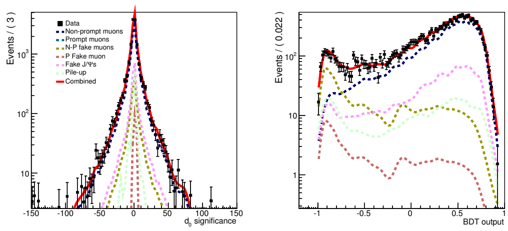

(e) $1.3<\Delta R<2.2$

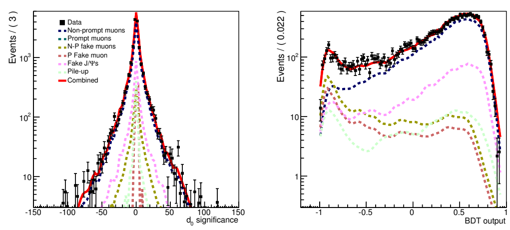

(f) $2.2<\Delta R<2.7$

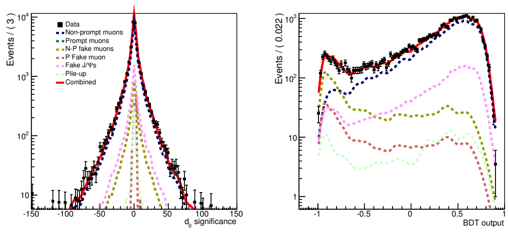

(g) $2.7<\Delta R<3.1$

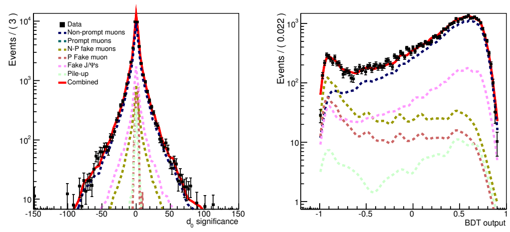

(h) $3.1<\Delta R<3.8$

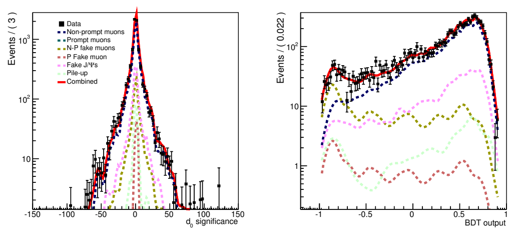

(i) $3.8<\Delta R<7$

Figure A.6.: 2D 3^{rd} muon fit results for ΔR obsevable.

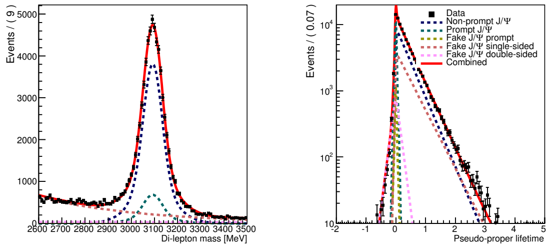

(a) $0<p_T^{\mu\mu\mu}<10$ GeV

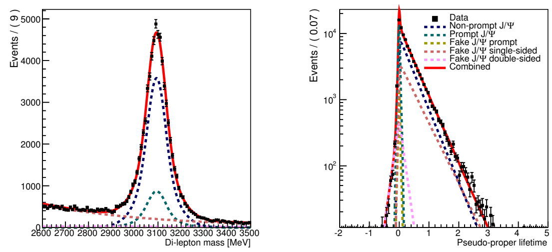

(b) $10<p_T^{\mu\mu\mu}<15$ GeV

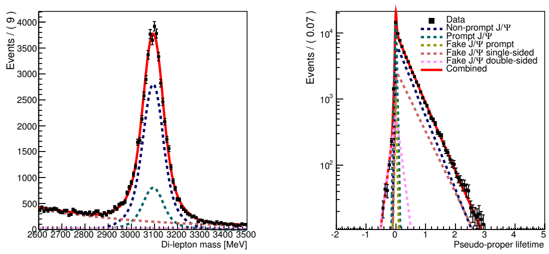

(c) $15<p_T^{\mu\mu\mu}<20$ GeV

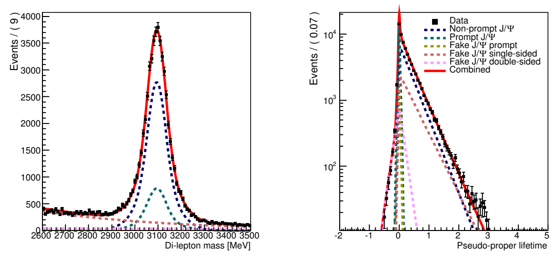

(d) $20<p_T^{\mu\mu\mu}<25$ GeV

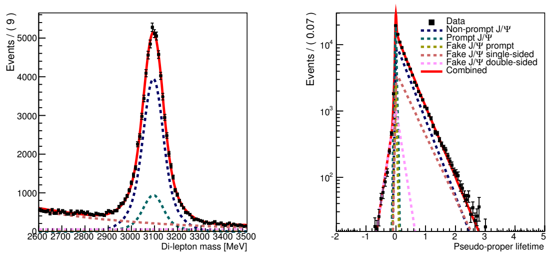

(e) $25<p_T^{\mu\mu\mu}<40$ GeV

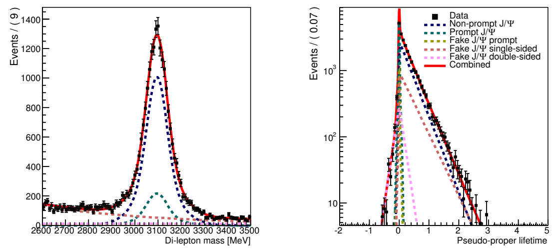

(f) $40<p_T^{\mu\mu\mu}<60$ GeV

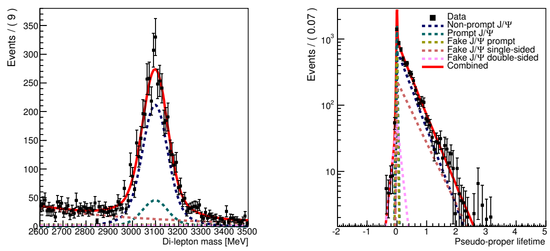

(g) $60<p_T^{\mu\mu\mu}<150$ GeV

Figure A.7.: 2D J/ψ fit results for $p_T^{\mu\mu\mu}$ obsevable.

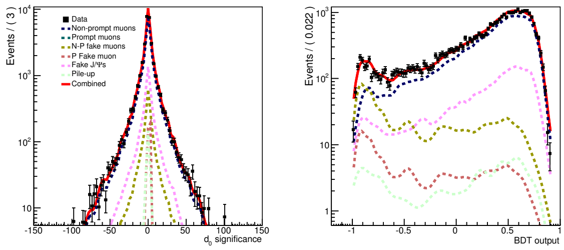

(a) $0<p_T^{\mu\mu\mu}<10$ GeV

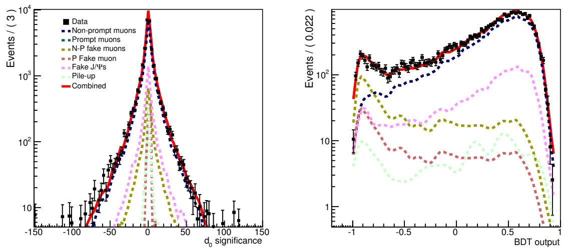

(b) $10<p_T^{\mu\mu\mu}<15$ GeV

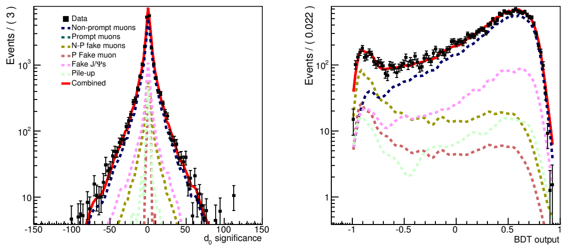

(c) $15<p_T^{\mu\mu\mu}<20$ GeV

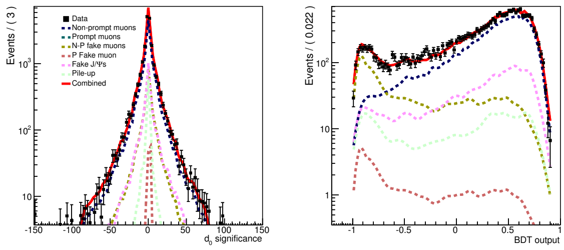

(d) $20<p_T^{\mu\mu\mu}<25$ GeV

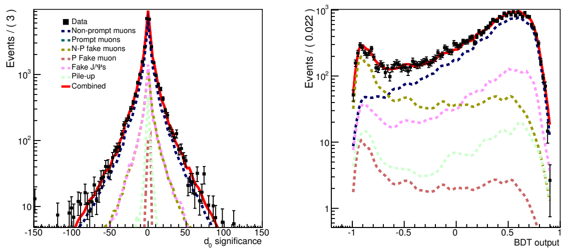

(e) $25<p_T^{\mu\mu\mu}<40$ GeV

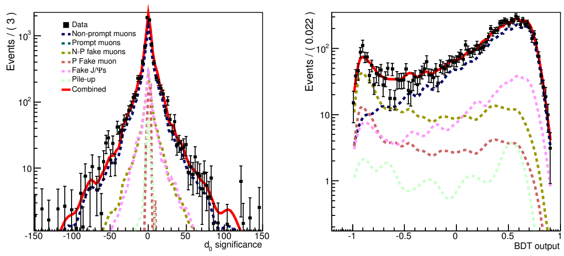

(f) $40<p_T^{\mu\mu\mu}<60$ GeV

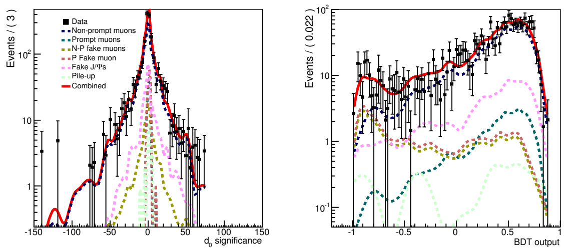

(g) $60<p_T^{\mu\mu\mu}<150$ GeV

Figure A.8.: 2D 3^{rd} muon fit results for $p_T^{\mu\mu\mu}$ observable.

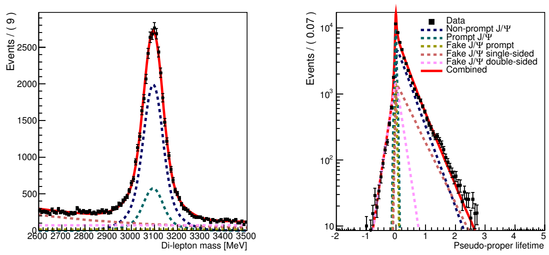

(a) $3 < M^{\mu\mu\mu} < 8$ GeV

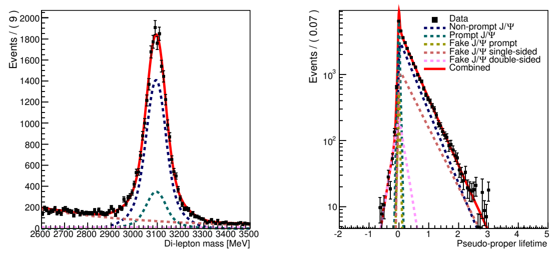

(b) $8 < M^{\mu\mu\mu} < 15$ GeV

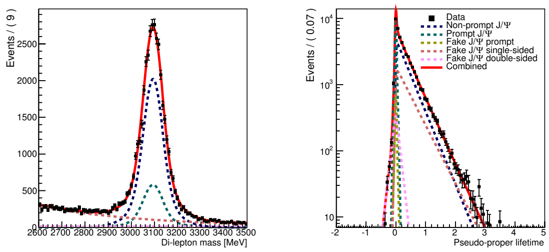

(c) $15 < M^{\mu\mu\mu} < 22$ GeV

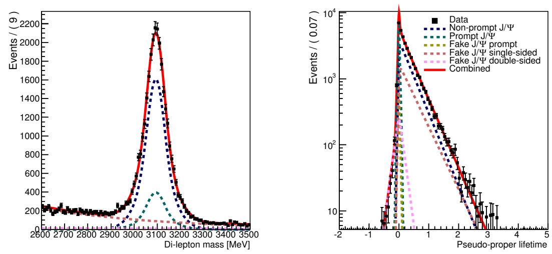

(d) $22 < M^{\mu\mu\mu} < 25$ GeV

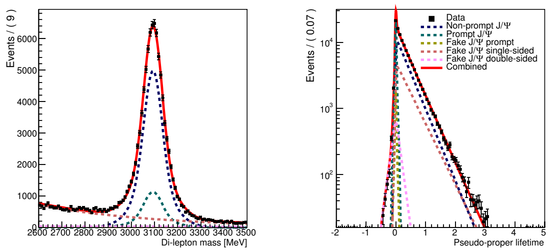

(e) $25 < M^{\mu\mu\mu} < 35$ GeV

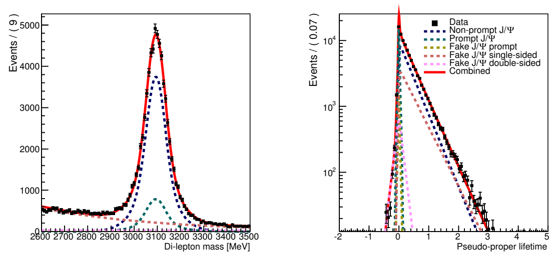

(f) $35 < M^{\mu\mu\mu} < 50$ GeV

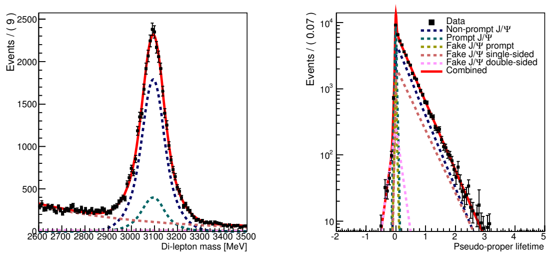

(g) $50 < M^{\mu\mu\mu} < 75$ GeV

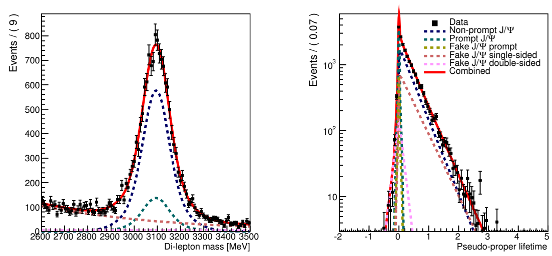

(h) $75 < M^{\mu\mu\mu} < 200$ GeV

Figure A.9.: 2D J/ψ fit results for $M^{\mu\mu\mu}$ observable.

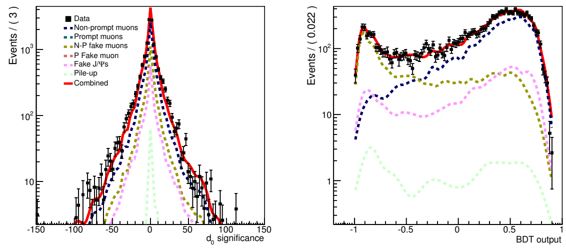

(a) $3<M^{\mu\mu\mu}<8$ GeV

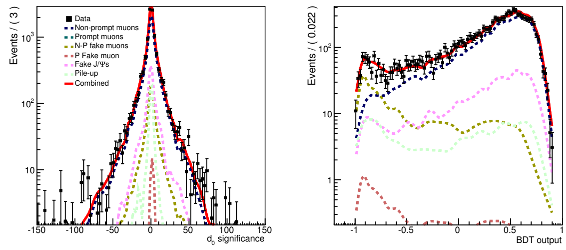

(b) $8<M^{\mu\mu\mu}<15$ GeV

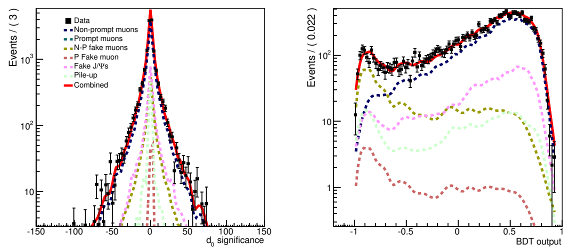

(c) $15<M^{\mu\mu\mu}<22$ GeV

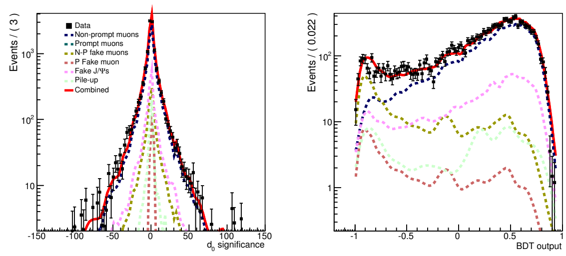

(d) $22<M^{\mu\mu\mu}<25$ GeV

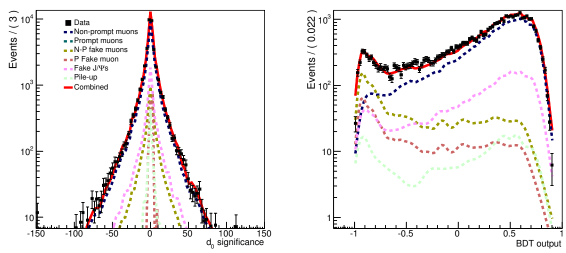

(e) $25<M^{\mu\mu\mu}<35$ GeV

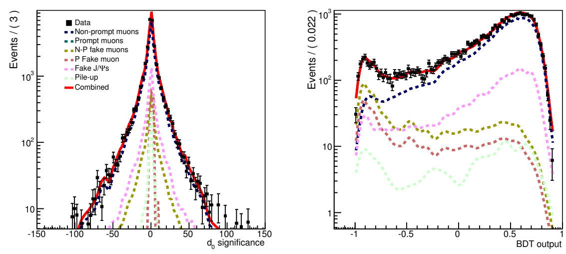

(f) $35<M^{\mu\mu\mu}<50$ GeV

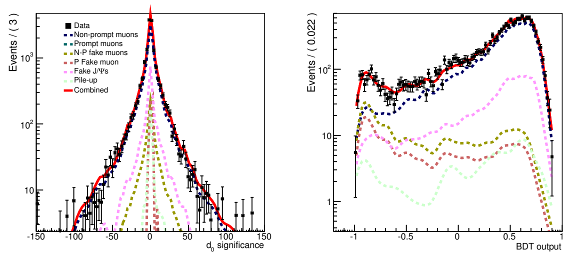

(g) $50<M^{\mu\mu\mu}<75$ GeV

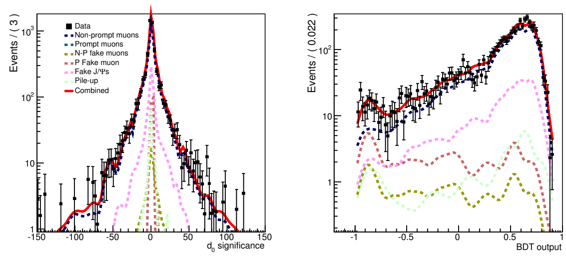

(h) $75<M^{\mu\mu\mu}<200$ GeV

Figure A.10.: 2D 3^{rd} muon fit results for $M^{\mu\mu\mu}$ obsevable.

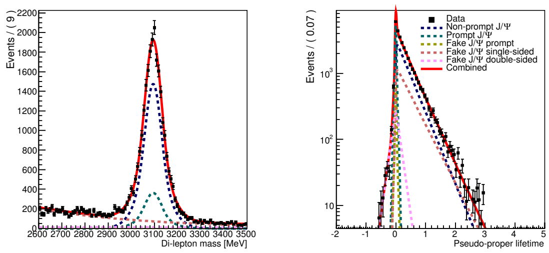

(a) $0<y_{boost}<0.1$

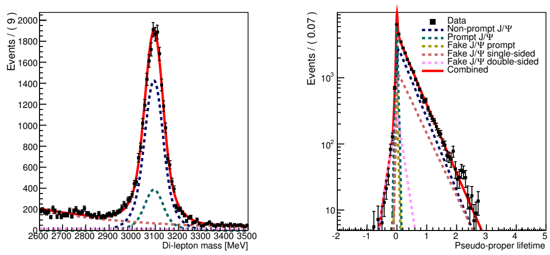

(b) $0.1<y_{boost}<0.22$

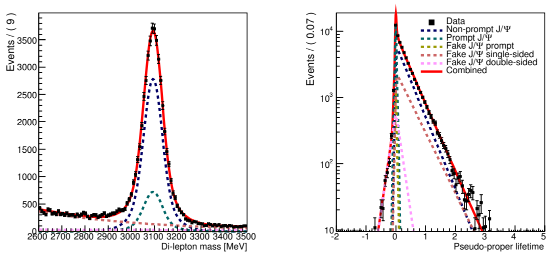

(c) $0.2<y_{boost}<0.4$

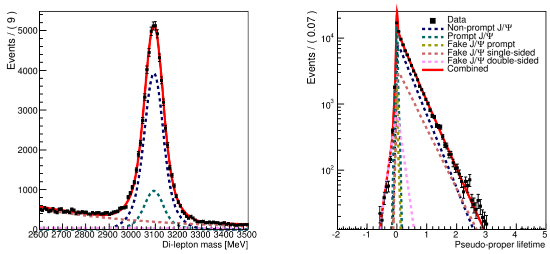

(d) $0.4<y_{boost}<0.7$

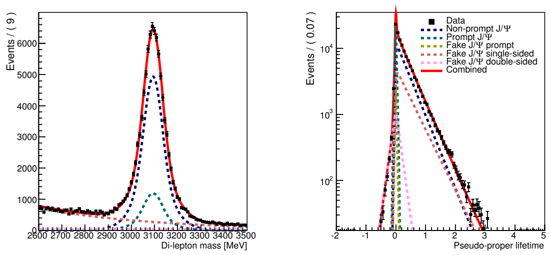

(e) $0.7<y_{boost}<1.2$

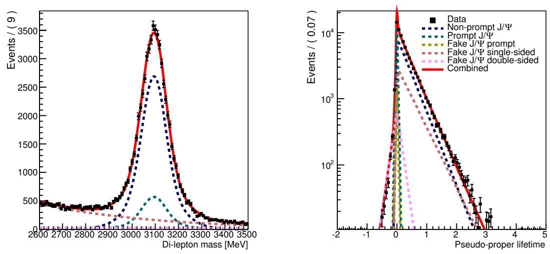

(f) $1.2<y_{boost}<1.7$

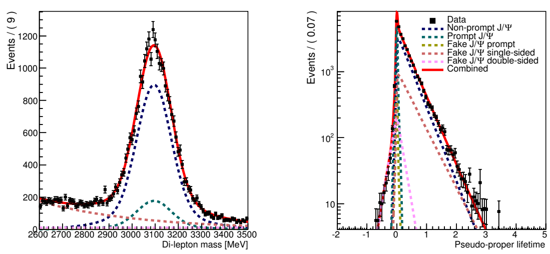

(g) $1.7<y_{boost}<2.5$

Figure A.11.: 2D J/ψ fit results for y_{boost} observable.

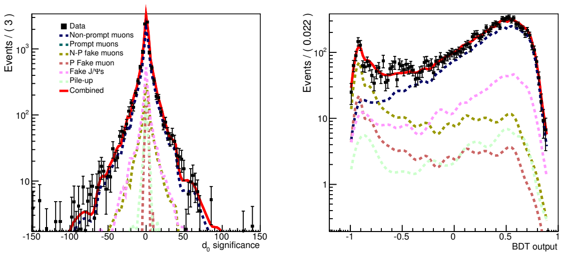

(a) $0{<}y_{boost}{<}0.1$

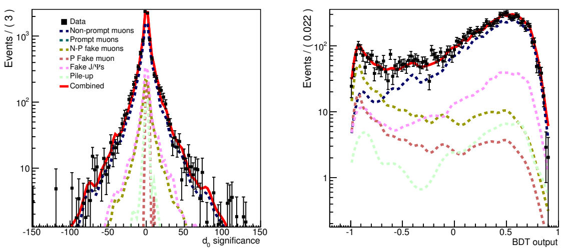

(b) $0.1{<}y_{boost}{<}0.22$

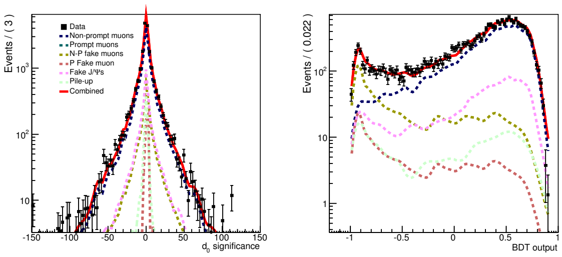

(c) $0.2{<}y_{boost}{<}0.4$

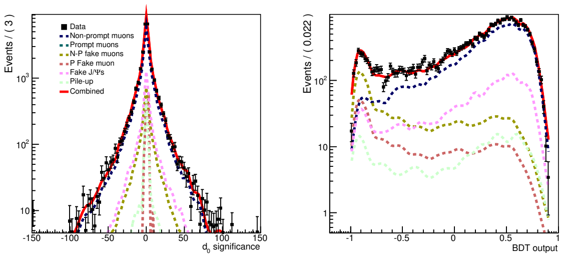

(d) $0.4{<}y_{boost}{<}0.7$

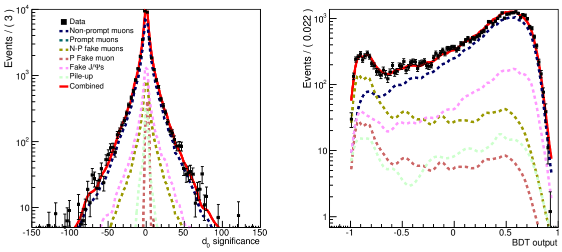

(e) $0.7{<}y_{boost}{<}1.2$

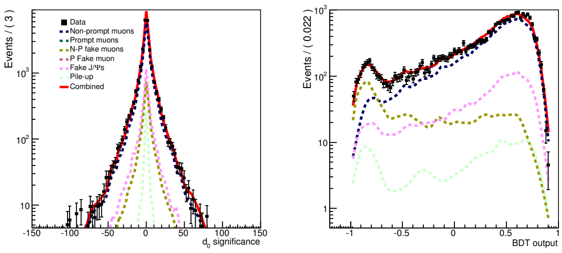

(f) $1.2{<}y_{boost}{<}1.7$

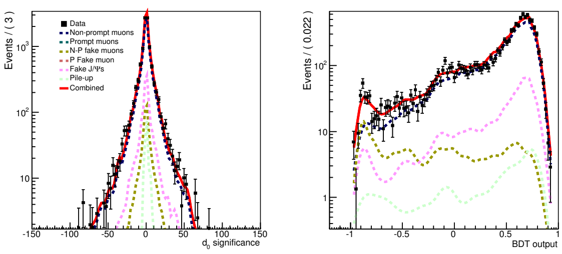

(g) $1.7{<}y_{boost}{<}2.5$

Figure A.12.: 2D 3^{rd} muon fit results for y_{boost} obsevable.

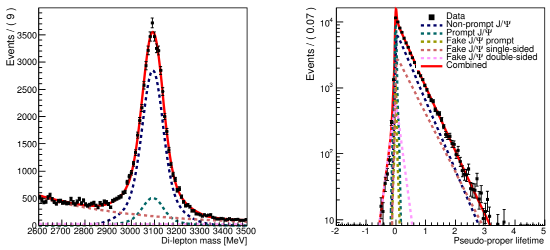

(a) $0 < \frac{p_T}{m} < 0.25$

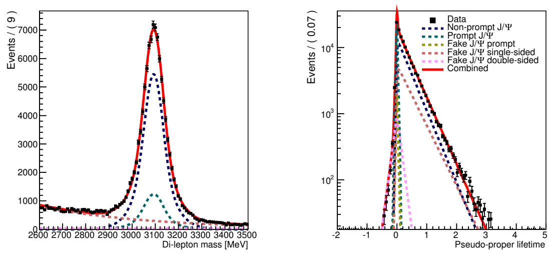

(b) $0.25 < \frac{p_T}{m} < 0.5$

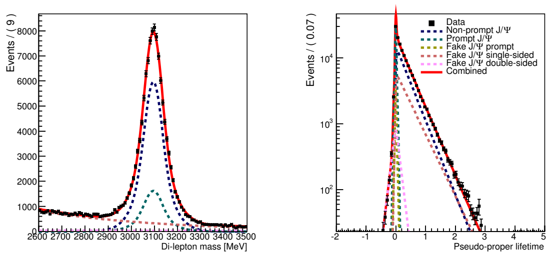

(c) $0.5 < \frac{p_T}{m} < 1.5$

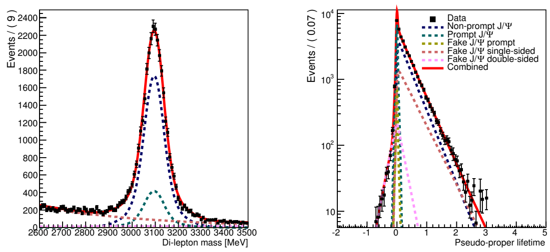

(d) $1.5 < \frac{p_T}{m} < 3.5$

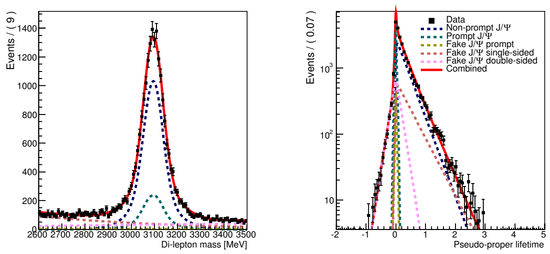

(e) $3.5 < \frac{p_T}{m} < 5.5$

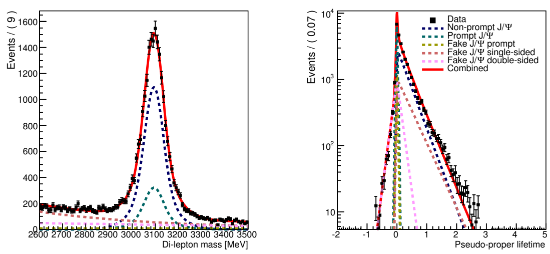

(f) $5.5 < \frac{p_T}{m} < 30.5$

Figure A.13.: 2D J/ψ fit results for $\frac{p_T}{m}$ obsevable.

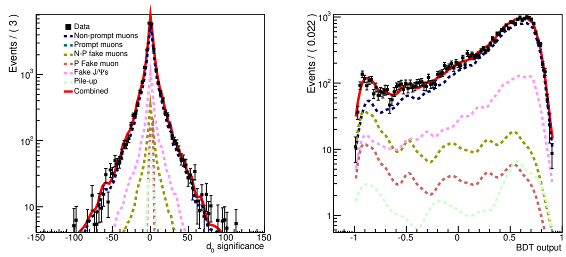

(a) $0<\frac{p_T}{m}<0.25$

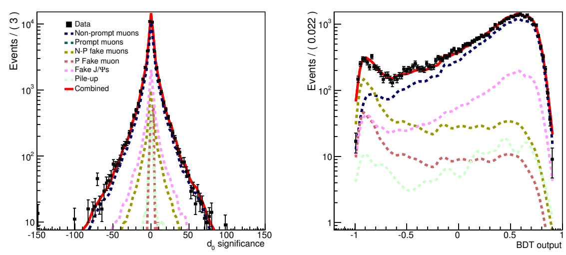

(b) $0.25<\frac{p_T}{m}<0.5$

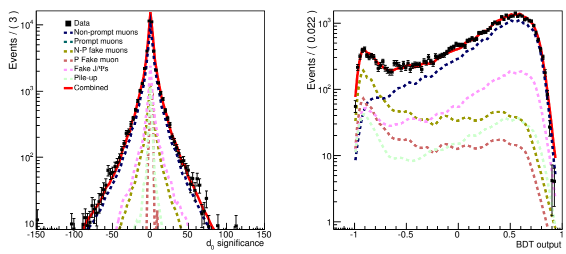

(c) $0.5<\frac{p_T}{m}<1.5$

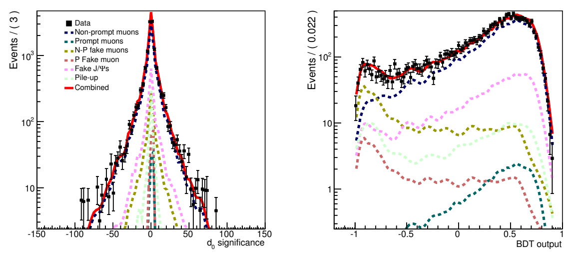

(d) $1.5<\frac{p_T}{m}<3.5$

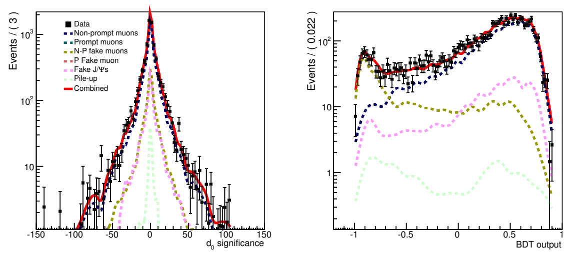

(e) $3.5<\frac{p_T}{m}<5.5$

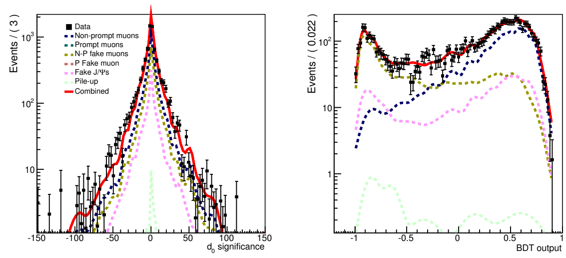

(f) $5.5<\frac{p_T}{m}<30.5$

Figure A.14.: 2D 3^{rd} muon fit results for $\frac{p_T}{m}$ obsevable.

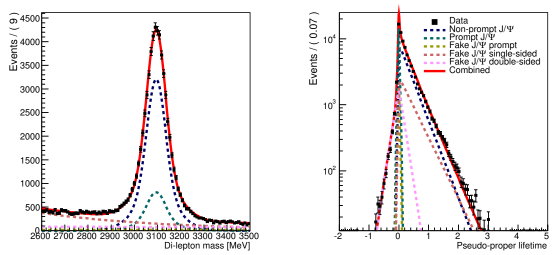

(a) $0<\frac{m}{p_T}<0.5$

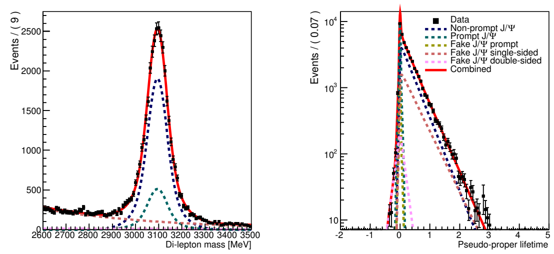

(b) $0.5<\frac{m}{p_T}<1.0$

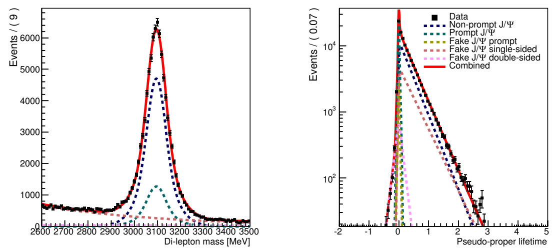

(c) $1.0<\frac{m}{p_T}<2.0$

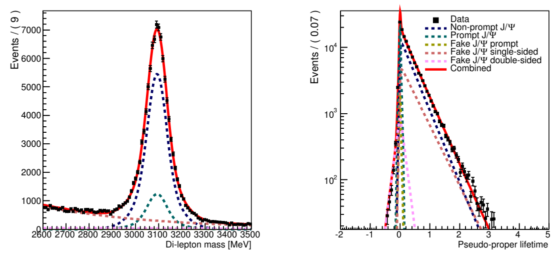

(d) $2.0<\frac{m}{p_T}<4.0$

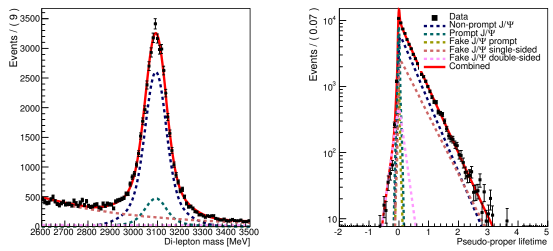

(e) $4.0<\frac{m}{p_T}<15.0$

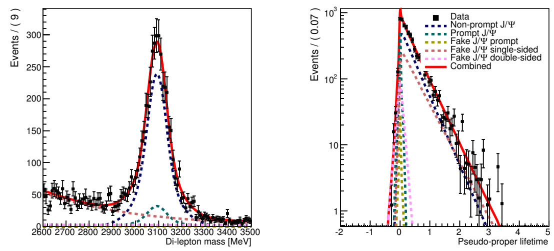

(f) $15.0<\frac{m}{p_T}<150.0$

Figure A.15.: 2D J/ψ fit results for $\frac{m}{p_T}$ obsevable.

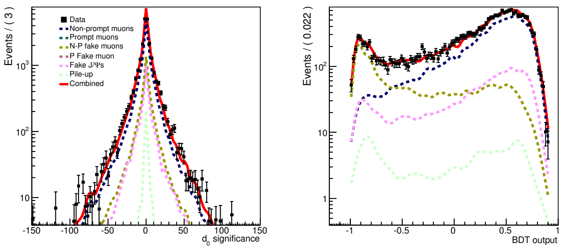

(a) $0<\frac{m}{p_T}<0.5$

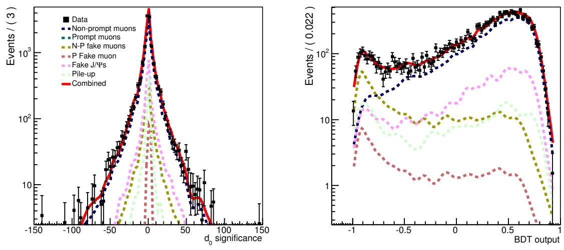

(b) $0.5<\frac{m}{p_T}<1.0$

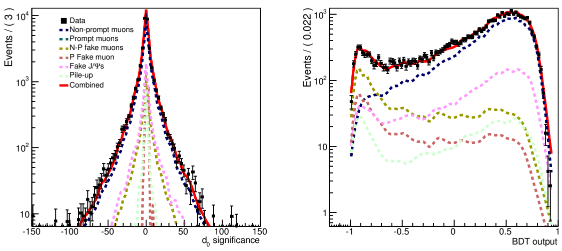

(c) $1.0<\frac{m}{p_T}<2.0$

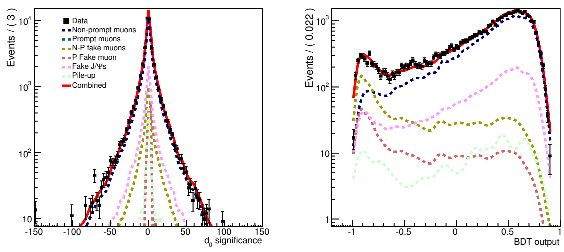

(d) $2.0<\frac{m}{p_T}<4.0$

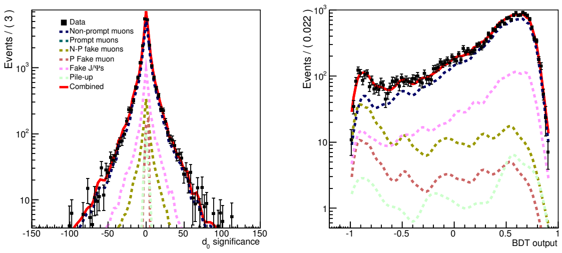

(e) $4.0<\frac{m}{p_T}<15.0$

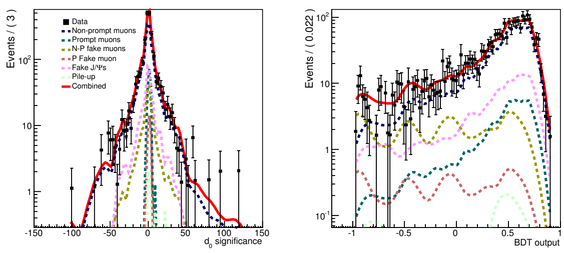

(f) $15.0<\frac{m}{p_T}<150.0$

Figure A.16.: 2D 3^{rd} muon fit results for $\frac{m}{p_T}$ obsevable.

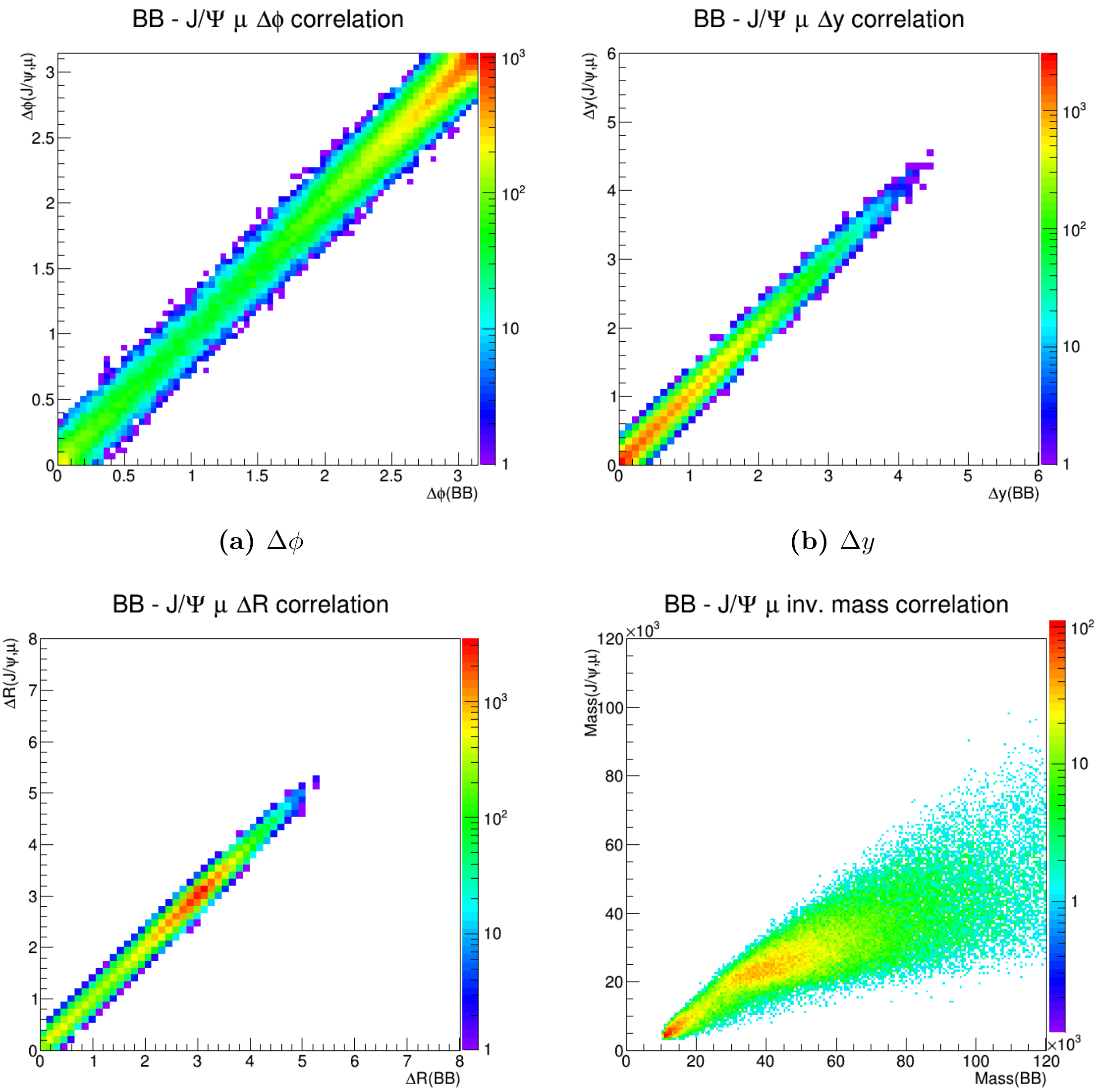

(a) $\Delta\phi$

(b) Δy

(c) ΔR

(d) invariant mass

Figure A.17.: The PTFs for $\Delta\phi$ (a), ΔR (c), Δy (b) between the J/ψ and $3^{rd}\mu$ and the invariant mass of the J/ψ and $3^{rd}\mu$ system (f).

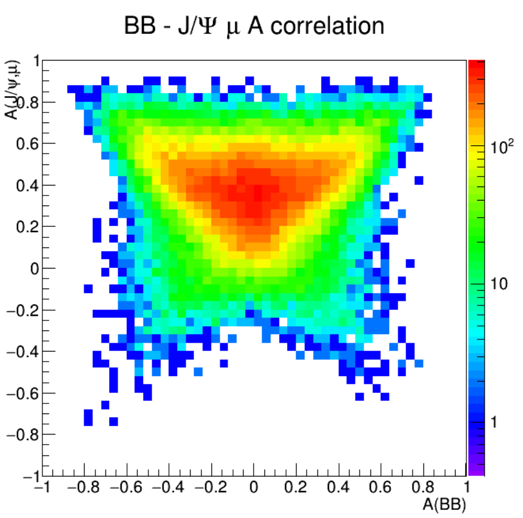

(a) p_T asymmetry

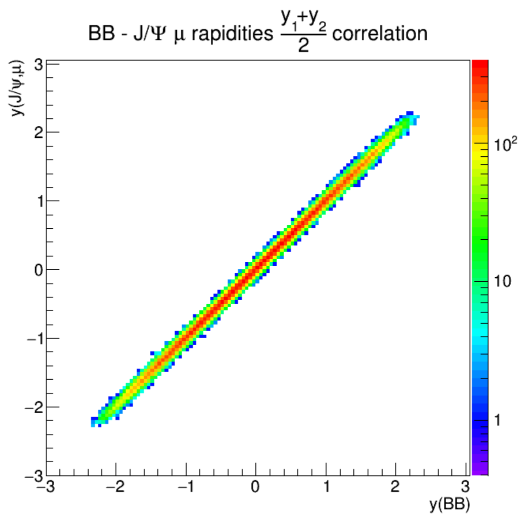

(b) Rapidities

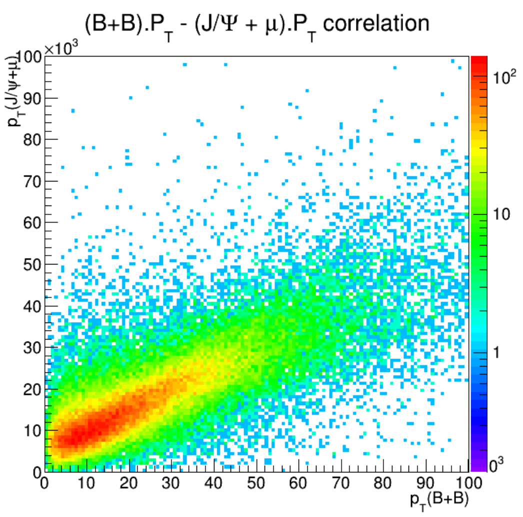

(c) p_T

Figure A.18.: The PTFs of p_T asymmetry between the J/ψ and $3^{rd}\mu$ and original $B\bar{B}$ (a), rapidity (b) and p_T (c) of the J/ψ and $3^{rd}\mu$ system.

Bibliography

[1] The ATLAS Collaboration. Summary of several Standard Model total production cross section measurements. https://atlas.web.cern.ch/Atlas/GROUPS/PHYSICS/CombinedSummaryPlots/SM/index.html#ATLAS_a_SMSummary_TotalXsect, 2015.

[2] H. Fritzsch, Murray Gell-Mann, and H. Leutwyler. Advantages of the Color Octet Gluon Picture. *Phys. Lett.*, B47:365–368, 1973.

[3] C. N. Yang and R. L. Mills. Conservation of isotopic spin and isotopic gauge invariance. *Phys. Rev.*, 96:191–195, Oct 1954.

[4] D. J. Gross and F. Wilczek. Ultraviolet Behavior of Non-Abelian Gauge Theories. *Physical Review Letters*, 30:1343–1346, June 1973.

[5] Frank Wilczek. Asymptotic Freedom. Technical Report hep-th/9609099. IASSNS-HEP-96-92, Princeton Univ. Inst. Adv. Stud., Princeton, NJ, Sep 1996.

[6] K.A. Olive et al. Review of Particle Physics. *Chin.Phys.*, C38:090001, 2014.

[7] S.W. Herb, D.C. Hom, L.M. Lederman, J.C. Sens, H.D. Snyder, et al. Observation of a Dimuon Resonance at 9.5-GeV in 400-GeV Proton-Nucleus Collisions. *Phys.Rev.Lett.*, 39:252–255, 1977.

[8] M. Artuso, D.M. Asner, P. Ball, E. Baracchini, G. Bell, et al. B, D and K decays. *Eur.Phys.J.*, C57:309–492, 2008.

[9] F. del Aguila, J.A. Aguilar-Saavedra, B.C. Allanach, Johan Alwall, Yu. Andreev, et al. Collider aspects of flavour physics at high Q. *Eur.Phys.J.*, C57:183–308, 2008.

[10] John C. Collins, Davison E. Soper, and George F. Sterman. Factorization of Hard Processes in QCD. *Adv.Ser.Direct.High Energy Phys.*, 5:1–91, 1988.

[11] John M. Campbell, J.W. Huston, and W.J. Stirling. Hard Interactions of Quarks

and Gluons: A Primer for LHC Physics. *Rept.Prog.Phys.*, 70:89, 2007.

[12] R.P. Feynman. The behavior of hadron collisions at extreme energies. *Conf.Proc.*, C690905:237–258, 1969.

[13] P. Nason, G. Ridolfi, O. Schneider, G.F. Tartarelli, P. Vikas, et al. Bottom production. 1999.

[14] Michelangelo L. Mangano, Paolo Nason, and Giovanni Ridolfi. Heavy quark correlations in hadron collisions at next-to-leading order. *Nucl.Phys.*, B373:295–345, 1992.

[15] S.P. Baranov and M. Smizanska. Measuring b-b correlations in ATLAS, 2000.

[16] S. Robins. Measuring b-b correlations in ATLAS. 2000.

[17] Georges Aad et al. Observation of a new χ_b state in radiative transitions to $\Upsilon(1S)$ and $\Upsilon(2S)$ at ATLAS. *Phys.Rev.Lett.*, 108:152001, 2012.

[18] S. L. Glashow, J. Iliopoulos, and L. Maiani. Weak interactions with lepton-hadron symmetry. *Phys. Rev. D*, 2:1285–1292, Oct 1970.

[19] J.E. Augustin et al. Discovery of a Narrow Resonance in e+ e- Annihilation. *Phys.Rev.Lett.*, 33:1406–1408, 1974.

[20] J.J. Aubert et al. Experimental Observation of a Heavy Particle J. *Phys.Rev.Lett.*, 33:1404–1406, 1974.

[21] N. Brambilla, S. Eidelman, B.K. Heltsley, R. Vogt, G.T. Bodwin, et al. Heavy quarkonium: progress, puzzles, and opportunities. *Eur.Phys.J.*, C71:1534, 2011.

[22] Gerhard A. Schuler. Quarkonium production and decays. *Phys.Rept.*, 1994.

[23] B. Abbott et al. Small angle J/ψ production in $p\bar{p}$ collisions at $\sqrt{s} = 1.8$ TeV. *Phys.Rev.Lett.*, 82:35–40, 1999.

[24] The ATLAS collaboration. Measurement of the differential cross-sections of inclusive, prompt and non-prompt J/ψ production in proton-proton collisions at $\sqrt{s} = 7$ TeV. *Nucl.Phys.*, B850:387–444, 2011.

[25] UA1 collaboration. Measurement of $b\bar{b}$ correlations at the cern$p\bar{p}$ collider. *Zeitschrift für Physik C Particles and Fields*, 61(1):41–52, 1994.

[26] D. Acosta et al. Measurements of $b\bar{b}$ azimuthal production correlations in $p\bar{p}$ collisions

at $\sqrt{s} = 1.8$ TeV. *Phys.Rev.*, D71:092001, 2005.

[27] B. Abbott et al. The $b\bar{b}$ production cross section and angular correlations in $p\bar{p}$ collisions at $\sqrt{s} = 1.8$ TeV. *Phys.Lett.*, B487:264–272, 2000.

[28] B et al. Abbott. The $b\bar{b}$ Production Cross Section and Angular Correlations in $p\overline{p}$ Collisions at $\sqrt{s} = 1.8$ TeV. *Phys. Lett. B*, 487(hep-ex/9905024. FERMILAB-PUB-99-144-E):264–272. 7 p, May 1999.

[29] CDF Collaboration. Measurements of bottom-antibottom azimuthal production correlations in proton-antiproton collisions at $\sqrt{s} = 1.8$ tev. *Phys. Rev. D*, 71:092001, May 2005.

[30] Leonardo Sala. Measurements on B-hadron angular correlations at 7-TeV with the CMS experiment. *AIP Conf.Proc.*, 1441:675–677, 2012.

[31] Vardan Khachatryan et al. Measurement of $B\bar{B}$ Angular Correlations based on Secondary Vertex Reconstruction at $\sqrt{s} = 7$ TeV. *JHEP*, 1103:136, 2011.

[32] Andy Buckley, Jonathan Butterworth, Stefan Gieseke, David Grellscheid, Stefan Hoche, et al. General-purpose event generators for LHC physics. *Phys.Rept.*, 504:145–233, 2011.

[33] Peter Z. Skands. QCD for Collider Physics. 2011.

[34] C. Ay, A. Buckley, J. Butterworth, J. Ferland, I. Hinchliffe, et al. Monte Carlo generators in ATLAS software. *J.Phys.Conf.Ser.*, 219:032001, 2010.

[35] T. Sjostrand and Peter Z. Skands. Transverse-momentum-ordered showers and interleaved multiple interactions. *Eur.Phys.J.*, C39:129–154, 2005.

[36] Torbjorn Sjostrand, Stephen Mrenna, and Peter Z. Skands. PYTHIA 6.4 Physics and Manual. *JHEP*, 0605:026, 2006.

[37] Torbjörn Sjöstrand, Stefan Ask, Jesper R. Christiansen, Richard Corke, Nishita Desai, et al. An Introduction to PYTHIA 8.2. 2014.

[38] T. Sjostrand. PYTHIA 5.7 and JETSET 7.4 physics and manual. 1994.

[39] Judith M. Katzy. QCD Monte-Carlo model tunes for the LHC. *Prog.Part.Nucl.Phys.*, 73:141–187, 2013.

[40] Tomas Kasemets. Inclusion of Parton Distribution Functions in PYTHIA8. 2010.

[41] Georges Aad et al. Summary of ATLAS Pythia 8 tunes. 2012.

[42] Hung-Liang Lai, Joey Huston, Stephen Mrenna, Pavel Nadolsky, Daniel Stump, Wu-Ki Tung, and C. P. Yuan. Parton Distributions for Event Generators. *JHEP*, 04:035, 2010.

[43] Bo Andersson, G. Gustafson, G. Ingelman, and T. Sjostrand. Parton Fragmentation and String Dynamics. *Phys.Rept.*, 97:31–145, 1983.

[44] Taichi Kawanai and Shoichi Sasaki. Interquark potential with finite quark mass from lattice qcd. *Phys. Rev. Lett.*, 107:091601, Aug 2011.

[45] Ralph Assmann, Mike Lamont, and Steve Myers. A brief history of the {LEP} collider. *Nuclear Physics B - Proceedings Supplements*, 109(2–3):17 – 31, 2002. Proceedings of the 7th Topical Seminar.

[46] Mike Lamont. Status of the lhc. *Journal of Physics: Conference Series*, 455(1):012001, 2013.

[47] CERN. ATLAS: Letter of intent for a general purpose p p experiment at the large hadron collider at CERN. 1992.

[48] Georges Aad et al. Measurement of the Higgs boson mass from the $H \to \gamma\gamma$ and $H \to ZZ^* \to 4\ell$ channels with the ATLAS detector using 25 fb^{-1} of pp collision data. *Phys.Rev.*, D90(5):052004, 2014.

[49] Georges Aad et al. Measurement of Higgs boson production in the diphoton decay channel in pp collisions at center-of-mass energies of 7 and 8 TeV with the ATLAS detector. *Phys.Rev.*, D90(11):112015, 2014.

[50] ATLAS Collaboration. Expected Performance of the ATLAS Experiment - Detector, Trigger and Physics. 2009.

[51] G. Aad et al. The ATLAS Experiment at the CERN Large Hadron Collider. *JINST*, 3:S08003, 2008.

[52] G. Aad, M. Ackers, F.A. Alberti, M. Aleppo, G. Alimonti, et al. ATLAS pixel detector electronics and sensors. *JINST*, 3:P07007, 2008.

[53] M Capeans, G Darbo, K Einsweiller, M Elsing, T Flick, M Garcia-Sciveres, C Gemme, H Pernegger, O Rohne, and R Vuillermet. ATLAS Insertable B-Layer Technical Design Report. Technical Report CERN-LHCC-2010-013. ATLAS-TDR-19, CERN,

Geneva, Sep 2010.

[54] H. Oide. The Pixel Detector of the ATLAS experiment for Run 2 of the Large Hadron Collider. *JINST*, 9(12):C12034, 2014.

[55] Georges Aad et al. ATLAS muon spectrometer: Technical design report. 1997.

[56] The ATLAS collaboration. Performance of the ATLAS muon trigger in pp collisions at $\sqrt{s} = 8$ TeV. 2014.

[57] R (SLAC) Bartoldus, C (Marseille CPPM) Bee, D (CERN) Francis, N (RAL) Gee, S (London RHBNC) George, R (Michigan SU) Hauser, R (RAL) Middleton, T (CERN) Pauly, O (KEK) Sasaki, D (Oregon) Strom, R (Roma I) Vari, and S (Roma I) Veneziano. Technical Design Report for the Phase-I Upgrade of the ATLAS TDAQ System. Technical Report CERN-LHCC-2013-018. ATLAS-TDR-023, CERN, Geneva, Sep 2013. Final version presented to December 2013 LHCC.

[58] Peter Jenni, Marzio Nessi, Markus Nordberg, and Kenway Smith. *ATLAS high-level trigger, data-acquisition and controls: Technical Design Report*. Technical Design Report ATLAS. CERN, Geneva, 2003.

[59] Georges Aad et al. Event Filter stream recording rates per month. https://twiki.cern.ch/twiki/bin/view/AtlasPublic/TriggerOperationPublicResults, 2015.

[60] ATLAS first level trigger: Technical design report. 1998.

[61] Georges Aad et al. Performance of the ATLAS Trigger System in 2010. *Eur.Phys.J.*, C72:1849, 2012.

[62] P Bernat. Architecture and Performance of the Inner Detector Trigger of the ATLAS detector. Technical Report ATL-DAQ-PROC-2012-032, CERN, Geneva, Jun 2012.

[63] Andrea Ventura. The muon high level trigger of the ATLAS experiment. *J.Phys.Conf.Ser.*, 219:032025, 2010.

[64] Georges Aad et al. Di-muon invariant mass for B physics triggers in 2011 data . https://twiki.cern.ch/twiki/bin/view/AtlasPublic/BPhysicsTriggerPublicResults, 2012.

[65] G. Barrand, I. Belyaev, P. Binko, M. Cattaneo, R. Chytracek, et al. GAUDI - A software architecture and framework for building HEP data processing applications.

Comput.Phys.Commun., 140:45–55, 2001.

[66] Eric Christian Lançon. Preparing ATLAS Distributed Computing for LHC Run 2. *PoS*, ISGC2014:045, 2014.

[67] GA Stewart, J. Boyd, JF da Costa, J. Tuggle, and G. Unal. Prompt data reconstruction at the ATLAS experiment. 2012.

[68] P.J. Laycock, N. Ozturk, Matthew Beckingham, R. Henderson, and Lei Zhou. Derived Physics Data Production in ATLAS: Experience with Run 1 and Looking Ahead. *J.Phys.Conf.Ser.*, 513:032052, 2014.

[69] Grigory Rybkin. ATLAS software configuration and build tool optimisation. *J.Phys.Conf.Ser.*, 513:052031, 2014.

[70] R. Brun, F. Rademakers, and S. Panacek. ROOT, an object oriented data analysis framework. *Conf.Proc.*, C000917:11–42, 2000.

[71] John Apostolakis and Dennis H. Wright. An overview of the GEANT4 toolkit. *AIP Conf.Proc.*, 896:1–10, 2007.

[72] P.J. Clark. The ATLAS detector simulation. *Nucl.Phys.Proc.Suppl.*, 215:85–88, 2011.

[73] F. Akesson, M.J. Costa, D. Dobos, M. Elsing, S. Fleischmann, et al. ATLAS Inner Detector Event Data Model. 2007.

[74] T Cornelissen, M Elsing, S Fleischmann, W Liebig, E Moyse, and A Salzburger. Concepts, Design and Implementation of the ATLAS New Tracking (NEWT). Technical Report ATL-SOFT-PUB-2007-007. ATL-COM-SOFT-2007-002, CERN, Geneva, Mar 2007.

[75] Georges Aad et al. Measurement of the muon reconstruction performance of the ATLAS detector using 2011 and 2012 LHC proton-proton collision data. *Eur.Phys.J.*, C74(11):3130, 2014.

[76] R. Nicolaidou, L. Chevalier, S. Hassani, J.F. Laporte, E. Le Menedeu, et al. Muon identification procedure for the ATLAS detector at the LHC using Muonboy reconstruction package and tests of its performance using cosmic rays and single beam data. *J.Phys.Conf.Ser.*, 219:032052, 2010.

[77] S. Armstrong, K.A. Assamagan, J.T.M. Baines, C.P. Bee, M. Bellomo, et al. Imple-

mentation and performance of the third level muon trigger of the ATLAS experiment at LHC. *IEEE Trans.Nucl.Sci.*, 53:500–505, 2006.

[78] E Moyse, A Nisati, A Oh, and D Quarrie. REPORT OF THE MUON RECONSTRUCTION SELECTION PANEL. Technical Report ATL-COM-MUON-2011-040, CERN, Geneva, Dec 2011.

[79] Christos Anastopoulos et al. Physics analysis tools for beauty physics in ATLAS. *J.Phys.Conf.Ser.*, 119:032003, 2008.

[80] Gavin Grant Hesketh, Michal Marcisovsky, Joshua Angus Mcfayden, Stephen Jiggins, and Peter Davison. Measurement of $BB \to J/\psi + \mu$ production at 8 TeV. Technical Report ATL-COM-PHYS-2015-488, CERN, Geneva, Jun 2015.

[81] S.D. Drell and Tung-Mow Yan. Massive Lepton Pair Production in Hadron-Hadron Collisions at High-Energies. *Phys.Rev.Lett.*, 25:316–320, 1970.

[82] Jan Therhaag. TMVA: Toolkit for multivariate data analysis. *AIP Conf.Proc.*, 1504:1013–1016, 2009.

[83] Georges Aad et al. Luminosity Determination in *pp* Collisions at $\sqrt{s} = 7$ TeV Using the ATLAS Detector at the LHC. *Eur.Phys.J.*, C71:1630, 2011.

[84] Kyle Cranmer. Kernel estimation in high-energy physics. *Comput. Phys. Commun.*, 136:198–207, 2001.

[85] M. Smizanska. PythiaB interface to Pythia6 dedicated to simulation of beauty events. 2003. Accessed: 2015-02-15.

[86] ATLAS Collaboration. The simulation principle and performance of the ATLAS fast calorimeter simulation FastCaloSim. 2010.

[87] Richard Corke and Torbjorn Sjostrand. Multiparton Interactions with an x-dependent Proton Size. *JHEP*, 1105:009, 2011.

[88] Richard Corke and Torbjorn Sjostrand. Interleaved Parton Showers and Tuning Prospects. *JHEP*, 1103:032, 2011.

[89] M. Bahr et al. Herwig++ physics and manual. *Eur. Phys. J.*, C58:639–707, 2008.

[90] Georges Aad et al. Measurement of Upsilon production in 7 TeV pp collision at ATLAS. *Phys. Rev.*, D87(5):052004, 2013.

[91] H Evans, V Kartvelishvili, D Price, and Y Yang. Measurement of Upsilon Production in 7 TeV pp Collisions at ATLAS. Technical Report ATL-COM-PHYS-2012-208, CERN, Geneva, Feb 2012.

[92] G. Aad et al. Measurement of the muon reconstruction performance of the ATLAS detector using 2011 and 2012 LHC proton-proton collision data. *Eur.Phys.J.*, C74, 2014.

[93] J. Gaiser. *Charmonium Spectroscopy From Radiative Decays of the J/ψ and ψ'*. PhD thesis, SLAC, 1982.

[94] The ATLAS Collaboration. Number of interactions per bunch crossing used in mc12 post-data-taking production. https://twiki.cern.ch/twiki/bin/view/AtlasPublic/DataPrepGenPublicResults, 2013.

[95] Kingman Cheung. Bc meson production at the tevatron revisited. *Physics Letters B*, 472(3–4):408 – 411, 2000.

[96] Wouter Verkerke and David P. Kirkby. The RooFit toolkit for data modeling. *eConf*, C0303241:MOLT007, 2003.

[97] Georges Aad et al. Improved luminosity determination in pp collisions at $\sqrt{s} = 7$ TeV using the ATLAS detector at the LHC. *Eur. Phys. J. C*, 73(arXiv:1302.4393. CERN-PH-EP-2013-026):2518. 40 p, Feb 2013. Comments: 26 pages plus author list (39 pages total), 17 figures, 9 tables, submitted to EPJC.

List of Figures

List of Tables

Glossary

BDT boosted decision tree. 65, 66

BSM beyond Standard Model. 4

CEM Color Evaporation Model. 17

COM Color Octet Model. 17

CSM Color Singlet Model. 17

DIF decays in flight. 97

ECR electron cyclotron resonance. 30

FSR final-state radiation. 8, 22

ID inner detector. 13, 164

ISR initial-state radiation. 8, 22

LEIR Low Energy Ion Ring. 30

LHC Large Hadron Collider. 1

LO leading-order. 6

MPI multi-parton interaction. 23

NLO next-to-leading order. 5, 6, 22

NNLO next-to NLO. 6, 22

PDF parton distribution functions. 5

PS parton shower. 22

PS proton synchrotron booster. 29

QCD quantum chromodynamics. 1, 17

QED quantum electrodynamics. 1

RFQ radiofrequency quadrupole. 29

SLHC superluminosity LHC. 29

SM Standard Model. 1, 4